# ADVANCED QUANTUM LIGHT SOURCES FOR QUANTUM NETWORKING

*by*

Christopher Leo Morrison

Submitted for the degree of
Doctor of Philosophy

Institute of Photonics and Quantum Sciences
School of Engineering and Physical Sciences
Heriot-Watt University

October 24, 2022

The copyright in this thesis is owned by the author. Any quotation from the report or use of any of the information contained in it must acknowledge this report as the source of the quotation or information.

# Abstract

All of quantum photonics relies on being able to reliably generate quantum states encoded in a particular degree of freedom of light. A key piece of technology is therefore the photon source.

The choice of which degree of freedom to encode information in is an interesting one, there is no universal best option. The historically common option of polarisation is straightforward to manipulate and detect, but is restricted to a two dimensional Hilbert space. More modern choices such as orbital angular momentum and path encodings have become popular as they are high dimensional and offer greater information capacity per photon. The downside of these options is they are difficult to integrate into existing communication networks.

Time and frequency are in a unique position of being naturally high dimensional and compatible with single-mode fibre which makes them compatible with standard telecommunication equipment. The first half of this thesis is about generating time-frequency encoded quantum states in a scalable, lossless and arguably simpler way than other techniques commonly used to generate time-frequency encoded states. This is done through the process of domain-engineering in parametric downconversion. This thesis will walk through the basics of nonlinear optics and particular three-wave mixing before going on to discuss the principles of domain-engineering and how it can be used to manipulate the time-frequency structure of photon pairs produced in parametric downconversion. The experimental characterisation of a high dimensional frequency-bin entangled source is discussed along with other potential time-frequency states which could be generated using the same domain-engineering techniques.

The second half of the thesis is centred around building a bright and low noise single-photon source at telecommunication wavelengths using a frequency converted quantum dot. The performance of the source before and after conversion is compared with the end result that the frequency conversion process does not significantly alter the single-photon nature of the source. Using the mathematical machinery developed to describe three-wave mixing, we show how the time-frequency properties of quantum dots can be improved using frequency conversion.

With a bright and low noise source realised, a demonstration of quantum key distribution is carried out. The range and key rate of this demonstration compare favourably to to other single-photon sources in the literature. Finally, theoretical predictions of a decoy state quantum key distribution protocol using this source are carried out which extends the range by around 100 km compared to the protocol without decoy states.

# Acknowledgements

The quote "You're the average of the five people spend the most time with," is most often attributed to the motivational speaker Jim Rohn. Whether you believe this statement to be true or not, I have had the privileged of being surrounded by some excellent scientist who have doubled as some excellent friends.

Foremost among these has to be my supervisor Alessandro. Sandro you have been an immeasurably positive force throughout my PhD. I have enjoyed our discussions on everything from the foundations of quantum mechanics to beer ("there are only four ingredients,") and many things in between. I appreciate the freedom you afforded me to pursue whatever ideas I found interesting, which ended up being making weird photons which may or may not be useful for anything. The relaxed and free atmosphere you have cultivated within the group has made for a wonderful atmosphere to carry out research over the last four years. At this point I should also mention the other PI involved in my work, Brian. I have to thank you for tolerating my ignorance regarding the intricacies of quantum dots over countless meetings.

And then there were the lab rats.

To Francesco, I could not have asked for a better friend to spend time in the lab and share a mutual love of all things nonlinear optics. Our conversations have made me a better experimentalist and deepened my understanding of quantum optics. A large portion of this thesis is built on the foundations you laid throughout your thesis which I am extremely thankful for. To Joseph, you have kept me on the straight and narrow with anything and everything quantum information. You were always there to answer questions and fill in the gaps in my own knowledge for which I am grateful. To both of you, without our Friday evening trips to Diggers my PhD would have been much less entertaining.

I must also thank Zak, without your tireless work on keeping the quantum dot alive while we played around with lasers and waveguides much of this thesis would not have been possible. I also appreciated your relentless swearing at various pieces of equipment in the lab, it was always reassuring and a sign that things were more or less proceeding as expected

To Markus, your attitude really pulled us through the worst times, when we couldn't get the laser working and we were on the 26th realignment of the week, it was made more bearable by your presence. Thank you.

Peter, I have to thank you for your patience in dealing with my questions on the innumerable lines of code you wrote to process the data acquired in the lab. Without your work, this thesis would have taken much longer than it did. To Alex and Mash, you were both always insightful and generous with your time in the lab when I came along looking for tips. To the younger students in the group, Jonathan, Fred and Fabrizio I hope you enjoy your PhD as much as I have enjoyed mine.

I should also thank Nathan, Helen, Patrick and Michael. Thank you guys for giving me some great advice during difficult times and a good firm push when I needed it most!

I must also thank my parents for their love and support throughout my life. Without your hard work I would not have had the opportunities I have received and would not be the person I am today. By extension I must thank my grandparents, without your hard work and dedication my parents would not have had the opportunities they received, particularly in Northern Ireland at a time when such opportunities were hard to come by. Without your tireless effort to provide a better life for your children my life would have been quite different.

To Anna, you have been the most loving and supportive person throughout our time together, more than I deserve. You have celebrated every high point with me and helped me through every low. Without you I surely would not have made it through my undergrad and doctorate. Your patience and selflessness while I have spent years away studying are a testament to your character, I still find it amazing now. I can't wait to spend the rest of our lives together.

# Research Thesis Submission

Please note this form should be bound into the submitted thesis.

| | | | |
|---|---|---|---|
| Name: | **Christopher Morrison** | | |
| School: | **School of Engineering and Physical Sciences** | | |
| Version: *(i.e. First, Resubmission, Final)* | **FINAL** | Degree Sought: | **Doctor of Philosophy** |

## Declaration

In accordance with the appropriate regulations I hereby submit my thesis and I declare that:

1. The thesis embodies the results of my own work and has been composed by myself
2. Where appropriate, I have made acknowledgement of the work of others
3. The thesis is the correct version for submission and is the same version as any electronic versions submitted*.
4. My thesis for the award referred to, deposited in the Heriot-Watt University Library, should be made available for loan or photocopying and be available via the Institutional Repository, subject to such conditions as the Librarian may require
5. I understand that as a student of the University I am required to abide by the Regulations of the University and to conform to its discipline.
6. I confirm that the thesis has been verified against plagiarism via an approved plagiarism detection application e.g. Turnitin.

## ONLY for submissions including published works

Please note you are only required to complete the Inclusion of Published Works Form (page 2) if your thesis contains published works)

7. Where the thesis contains published outputs under Regulation 6 (9.1.2) or Regulation 43 (9) these are accompanied by a critical review which accurately describes my contribution to the research and, for multi-author outputs, a signed declaration indicating the contribution of each author (complete)
8. Inclusion of published outputs under Regulation 6 (9.1.2) or Regulation 43 (9) shall not constitute plagiarism.

* *Please note that it is the responsibility of the candidate to ensure that the correct version of the thesis is submitted.*

| | | | |
|---|---|---|---|
| Signature of Candidate: | Christopher Morrison | Date: | **24/10/2022** |

## Submission

| | |
|---|---|
| Submitted By *(name in capitals)*: | Christopher Morrison |
| Signature of Individual Submitting: | Christopher Morrison |
| Date Submitted: | **24/10/2022** |

## For Completion in the Student Service Centre (SSC)

| | | | | | | | | | | |
|---|---|---|---|---|---|---|---|---|---|---|
| Limited Access | Requested | Yes | | No | | Approved | Yes | | No | |
| *E-thesis Submitted* (***mandatory for final theses***) | | | | | | | | | | |
| Received in the SSC by *(name in capitals)*: | | | | | | Date: | | | | |

HERIOT
WATT
UNIVERSITY

# Inclusion of Published Works

Please note you are only required to complete the Inclusion of Published Works Form if your thesis contains published works under Regulation 6 (9.1.2)

---

## Declaration

This thesis contains one or more multi-author published works. In accordance with Regulation 6 (9.1.2) I hereby declare that the contributions of each author to these publications is as follows:

| | |
|---|---|
| Citation details | Christopher L. Morrison, Markus Rambach, Zhe Xian Koong, Francesco Graffitti, Fiona Thorburn, Ajoy K. Kar, Yong Ma, Suk-In Park, Jin Dong Song, Nick G. Stoltz, Dirk Bouwmeester, Alessandro Fedrizzi, and Brian D. Gerardot,<br>“A bright source of telecom single photons based on quantum frequency conversion”,<br>Appl. Phys. Lett. 118, 174003 (2021). |
| Author 1,2,3,4,5 | Constructed the experiment, wrote the manuscript. |
| Author 1,2,3,4 | Acquired and analysed the data. |
| Author 7,8,9,10,11 | Fabricated samples. |
| Author 12,13 | Conceived the experiment, wrote the manuscript. |
| Signature: | Christopher Morrison |
| Date: | **24/10/2022** |

| | |
|---|---|
| Citation details | Christopher L. Morrison, Francesco Graffitti, Peter Barrow, Alexander Pickston, Joseph Ho, and Alessandro Fedrizzi,<br>“Frequency-bin entanglement from domain-engineered down-conversion”,<br>APL Photonics 7, 066102 (2022). |
| Author 1,2,4,5 | Constructed the experiment, wrote the manuscript. |
| Author 1,3,5 | Acquired and analysed the data. |
| Author 6 | Supervised the experiment, wrote the manuscript. |
| Signature: | Christopher Morrison |
| Date: | **24/10/2022** |

# List of publications

## Publications included in this thesis

Christopher L. Morrison, Markus Rambach, Zhe Xian Koong, Francesco Graffitti, Fiona Thorburn, Ajoy K. Kar, Yong Ma, Suk-In Park, Jin Dong Song, Nick G. Stoltz, Dirk Bouwmeester, Alessandro Fedrizzi, and Brian D. Gerardot, *"A bright source of telecom single photons based on quantum frequency conversion"*, Appl. Phys. Lett. 118, 174003 (2021).

Christopher L. Morrison, Francesco Graffitti, Peter Barrow, Alexander Pickston, Joseph Ho, and Alessandro Fedrizzi, *"Frequency-bin entanglement from domain-engineered down-conversion"*, APL Photonics 7, 066102 (2022).

## Other publications

Alexander Pickston, Francesco Graffitti, Peter Barrow, Christopher L. Morrison, Joseph Ho, Agata M. Brańczyk, and Alessandro Fedrizzi, *"Optimised domain-engineered crystals for pure telecom photon sources"*, Opt. Express 29, 6991-7002 (2021).

Joseph Ho, George Moreno, Samuraí Brito, Francesco Graffitti, Christopher L. Morrison, Ranieri Nery, Alexander Pickston, Massimiliano Proietti, Rafael Rabelo, Alessandro Fedrizzi and Rafael Chaves, *"Entanglement-based quantum communication complexity beyond Bell nonlocality"*, npj Quantum Information 8, 13 (2022).

## Conference contributions

Francesco Graffitti, Christopher L. Morrison, Markus Rambach, Zhe Xian Koong, Fiona Thorburn, Yong Ma, Suk-In Park, Jin Dong Song, Ajoy K. Kar, Alessandro Fedrizzi, and Brian D. Gerardot, *"Coherent frequency-conversion of quantum dot photons to the telecommunication C-band for quantum communication applications"*, in Conference on Lasers and Electro-Optics, OSA Technical Digest (Optica Publishing Group, 2021), paper FM3M.3.

Christopher L. Morrison, Francesco Graffitti, Joseph Ho, Peter Barrow, and Alessandro Fedrizzi, *"High dimensional frequency-bin entanglement from domain engineered parametric downconversion"*, in Conference on Lasers and Electro-Optics, OSA Technical Digest (Optica Publishing Group, 2021), paper FM1N.1.

Christopher L. Morrison, Francesco Graffitti, Zhe Xian Koong, Nick G. Stoltz, Dirk Bouwmeester, Alessandro Fedrizzi, Brian D. Gerardot, *"Quantum key distribution with a bright telecom wavelength quantum dot single-photon source"*, Proc. SPIE 11881, Quantum Technology: Driving Commercialisation of an Enabling Science II, 1188103 (6 October 2021)

# Contents

**1 Introduction 1**

**2 Nonlinear Optics 4**

2.1 Nonlinear Polarisation . . . . . . . . . . . . . . . . . . . . . . . . . . 4

2.1.1 Second order nonlinear polarisation . . . . . . . . . . . . . . . . 6

2.2 Quantum treatment of three-wave mixing . . . . . . . . . . . . . . . . . 7

2.2.1 Pump-envelope function . . . . . . . . . . . . . . . . . . . . . . 10

2.2.2 Phasematching function . . . . . . . . . . . . . . . . . . . . . . 11

2.2.3 Joint spectral amplitude . . . . . . . . . . . . . . . . . . . . . . 13

2.3 More on phasematching . . . . . . . . . . . . . . . . . . . . . . . . . . 22

**3 Time-Frequency entangled photon pairs 26**

3.1 Aperiodic poling . . . . . . . . . . . . . . . . . . . . . . . . . . . . . 26

3.2 Design process for aperiodic poled crystals . . . . . . . . . . . . . . . 28

3.3 Time-Frequency encodings . . . . . . . . . . . . . . . . . . . . . . . . 31

3.4 The role of group velocity . . . . . . . . . . . . . . . . . . . . . . . . 35

3.5 Experimental eight-mode frequency-bin entanglement . . . . . . . . . 37

3.5.1 Experimental characterisation . . . . . . . . . . . . . . . . . . . 41

3.5.2 Polarisation frequency-bin hyperentanglement . . . . . . . . . . 52

3.6 A hint towards frequency-bin GHZ states . . . . . . . . . . . . . . . . 55

3.7 Future designs for other time-frequency encodings . . . . . . . . . . . 57

3.7.1 Time-bin crystals . . . . . . . . . . . . . . . . . . . . . . . . . . 58

3.7.2 Hybrid encodings . . . . . . . . . . . . . . . . . . . . . . . . . . 60

**4 Quantum dot frequency conversion** **62**
4.1 Quantum dot . . . . . . . . . . . . . . . . . . . . . . . . . . . . . 63
4.2 Mid-infrared laser . . . . . . . . . . . . . . . . . . . . . . . . . . . 65
  4.2.1 Experimental tips for aligning a cavity . . . . . . . . . . . . . 70
4.3 Lithium niobate waveguide . . . . . . . . . . . . . . . . . . . . . . 71
4.4 Conversion results . . . . . . . . . . . . . . . . . . . . . . . . . . . 73
4.5 From CW to pulsed conversion . . . . . . . . . . . . . . . . . . . . 79
  4.5.1 Density matrix for single photons from a quantum dot . . . . 80
  4.5.2 Frequency jitter . . . . . . . . . . . . . . . . . . . . . . . . . 80
  4.5.3 Emission time jitter . . . . . . . . . . . . . . . . . . . . . . . 82
  4.5.4 Calculating the output state . . . . . . . . . . . . . . . . . . . 83
  4.5.5 Numerical results on pulsed frequency conversion . . . . . . . 84
  4.5.6 Reverse wave frequency conversion . . . . . . . . . . . . . . . 85

**5 Quantum key distribution with a frequency-converted quantum dot** **91**
5.1 Brief overview of the BB84 protocol . . . . . . . . . . . . . . . . . 93
5.2 Key rate for a noisy single-photon source . . . . . . . . . . . . . . . 94
5.3 Experimental Results . . . . . . . . . . . . . . . . . . . . . . . . . . 98
5.4 Finite key rate . . . . . . . . . . . . . . . . . . . . . . . . . . . . . 103
5.5 Extending the range with decoy states . . . . . . . . . . . . . . . . 106

**6 Conclusion** **115**

**A Derivation of PMF for a periodically-poled crystal** **118**

**B Electro-optic modulator characterisation** **120**

# Glossary

**Cr:ZnSe** chromium doped zinc-selenide

**CW** continuous-wave

**DFG** difference-frequency generation

**DoF** degree of freedom

**EOM** electro-optic modulator

**FC** frequency conversion

**FSR** free spectral range

**GHZ** Greenberger-Horne-Zeilinger

**HOMI** Hong-Ou-Mandel interference

**HWP** half-wave plate

**JSA** joint spectral amplitude

**JSI** joint spectral intensity

**JTA** joint temporal amplitude

**KTP** potassium titanyl phosphate

**LN** lithium niobate

**MUB** mutually unbiased bases

**NIR** near-infrared

**OSA** optical spectrum analyser

**PDC** parametric downconversion

**PEF** pump-envelope function

**PMF** phasematching function

**QD** quantum dot

**QKD** quantum key distribution

**QWP** quarter-wave plate

**SFG** sum-frequency generation

**SIC** symmetric informationally complete

**SNR** signal-to-noise ratio

**SVD** singular value decomposition

**TOFS** time-of-flight spectrometer

**WDM** wavelength-division multiplexing

# Chapter 1

# Introduction

In the world of quantum photonics there are roughly three components: sources, circuits and detectors. In the language of quantum information processing this could be rephrased as a way to create, evolve (hopefully in a unitary way) and detect quantum states. The majority of people working in quantum photonics have their work fall into one of these three camps.

This thesis is about sources.

The thesis can be divided roughly down the middle with one half focusing on parametric downconversion (PDC) which has been the workhorse for quantum optics since it was first demonstrated in parametric amplifiers in the 60s [1–3]. As PDC creates pairs of photons, the obvious application of PDC is a source of entanglement for your favourite quantum information protocol. The form of the entanglement comes in many different types, corresponding to the different degrees of freedom a photon may possess. A non-exhaustive list includes: polarisation [4], momentum [5], transverse mode [6], orbital angular momentum [7], central frequency [8], arrival time [9] and the list goes on. The control of photon pairs is so exquisite that entanglement between more than one degree of freedom, so-called hyperentanglement, has been demonstrated in up to three of the possible degrees of freedom listed [10].

My small contribution to the vast body of work on PDC is making photon pairs which share entanglement in time and frequency using atypical poling structures inside the nonlinear crystal. This work leans heavily on the work of Francesco Graffitti [11] who developed a lot of the ideas upon which the experimental work in this thesis is built. The initial application of aperiodic poling was making a completely uncorrelated and separable photon-pair source. The work presented in this thesis came from the opposing point of view, instead of removing the entanglement, it be tailored and produce specific entangled states with the same poling techniques. Hopefully by the end of the thesis I will have convinced the reader of two things. First, one can make some interesting quantum states with aperiodic poling and second, these states might even be useful one day. I am confident I have achieved the former and pessimistic about achieving the latter.

The second half focuses on quantum dot sources, the young(-ish) upstart which has come along to steal the crown of heralded sources as the preferred choice for photonics researchers worldwide. The improvements in quantum dots as single-photon sources has been almost astronomical from the initial observation of non-classical light emission in 2000 [12] towards QDs emitting something close to a single photon around 50% of the time in 2021 [13]. While QDs have have better signal-to-noise scaling than PDC sources they do have their drawbacks. QDs are still effectively probabilistic sources with the collection efficiencies of current devices. There is also the question of scalablility; making two PDC sources with identical properties is relatively straightforward, fabricating multiple QDs to emit identical photons is an extremely difficult task. A third problem is QDs emitting between $700 - 1000$ nm, which I will refer to as near-infrared, have the best quality in terms of efficiency and coherence of the emitted photons. This is not ideal in terms of communication applications, ideally the photons would be around one of the telecommunication bands.

The work in this thesis tries to address the last of these problems. This is done using a bright near-infrared QD source coupled with efficient nonlinear frequency conversion to shift the photon from the near-infrared to 1550 nm. For a while this work constituted the best QD source in the telecommunication C-band before being surpassed by other groups.

Chapter 2 develops the mathematical machinery needed to understand the nonlinear optical processes of parametric downconversion and frequency conversion. It starts from the classical picture of these processes and then develops the quantum mechanical picture introducing concepts such as quasi-phasematching and group-velocity matching. The end goal of this chapter is to describe the joint spectral amplitude, which describes the key features of both parametric downconversion and frequency conversion.

Chapter 3 contains the work on time-frequency entangled photons. This chapter starts with the design process for aperiodically poled nonlinear crystals and the key steps to go from a desired entangled state to the nonlinear crystal design that produces it. The bulk of this chapter is the design and characterisation of an eight-bin frequency entangled state. The chapter concludes with some speculative theory ideas which were developed in the long evenings of lockdown during spring/summer of 2020.

Chapter 4 describes the frequency conversion work towards developing a bright QD source suitable for fibre-optic communications. The experimental components required to realise such a source, the QD, the pump laser to drive the frequency conversion and the nonlinear waveguide are described in turn. The source performance is characterised in terms of count rate, multiphoton suppression and two-photon interference visibility.

Chapter 5 contains the experimental work towards long-range quantum key distribution with the frequency converted QD source. The secure key rate is evaluated theoretically based on the measured source parameters and compared to experimentally measured count rates in an in-lab demonstration of quantum key distribution over 170 km of fibre. A comparison to other single-photon sources in terms of key rate and maximum achievable distance is made which is favourable for our work. The chapter concludes by using recent theoretical results on the decoy-state quantum key distribution scheme for arbitrary photon-number distributions to model how the QD source would perform in a decoy-state protocol which extends the maximum range to 250 km.

# Chapter 2

# Nonlinear Optics

A large portion of this thesis focuses on the interaction of optical modes in a nonlinear medium. This section will give a mathematical description of nonlinear processes in the classical picture and then transition to the quantum view. The machinery developed in this chapter will hopefully build intuition for the specific three-wave mixing interactions behind the experimental work in this thesis.

## 2.1 Nonlinear Polarisation

We consider the case of electric fields propagating in a dielectric medium with frequencies far away from atomic resonances of the medium. We consider the electrons in the medium using a simple Lorentz atomic model (mass and spring model) where the force acting on a given electron is linear. This is a reasonable model as an electron sitting close to the minimum in any potential landscape experiences an approximately quadratic potential. As the electric field oscillates in the material it drives oscillations of bound electrons. One can write the dipole moment per unit volume or polarisation of the material as [14]

$$P = \epsilon_0 \chi^{(1)} E, \tag{2.1}$$

where $P$ is the polarisation of the material, $E$ is the applied electric field, $\chi^{(1)}$ is the linear susceptibility of the material and $\epsilon_0$ is the vacuum permittivity. Typically the electric field is not of sufficient strength to significantly alter the harmonic potential experienced by charges within the medium ($\sim 10^{11}$V/m). This results in linear equations of motion for the charges and therefore a linear response of the material with the applied electric field. With the advent of the laser in 1960 by Maiman [15] a new frontier of physics became experimentally accessible. The electric fields inside a laser beam are strong enough to significantly alter the atomic potential felt by trapped charges and introduce anharmonicities. Due to the anharmonic potential the equations of motion become nonlinear. The response of the material in this nonlinear regime can be accounted for by expanding the polarisation in a Taylor series,

$$\begin{aligned} P &= \epsilon_0 \left( \chi^{(1)} E + \chi^{(2)} EE + \chi^{(3)} EEE + ... \right) \\ &:= P^{(1)} + P^{(2)} + P^{(3)} + .... \end{aligned} \tag{2.2}$$

We define the linear polarisaton as $P^{(1)} = \epsilon_0 \chi^{(1)} E$ and the nonlinear polarisation as the remaining part $P^{\mathrm{NL}} = P - P^{(1)}$. In Eq. (2.2) the vectorial nature of the polaristion has been ignored. Generally the polarisation field generated and electric field which generated it do not need to be aligned in terms of polarisation, in this case the $\chi^{(n)}$ is a $n$-rank tensor to reflect the coupling between the different electric field components. This thesis focuses on the second-order nonlinearity $P^{(2)}$ which is responsible for three-wave mixing interactions. Four-wave mixing or $\chi^{(3)}$ interactions are also used for photon-pair production and frequency conversion [16, 17] but have reduced efficiency compared to their three-wave mixing counterparts due to the larger $\chi^{(2)}$ coefficient. Four-wave mixing interactions for frequency conversion find some application when the frequency shift involved is small [18]. Recently, broadly tunable frequency conversion has been proposed and demonstrated with four-wave mixing in photonic crystal fibre [19, 20].

### 2.1.1 Second order nonlinear polarisation

From this point on we will restrict the discussion of the nonlinear polarisation to only the second-order term $P^{\mathrm{NL}} = \epsilon_0 \chi^{(2)} EE$. In general not all materials exhibit this order of nonlinearity. For materials which have inversion symmetry, $-\vec{P}\left(x,y,z\right) = \vec{P}\left(-x,-y,-z\right)$, the second order nonlinearity is zero. Consider two input electric fields with different frequencies $\omega_1$ and $\omega_2$ such that the electric field can be written as

$$E\left(t\right) = E_1 \exp\left(-i\omega_1 t\right) + E_2 \exp\left(-i\omega_2 t\right) + \text{c.c.} \tag{2.3}$$

Inserting this electric field into the nonlinear polarisation gives,

$$\begin{aligned} P^{\mathrm{NL}} = \epsilon_0 \chi^{(2)} & \left[E_1^2 \exp\left(-i2\omega_1 t\right) + E_2^2 \exp\left(-i2\omega_2 t\right)\right. \\ & + 2E_1E_2 \exp\left(-i\left(\omega_1+\omega_2\right)t\right) + 2E_1E_2^* \exp\left(-i\left(\omega_1-\omega_2\right)t\right) \\ & \left.+2\left(E_1E_1^* + E_2E_2^*\right)\right]. \end{aligned} \tag{2.4}$$

Equation (2.4) contains all second-order nonlinear interactions. The first two terms represent second-harmonic generation (SHG) at $2\omega_1$ and $2\omega_2$ respectively. The last term represents optical rectification. The most important term for this thesis is the difference-frequency term, $\omega_1 - \omega_2$. Both frequency conversion (FC) and parametric downconversion (PDC) are the same underlying process and come from this term. The main difference in the physics comes from the intensity of the fields at $\omega_1, \omega_2$ and $\omega_3 = \omega_1 - \omega_2$ before the nonlinear interaction.

$$\begin{aligned} \frac{\mathrm{d}A_1}{\mathrm{d}z} &= \kappa \frac{\omega_1}{n_1} A_2 A_3 \exp\left(i\left(k_2+k_3-k_1\right)z\right), \\ \frac{\mathrm{d}A_2}{\mathrm{d}z} &= \kappa \frac{\omega_2}{n_2} A_1 A_3^* \exp\left(-i\left(k_2+k_3-k_1\right)z\right), \\ \frac{\mathrm{d}A_3}{\mathrm{d}z} &= \kappa \frac{\omega_3}{n_3} A_1 A_2^* \exp\left(-i\left(k_2+k_3-k_1\right)z\right). \end{aligned} \tag{2.5}$$

Eq. (2.5) are the classical amplitude equations for three fields interacting in a nonlinear medium. From Eq. (2.5) two of the field amplitudes must be non-zero, for example $A_1$ and $A_2$, at the start of the nonlinear crystal for an interaction to take place and generate a new field at $A_3$. For FC this is commonly the case where $A_1$ is a single photon and $A_2$ is a strong coherent field. For PDC both $A_2$ and $A_3$ are vacuum modes; a phrase sometimes heard around the coffee table is PDC is difference-frequency generation "seeded" by vacuum. In the purely classical picture PDC cannot take place and so we must use a quantum mechanical picture of three-wave mixing.

## 2.2 Quantum treatment of three-wave mixing

To start describing the three-wave mixing interaction in a quantum mechanical framework we introduce the quantised electric field operators,

$$\begin{aligned} \hat{E}_i\left(z,t\right) &= \hat{E}_i^{+}\left(z,t\right) + \hat{E}_i^{-}\left(z,t\right) \\ \hat{E}_i\left(z,t\right) &= i\mathcal{A}\int \mathrm{d}\omega \left(\hat{a}_i\left(\omega_i\right) e^{i\left(k\left(\omega_i\right)z-\omega_i t\right)} - \hat{a}_i^{\dagger}\left(\omega_i\right) e^{-i\left(k\left(\omega_i\right)z-\omega_i t\right)}\right) \end{aligned} \tag{2.6}$$

where $\hat{a}\left(\omega\right)$ $\left(\hat{a}^{\dagger}\left(\omega\right)\right)$ are the annihilation (creation) operators for a photon at frequency $\omega$ with wave vector $k\left(\omega\right)$ and $\mathcal{A}$ is a factor which includes the transverse spatial extent of the optical mode, the optical power in the mode and other constant factors. Here we have considered a simplified paraxial description of the mode along the beam propagation direction $z$.

The three-wave mixing Hamiltonian can then be written as [21]

$$\hat{H}_{3\mathrm{WM}} \propto \int \mathrm{d}z g\left(z\right)\left(\hat{E}_1^{+} + \hat{E}_1^{-}\right)\left(\hat{E}_2^{+} + \hat{E}_2^{-}\right)\left(\hat{E}_3^{+} + \hat{E}_3^{-}\right), \tag{2.7}$$

where $g\left(z\right)$ is the normalised nonlinearity along the crystal. From Eq. (2.7) all the terms present in Eq. (2.4) can be recovered. Picking out the relevant term for FC and PDC the Hamiltonian becomes,

$$\begin{aligned}\hat{H}_{3\mathrm{WM}} &\propto \int \mathrm{d}z\, g\left(z\right) \hat{E}_1^{+} \hat{E}_2^{-} \hat{E}_3^{-} + \mathrm{h.c.} \\ &= \int \mathrm{d}z\, \mathrm{d}\omega_1 \mathrm{d}\omega_2 \mathrm{d}\omega_3 \hat{a}_1\left(\omega_1\right) \hat{a}_2^{\dagger}\left(\omega_2\right) \hat{a}_3^{\dagger}\left(\omega_3\right) \\ &\quad \exp\left(i\left[\omega_2+\omega_3-\omega_1\right]t\right) g\left(z\right) \exp\left(i\left[k\left(\omega_3\right)-k\left(\omega_1\right)-k\left(\omega_2\right)\right]z\right) + \mathrm{h.c.},\end{aligned} \tag{2.8}$$

where we have implicitly assumed the optical mode at frequency $\omega_1$ is the highest frequency field. Without loss of generality we assume the ordering of frequencies $\omega_1 > \omega_2 \geq \omega_3$. At this point we could evaluate the evolution of the fields in the Schrödinger picture as

$$\left|\psi\left(t\right)\right\rangle = \hat{\mathcal{T}} \exp\left\{\frac{-i}{\hbar}\int_0^t \mathrm{d}t' \hat{H}_{3\mathrm{WM}}\left(t'\right)\right\}\left|\psi\left(0\right)\right\rangle, \tag{2.9}$$

where $\hat{\mathcal{T}}$ is the time-ordering operator. Unfortunately as the Hamiltonian does not commute with itself at different times we cannot proceed easily with Eq. (2.9). However, the impact of the time-ordering operator can be neglected for low photon numbers in PDC ($\bar{n} \ll 1$) and low efficiency in FC ($\eta \ll 1$) [22]. For the experimental work in this thesis this approximation is valid and we can proceed with the time integral,

$$\int_{-\infty}^{\infty} \mathrm{d}t' \exp\left(i\left[\omega_2+\omega_3-\omega_1\right]t'\right) = \delta\left(\omega_2+\omega_3-\omega_1\right) \tag{2.10}$$

The limits of the time integral have been extended from $[0,t] \rightarrow [-\infty,\infty]$ based on the argument that outside the crystal the fields freely evolve and so the state is unchanged outside the region $[0,t]$, the points in time where the fields start and end interacting inside the crystal.

At this point we must make a choice to talk about PDC and FC separately. Due to the small photon-photon interaction at optical frequencies in typical crystals $\left(\chi^{(2)} \sim 10^{-12}\right)$ one of the three modes must be a classical field containing a macroscopic number of photons $(10^{15} - 10^{19}\mathrm{s}^{-1})$ in order for something to be observed in the typical integration time of an experiment.

The choice of which of the three fields is replaced by a classical field is one of the fundamental differences between PDC and FC. In PDC the classical field is the highest frequency mode such that a high energy photon can spontaneously decay into two lower energy photons. For FC either of the lower energy modes can become classical. In either case we make the substitution $\hat{a}\left(\omega\right) \rightarrow \alpha\left(\omega\right)$ with $\alpha$ a complex valued function. $\alpha\left(\omega\right)$ is often called the pump-envelope function (PEF) and describes the spectral amplitude of the mode and has the normalisation property

$$\int \mathrm{d}\omega |\alpha\left(\omega\right)|^2 = 1. \tag{2.11}$$

Making this substitution and using the delta function to remove the frequency integral over the classical field we have the PDC and FC Hamiltonians.

$$\hat{H}_{\mathrm{PDC}} = \int \mathrm{d}\omega_2 \mathrm{d}\omega_3 \mathrm{d}z g\left(z\right) \exp\left(i\Delta k\left(\omega_2, \omega_3\right) z\right) \alpha\left(\omega_2 + \omega_3\right) \hat{a}_2^\dagger\left(\omega_2\right) \hat{a}_3^\dagger\left(\omega_3\right) + \mathrm{h.c.}, \tag{2.12}$$

$$\hat{H}_{\mathrm{FC}} = \int \mathrm{d}\omega_1 \mathrm{d}\omega_2 \mathrm{d}z g\left(z\right) \exp\left(i\Delta k\left(\omega_1, \omega_2\right) z\right) \alpha\left(\omega_1 - \omega_2\right) \hat{a}_1\left(\omega_1\right) \hat{a}_2^\dagger\left(\omega_2\right) + \mathrm{h.c.}, \tag{2.13}$$

with the shorthand $\Delta k = k_i - k_j - k_k$. At this point we can identify the phase-matching function (PMF) as the spatial integral

$$\phi\left(\Delta k\left(\omega_i, \omega_j\right)\right) = \int \mathrm{d}z g\left(z\right) \exp\left(i\Delta k\left(\omega_i, \omega_j\right) z\right), \tag{2.14}$$

The PMF describes the spectral response of the nonlinear material at frequencies $\omega_i, \omega_j, \omega_i \pm \omega_j$ with the relative sign due to the differences between labelling of modes in FC and PDC. With the PMF and PEF we are able to now define the joint spectral amplitude (JSA) as

$$f\left(\omega_i, \omega_j\right)_{\mathrm{PDC/FC}} = \alpha\left(\omega_i \pm \omega_j\right) \phi\left(\omega_i, \omega_j\right), \tag{2.15}$$

where the positive sign is for PDC and the negative sign for FC.

In order to gain some more understanding the PMF, PEF and JSA are discussed in turn. The main differences between PDC and FC are highlighted for each before showing how the JSA can be reduced to a finite number of modes using the Schmidt decomposition. This modal description gives additional insight into experimentally measurable quantities such as Hong-Ou-Mandel visibilities from PDC photons. From this point we change frequency notation to refer to the downconverted photons in PDC as signal and idler and make the change $\omega_i, \omega_j \rightarrow \omega_s, \omega_i$. In FC we refer to the input and output modes as the modes which are occupied by a photon at the beginning and end of the conversion process and make the substitution $\omega_i, \omega_j \rightarrow \omega_o, \omega_i$ when referring to FC

### 2.2.1 Pump-envelope function

The PEF represents the spectral amplitude of the classical field driving the three-wave mixing process. An intuitive way to think of the PEF is to consider sending the classical field onto a spectrometer, the intensity measured would correspond to $|\alpha\left(\omega_s, \omega_i\right)|^2$ with appropriate normalisation. For ultrafast soliton mode-locked lasers like the Ti:Sapphire laser used in this thesis, the PEF is a sech function. Frequently in this thesis the sech pulse shape will be approximated as a Gaussian function to simplify analytical calculations.

For PDC the classical field is the highest frequency mode and by energy conservation the two downconverted photons must sum to the pump photon's energy. This restricts the orientation of the PEF to run from the upper left to lower right in the $(\omega_s, \omega_i)$ plane. For a Gaussian PEF with a flat spectral phase, the explicit form is given by

$$\alpha_{\mathrm{PDC}}\left(\omega_s, \omega_i\right) = \exp\left(-\frac{\left(\omega_s + \omega_i\right)^2}{2\sigma^2}\right), \tag{2.16}$$

where $\sigma$ is related to the spectral bandwidth of the pump pulse.

For FC the classical field is either the lowest or intermediate energy mode. This then restricts the PEF to run from the lower left to the top right in the $(\omega_i, \omega_o)$

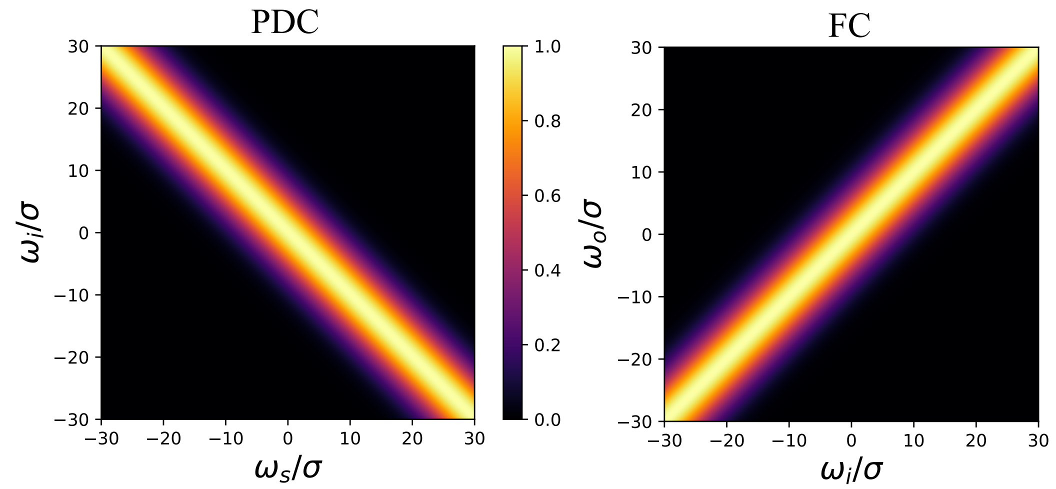

Figure 2.1: Comparison of PEF for PDC (left) and FC (right). The orientation of the PEF is fixed due to energy conservation constraints. Axes are rescaled in units of the pump bandwidth $\sigma$. For symmetric functions the labelling of $\omega_s, \omega_i$ and $\omega_i, \omega_o$ can be exchanged, this is not true for odd-functions such as a first-order Hermite-Gauss mode which will be relevant in Section 3.3.

plane. The relative orientations for FC and PDC can be seen in Fig. 2.1. Similar to Eq. (2.16), for a transform limited Gaussian PEF the explicit form is given by,

$$\alpha_{\mathrm{FC}}\left(\omega_i, \omega_o\right) = \exp\left(-\frac{\left(\omega_i - \omega_o\right)^2}{2\sigma^2}\right) \tag{2.17}$$

### 2.2.2 Phasematching function

The PMF describes the spectral response of the crystal in three-wave mixing, in this section we will discuss how the dispersion properties of the crystal affect the shape of the PMF in PDC and FC.

We have seen previously in Eq. (2.14) the PMF depends on the phase-mismatch $\Delta k$ and the nonlinearity profile along the crystal $g\left(z\right) = \chi^{(2)}\left(z\right)/\chi^{(2)}$. An important point worth highlighting is the PMF can be viewed as a Fourier transform of the nonlinearity profile $g\left(z\right)$ with respect to the wavevector mismatch $\Delta k$. For now we consider the simplest case of a bulk crystal $g\left(z\right) = 1$ inside the crystal and zero otherwise. From here we consider how the dispersion of the crystal affects the PMF. We will return to other shapes of $g\left(z\right)$ in Section 3.2.

For a bulk crystal the spatial integral can be carried out and the PMF is given by

$$\int_0^L \mathrm{d}z \exp\left(i\Delta k\right) = L \operatorname{sinc}\left(\frac{\Delta k L}{2}\right) \exp\left(\frac{i\Delta k L}{2}\right). \tag{2.18}$$

This the classic result of a sinc-shaped phasematching well known from nonlinear optics [14]. Intuitively the sinc shape can be thought of as a Fourier transform of a unit box function in the spatial domain with respect to the phase-mismatch $\Delta k$. The phase term, $\exp\left(i\Delta k L/2\right)$ results from the asymmetric choice of the crystal position around the zero position in space. An important point to note is that the width of the PMF in $\Delta k$ space is controlled by the crystal length $L$.

To understand how the PMF affects the PDC and FC process we examine the phase-mismatch $\Delta k$ and Taylor expand around the central frequencies of each mode

$$\begin{aligned} \Delta k_{\mathrm{PDC}} &= k_p - k_s - k_i \approx 0 \\ &\approx k_{p,0} - k_{s,0} - k_{i,0} \\ &+ \frac{\partial k_p}{\partial \omega_p}\Omega_p - \frac{\partial k_s}{\partial \omega_s}\Omega_s - \frac{\partial k_i}{\partial \omega_i}\Omega_i \\ &+ \mathcal{O}\left(\frac{\partial^2 k}{\partial \omega^2}\Omega^2\right), \end{aligned} \tag{2.19}$$

where $k_j = n\left(\omega_j\right)\omega_j/c$, $n\left(\omega_j\right)$ is the refractive index at frequency $\omega_j$ and $\Omega_j = \left(\omega_j - \omega_{j,0}\right)$ is the deviation from the central frequency $\omega_{j,0}$. The derivatives $\frac{\partial k_j}{\partial \omega_j} = v_j^{-1}$ are the inverse group velocities at frequency $\omega_j$. The higher-order derivatives are relevant for larger spectral ranges where group-velocity dispersion becomes important, which is not discussed in this work [23]. For a phasematched process, the zeroth order term $k_{p,0} - k_{s,0} - k_{i,0} = 0$, using this and some simple rearranging of terms leads to

$$\Omega_i = -\left(\frac{v_p^{-1} - v_s^{-1}}{v_p^{-1} - v_i^{-1}}\right)\Omega_s. \tag{2.20}$$

From Eq. (2.20) one can see contours with constant value have a gradient of,

$$m = -\left(\frac{v_p^{-1} - v_s^{-1}}{v_p^{-1} - v_i^{-1}}\right). \tag{2.21}$$

A similar calculation can be carried out for FC which gives a similar result,

$$\Omega_o = \left( \frac{v_p^{-1} - v_i^{-1}}{v_p^{-1} - v_o^{-1}} \right) \Omega_i \tag{2.22}$$

To illustrate the difference in FC and PDC, Fig. 2.2 shows the PMF for a PDC process where the idler and pump photons have the same group velocity which gives a vertical PMF in the $\omega_i, \omega_s$ plane. For the same three-wave mixing process the FC PMF can be aligned with the $\omega_i$-axis or $\omega_o$-axis depending on if the FC considered is either difference-frequency or sum-frequency generation process. The PMF for the sum-frequency generation process is the transpose of the PMF for the difference-frequency generation process and vice versa.

To accurately model real crystals including these group velocity effects it is important to understand how $n\left(\omega_j\right)$ varies with $\omega_j$. This is done using Sellmeier equations, named after Wolfgang Sellmeier who introduced the functional form of the equations that is still commonly used today. Typically the equations are written in terms of wavelength and are of the form,

$$n^2\left(\lambda\right) = 1 + \sum_j \frac{B_j \lambda^2}{\lambda^2 - C_j}, \tag{2.23}$$

where the Sellmeier coefficients $B_j, C_j$ are empirically measured for a given crystal over a particular frequency range. There are many different publications which include Sellmeier coefficients for a wonderful variety of nonlinear crystals including extra physical effects such as the temperature dependence of the refractive indices or the inclusion and concentration of different dopants in common nonlinear materials. For this thesis the Sellmeier equations are taken from [24] for potassium titanyl phosphate and from [25] for lithium niobate.

### 2.2.3 Joint spectral amplitude

The preceding sections describing the PEF and PMF have now put us in a position to describe the joint spectral amplitude. As we shall see the JSA is a powerful tool

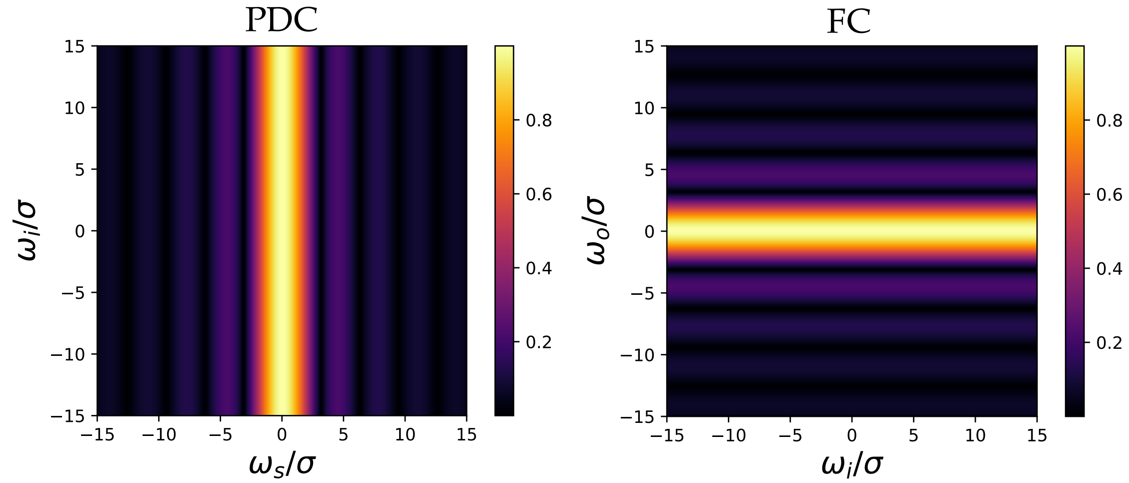

Figure 2.2: Comparison of PMF for PDC (left) and FC (right). The orientation of the PMF is determined by the group velocities of light in the material at the frequencies involved in the three-wave mixing process. There is an ambiguity in the orientation of the PMF for a FC process depending on which mode is considered the input or output. All plots show the absolute value unless otherwise stated.

for understanding PDC and FC. At this point we return to Eq. (2.12) and Eq. (2.13) and examine each process individually.

In PDC it is common to Taylor expand the unitary generated from the Hamiltonian in Eq. (2.12) to include the term in which a single pair of photons are produced. This approximation is referred to as the low-gain approximation and is a similar level to ignoring the time-ordering operator in Eq. (2.9). At this point the two-photon or biphoton state from PDC can be written as

$$\begin{aligned} |\psi\rangle &= \exp\left(\frac{-i}{\hbar}\hat{H}_{\text{PDC}}\right)|0,0\rangle \\ |\psi\rangle &\approx \left(\mathbb{I} + g\int\int \mathrm{d}\omega_s \mathrm{d}\omega_i f\left(\omega_s,\omega_i\right) a^\dagger\left(\omega_s\right) b^\dagger\left(\omega_i\right)\right)|0,0\rangle\,, \end{aligned} \tag{2.24}$$

where $\mathbb{I}$ is the identity operator and represents the term where no downconversion takes place. We have lumped the constant terms into a coupling factor $g$ which is proportional to the square root of the pump power. Looking at Eq. (2.24) the meaning of the JSA for PDC is clear, $f\left(\omega_s,\omega_i\right)$ is the probability amplitude density for finding a signal photon at freqency $\omega_s$ and an idler photon at frequency $\omega_i$. Note the state in Eq. (2.24) is unnormalised.

Using a similar Taylor expansion for the unitary generated by Eq. (2.13) under the same low-gain approximation the output of a single-photon FC process can be written as

$$\begin{aligned} |\psi\rangle &= \exp\left(\frac{-i}{\hbar}\hat{H}_{\mathrm{FC}}\right)|0,1\rangle \\ |\psi\rangle &= \exp\left(g\int\int \mathrm{d}\omega_o \mathrm{d}\omega_i f\left(\omega_o,\omega_i\right) a^{\dagger}\left(\omega_o\right) b\left(\omega_i\right) + \mathrm{h.c.}\right)|0,1\rangle\,. \end{aligned} \tag{2.25}$$

For FC the JSA describes the probability amplitude for converting an input photon at frequency $\omega_i$ to $\omega_o$.

It is important to note the difference in physical meaning for the JSA for the two different processes. In PDC the JSA tells us something about a quantum state. The JSA for FC describes how a particular input state is mapped to an output state, it describes a unitary process.

In order to develop some intuition about PDC and FC we can apply the Schmidt decomposition to Eq. (2.24) and Eq. (2.25). The Schmidt decomposition is a common technique in quantum information and gives a way to describe a bipartite quantum system in terms of an orthonormal basis for each subsystem. It has been applied to the continuous time-frequency degree of freedom in PDC [26] and FC [21].

For both PDC and FC, using the Schmidt decomposition the JSA can be written as

$$f\left(\omega_i,\omega_j\right) = \sum_k \lambda_k u_k\left(\omega_i\right) v_k\left(\omega_j\right), \tag{2.26}$$

where $u_k\left(\omega_i\right)$ and $v_k\left(\omega_j\right)$ form an orthonormal set of functions and $\lambda_k$ are the Schmidt coefficients for each pair of functions satisfying $\sum_k \lambda_k^2 = 1$.

Unfortunately there are only a few examples of functions for which the Schmidt decomposition can be calculated analytically. Typically these are products of Gaussian or Hermite-Gauss functions. The typical approach is to represent $f\left(\omega_i,\omega_j\right)$ numerically as a matrix and use the singular value decomposition to find the Schmidt modes and Schmidt coefficients. From the SVD we have that,

$$f\left(\omega_i,\omega_j\right) \approx F_{n,m} = U_{n,k} D_{k,k} V_{k,m}^{T}, \tag{2.27}$$

where the columns (rows) of $U\left(V^T\right)$ form an orthonormal basis which can be identified as the discretised versions of $u_k\left(\omega_i\right)$ and $v_k\left(\omega_j\right)$. $D_{k,k}$ is a diagonal matrix with elements equal to the singular values of the matrix $F$ which we identify as the Schmidt coefficients $\lambda_k$. For results presented in this thesis the SVD is carried out numerically on a grid of $n \times m = 2048 \times 2048$ points. From here on we will treat the Schmidt decomposition and the SVD interchangeably.

Applying the Schmidt decomposition to the biphoton state generated in PDC we have

$$\begin{aligned} |\psi\rangle &= \sum_k \int\int \mathrm{d}\omega_s \mathrm{d}\omega_i \lambda_k u_k\left(\omega_s\right) v_k\left(\omega_i\right) a^\dagger\left(\omega_s\right) b^\dagger\left(\omega_i\right) |0,0\rangle \\ &= \sum_k \lambda_k A_k^\dagger B_k^\dagger |0,0\rangle\,, \end{aligned} \tag{2.28}$$

where broadband mode operators are defined such that

$$\begin{aligned} A_k^\dagger &= \int \mathrm{d}\omega_s u_k\left(\omega_s\right) a^\dagger\left(\omega_s\right) \\ B_k^\dagger &= \int \mathrm{d}\omega_i v_k\left(\omega_i\right) b^\dagger\left(\omega_i\right)\,, \end{aligned} \tag{2.29}$$

which satisfy the commutation relation $\left[A_i, A_j^\dagger\right] = \delta_{i,j}$.

This gives a nice interpretation of a general PDC process as being built up from many pairs of orthogonal two-mode squeezed vacuum states running over the index $k$ generating a multimode two-mode squeezed vacuum state, see Fig. 2.3.

The number of effective modes in the downconversion process can be estimated using $K = 1/\sum_k \lambda_k^4$, commonly referred to as the Schmidt number. Consider the density matrix for the two photon state produced by PDC,

$$\rho_{\mathrm{PDC}} = \sum_{k,j} \lambda_k \lambda_j A_k^\dagger B_k^\dagger |0,0\rangle \langle 0,0| A_j B_j. \tag{2.30}$$

Typically when heralding a single photon from PDC the heralding detector does not resolve the frequency mode and so the heralded modes must be traced out, the

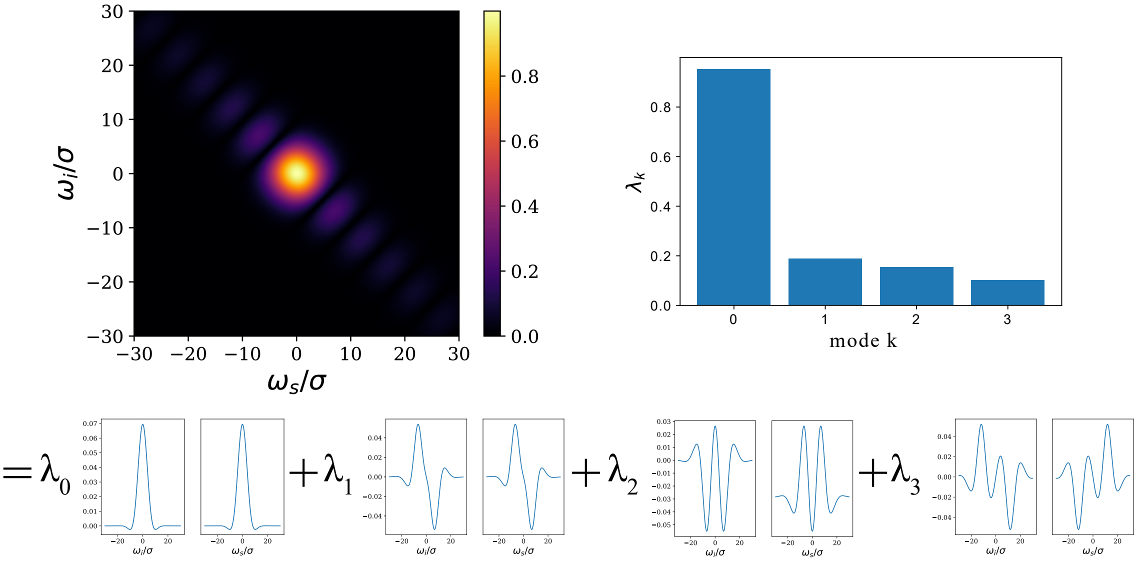

Figure 2.3: Joint spectral amplitude of a PDC process and the associated Schmidt decomposition into orthogonal signal and idler modes. The pump inverse group velocity is set to be the average of signal and idler inverse group velocities. This is the case with type-2 PDC in KTP at telecom wavelengths which is used in Chapter 3. The Schmidt number $K = 1.21$ and the purity of a heralded single-photon from this biphoton state would be 82.4%. The purity is reduced from unity due to the sinc-lobes running along the anti-diagonal which are a source of frequency anti-correlation between signal and idler photons. After heralding this frequency anti-correlation causes mixedness in the final single-photon state. The overall PDC state can be thought of as a sum of pairs of two-mode squeezers with the weights given by the Schmidt coefficients, which is shown in the lower panel.

reduced density matrix of the heralded single photon is therefore

$$\mathrm{Tr}_B\left(\rho_{\mathrm{PDC}}\right) = \rho_A = \sum_j \lambda_j^2 A_j^\dagger \left|0\right\rangle \left\langle 0\right| A_j \tag{2.31}$$

and the purity of the heralded state is then

$$\mathrm{Tr}\left(\rho_A^2\right) = \sum_j \lambda_j^4 = \frac{1}{K}. \tag{2.32}$$

From Eq. (2.32) the purity of the heralded single photon is the reciprocal of the Schmidt number. This means that for a unit purity heralded single photon there must be exactly one pair of modes contributing to the downconversion process and equivalently more than one pair of modes contributing to the downconversion process ($K > 1$) implies the photon pair is time-frequency entangled and therefore the heralded state cannot be pure. Historically these spectral correlations are removed by using tight filters to retain only the central lobe of the JSA [27]. This comes at the cost of brightness and heralding efficiency as any photons produced in these spectral regions are lost. A better option is to remove the spectral correlations by domain engineering which will be discussed in Chapter 3.

At this point it is worth highlighting a special case of Eq. (2.28) where each pair of modes has equal probability. For $d$ modes occurring with equally probability we have defined a $d$-dimensional maximally entangled state which can be written as

$$|\psi^d\rangle = \sum_k^d \frac{1}{\sqrt{d}} A_k^\dagger B_k^\dagger |0\rangle |0\rangle = \sum_k \frac{1}{\sqrt{d}} |u_k\rangle |v_k\rangle , \tag{2.33}$$

where we have defined the states $|u_k\rangle , |v_k\rangle$ as a time-frequency mode defined by Eq. (2.29) occupied by a single photon. We will return to this case in Chapter 3.

A similar calculation can be carried out for FC which leads to Eq. (2.25) being written as

$$|\psi\rangle = \exp\left( g \sum_k \lambda_k A_k^\dagger B_k \right) |0, 1\rangle , \tag{2.34}$$

which is the canonical unitary for a beam splitter transformation with beam splitter ratios given by $g\lambda_k$. This gives a clean interpretation of the frequency conversion process, an input photon in a mode defined by $B_k$ is converted to an output photon in a mode defined by $A_k^\dagger$ with an efficiency given by $\sin^2 (g\lambda_k)$. For this reason frequency conversion is sometimes called a frequency beam splitter [28].

In this case the Schmidt number is related to how single-mode the frequency conversion process is. For $K \approx 1$ only one of the beam splitters has a non-zero conversion to the output mode and all other modes are left unconverted. For $K \gg 1$ all of the input modes have approximately the same Schmidt coefficient and therefore the same conversion for the same coupling strength $g$.

To make this point more concrete let us examine a FC process in which the output photon and pump field have similar group velocities, this choice is motivated by the experimental situation described in Chapter 4.

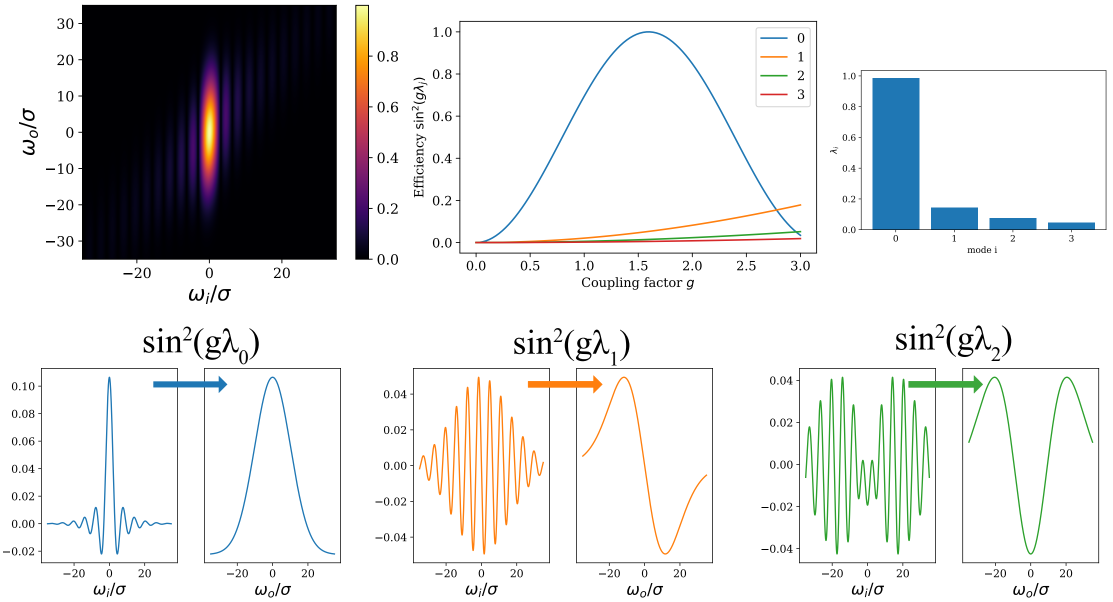

Figure 2.4: Absolute joint spectral amplitude for a FC process with group velocity matching between pump and output modes. The Schmidt number for this process is $K = 1.06$ and is therefore close to single-mode. Similar to the PDC process the increase in Schmidt number is due to the sinc-lobes visible on the diagonal of the JSA plot in the upper left panel. Looking at the Schmidt coefficients, the first mode has a coefficient approaching unity while all other modes are close to zero. This implies that only the first pair of modes (blue) are active and a photon in any other mode (orange and green) is left unchanged.

The FC process described in Fig. 2.4 has a broadband ultrafast pulse for the pump mode, where the pump bandwidth, $\sim 100$ GHz is much larger than the phasematching bandwidth $\sim 10$ GHz. For this type of pumping the JSA is approximately single-mode and only one pair of modes is converted. This case will be discussed in more detail in Section 4.5. There have been some experimental demonstrations of pulsed FC [29, 30] but the vast majority of FC experiments [31–37], including the experimental work in this thesis, are pumped by a continuous-wave laser. A CW laser has a linewidth on the order of 1 MHz or less which is considerably smaller than typical phasematching bandwidths. This leaves a highly correlated JSA with Schmidt number $K \gg 1$, shown in Fig. 2.5.

While we have described both single-mode and and multimode frequency conversion in the frequency domain an equivalent explanation exists in the time domain which supports the conclusions drawn here. For CW pumped FC the process is invariant with translation in time. Therefore the longitudinal shape of the input photon has

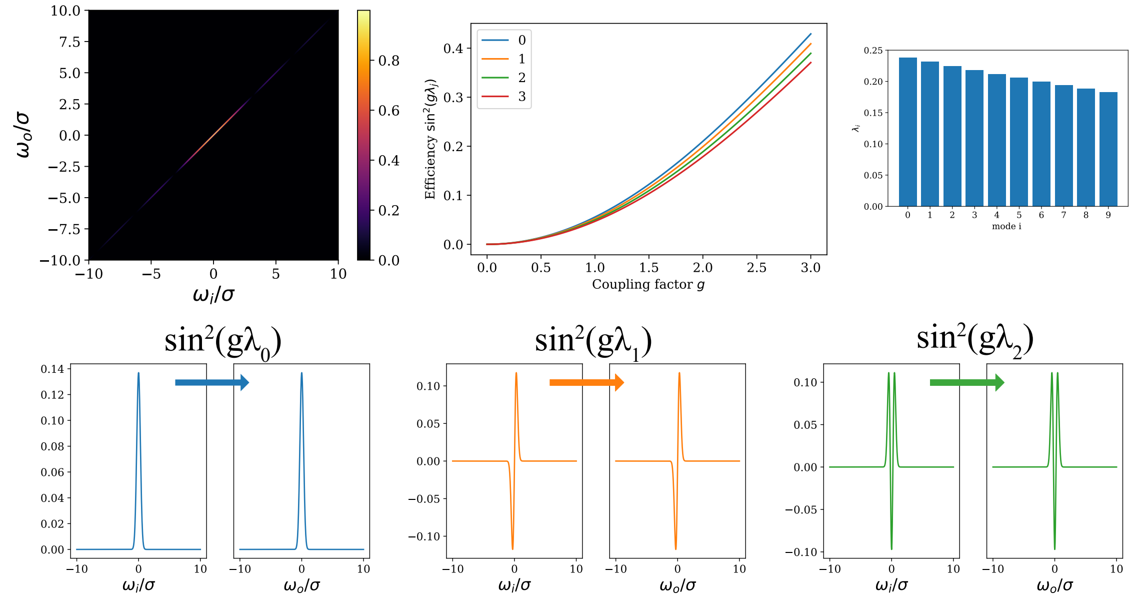

Figure 2.5: An example of a highly multimode FC process driven by a narrowband CW laser. For a highly correlated JSA there are a large number of modes with approximately similar Schmidt coefficients (upper right panel). This means that many modes have similar conversion efficiencies for the same coupling coefficient $g$ (upper centre). Since these modes have similar conversion efficiency any input mode is converted to the output mode, this is the heart of the multimode interpretation of CW FC. It is also worth noting for CW-pumped FC the input and output modes are similar shape and bandwidth, unlike the ultrafast pulsed case.

no effect on the conversion efficiency. Similarly for an ultrafast pulse which is well localised in time, there must be a time-gating effect as the three modes propagate in the crystal, which can be seen in the upper right panel of Fig. 2.6 (note the difference in time scales). This is the alternative view of the frequency selectivity seen in Fig. 2.4.

In analogy to the JSA a joint temporal amplitude (JTA) can be defined as the Fourier transform of the JSA

$$F\left(\tau_i, \tau_o\right) = \int\int \mathrm{d}\omega_i \mathrm{d}\omega_o f\left(\omega_i, \omega_o\right) \exp\left(-i\omega_i\tau_i - i\omega_o\tau_o\right). \tag{2.35}$$

Here the time parameters $\tau_i, \tau_j$ can be roughly interpreted as defining the arrival time of a photon at a detector relative to a reference clock defined by the arrival time of the pump photons [38].

The calculations presented in the previous sections could have been entirely pre-

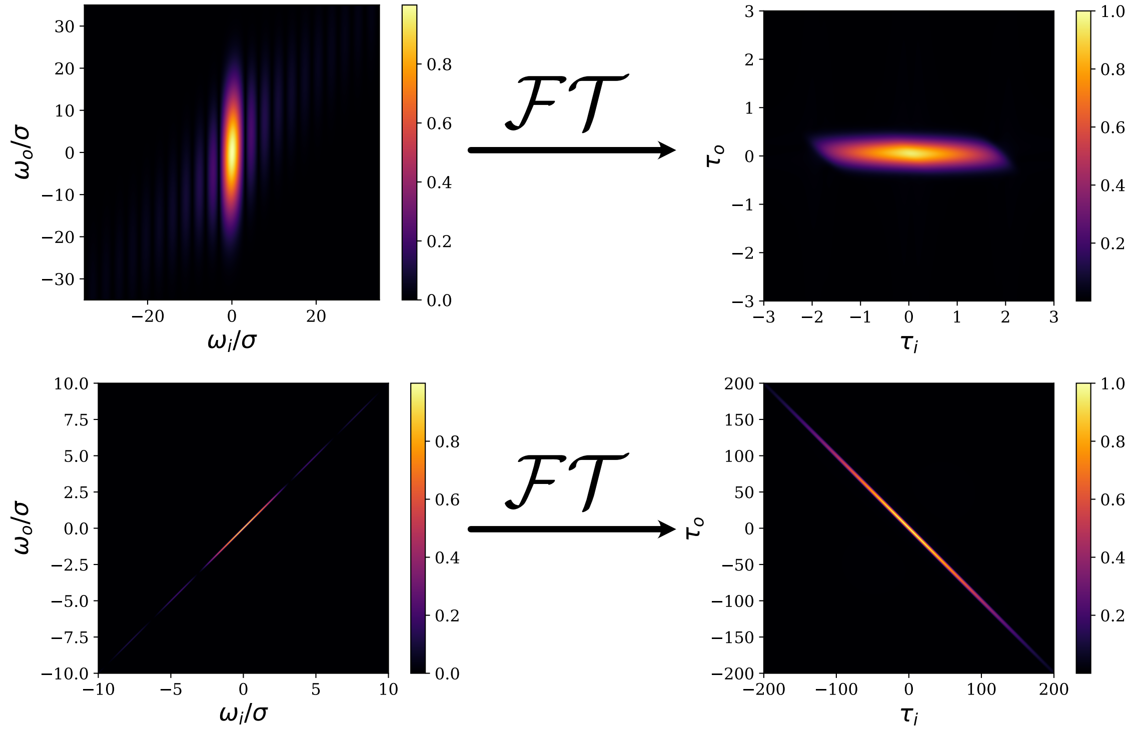

Figure 2.6: Top row shows single-mode JSA and corresponding JTA after taking a Fourier transform. The bottom row shows the multimode JSA and JTA. For the ultrafast pulsed JTA the output photons all arrive in a small window around $\tau_o = 0$, this is a result of the group-velocity matching conditions $v_p \approx v_o$. The physical interpretation is that the pump walks through the input photon and as it passes, a photon at $\omega_o$ is generated and co-propagates with the pump pulse through the crystal at the same speed and the arrival time is fixed to the arrival time of the pump. In the CW pumped multimode case the arrival time of the output photon varies as the pump intensity is constant in time. For a truly CW excitation the pump $\alpha\left(\omega_i - \omega_o\right) = \delta\left(\omega_i - \omega_o\right)$ and the JTA would be completely constant for all time. For clarity when plotting we are using long pulses in time to represent the CW case.

sented in the time domain. The frequency domain is typically preferred as the JSA is more easily measured than the JTA. The JTA would require arrival time information on the order of 1 ps resolution which is beyond direct measurement using superconducting detectors and time-tagging equipment. The JSA is easily measured using dispersive fibre-spectrometers or reconstructed by scanning narrowband filters across the input and output photon frequencies in FC [39].

We now return to the issue of phasematching and how this can be done for realistic crystals at useful wavelengths where perfect phasematching may not be possible.

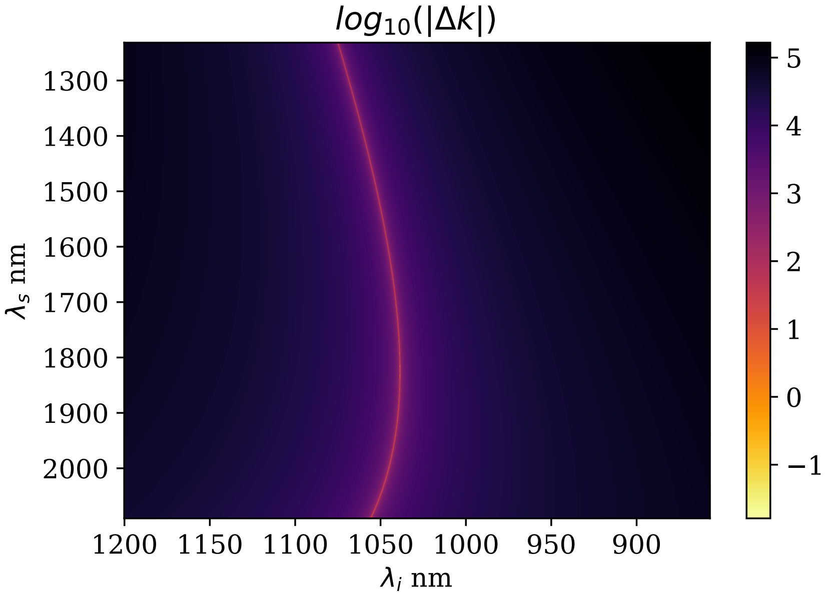

Figure 2.7: Example of the phase-mismatch $|\Delta k| = |k_p - k_s - k_i|$ for a type-2 downconversion process in KTP. If we want a photon at 1550 nm for fibre based applications then we can see that bulk phasematching only occurs with the idler photon around 1050 nm which is not a desirable wavelength in terms of detectors or propagation in fibre or free-space. The frequency axis is labelled in terms of wavelength for convenience.

## 2.3 More on phasematching

In Section 2.2.2 we made the assumption that we had perfect phasematching $\Delta k = 0$ in a bulk crystal with no spatial structure to the nonlinearity profile $g(z) = 1$ and proceeded to explain the JSA for fictitious three-wave mixing processes choosing the group velocities to highlight the physics involved. For real crystals this is a highly idealised scenario. Noncritical phasematching only occurs at specific wavelengths set by the refractive index profile for the material. This massively restricts the wavelenghts at which PDC or FC can take place. One can tune the emission wavelength using critical phasematching, where the angle of the three fields is changed with respect to the crystal axes. This offers wider tunability in terms of emission wavelengths. The downside of this is the beams experience spatial walk-off due to the birefringence of typical $\chi^2$ crystals, this reduces the length of the interaction region and therefore increases the power required for a given brightness in PDC or efficiency in FC.

Fortunately these problems were solved with the idea of quasi-phasematching intro-

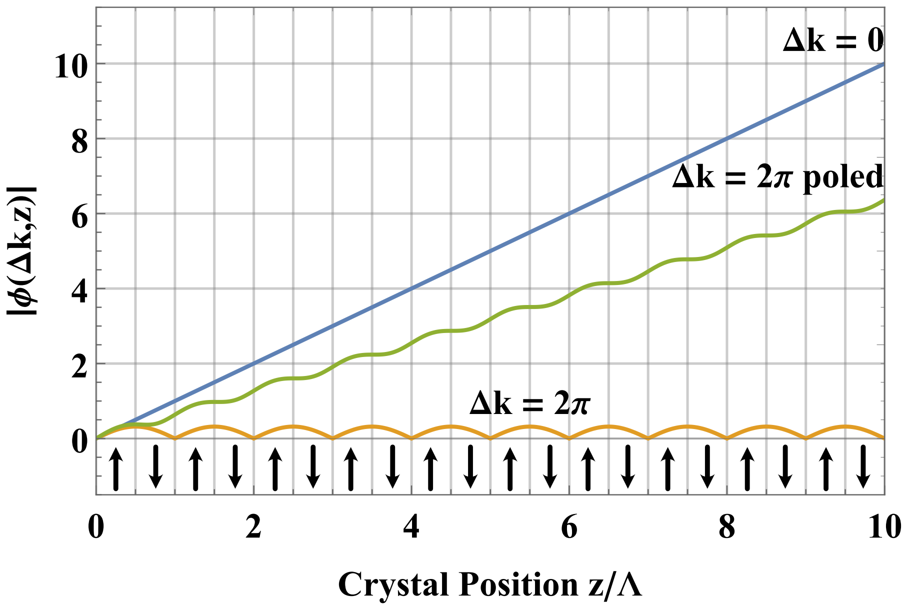

Figure 2.8: Plot comparing the bulk phasematching $\phi_b\left(\Delta k = 0\right)$ (blue) and $\phi_b\left(\Delta k = 2\pi\right)$ (orange). The same phase-mismatch is plotted for a periodically poled crystal with the poling-period set for quasi-phasematching $\Lambda = 2l_c = \frac{2\pi}{\Delta k} = 1$. The quasi-phasematched PMF amplitude oscillates around a line with gradient equal to $2/\pi$, the bulk phasematching gradient is equal to one.

duced in [40, 41]. If we consider again the classical coupled amplitude equations for three-wave mixing Eq. (2.5), we can see the phase term $\exp\left(i\Delta kz\right)$ oscillates on a period equal to $\Lambda = \dfrac{2\pi}{\Delta k}$. After one half-period the amplitude of the generated fields reaches a maximum, after this point the amplitude decreases again to return to zero, see orange curve Fig. 2.8. This half-period is commonly referred to as the coherence length $l_c$. The idea behind quasi-phasematching is that after one half-period the sign of the nonlinearity coefficient $g\left(z\right)$ is flipped from $+1 \rightarrow -1$. At this point when the generated fields would have previously decreased in amplitude they begin to increase again (Fig. 2.8 green curve) but at a lower rate than a perfect bulk phasematched process (Fig. 2.8 blue curve). This process of flipping the sign of $g\left(z\right)$ each coherence length is commonly done by inverting the ferroelectric domains of the crystal using high voltage electrodes and is called periodic poling [42]. It should be noted that this is not the only method for introducing quasi-phasematching but is by far the most common for crystals with a $\chi^{(2)}$ nonlinearity. Quasi-phasematching can also be realised by modulating the width of an optical fibre or waveguide [43] which may find application in $\chi^{(3)}$ systems.

Returning again to the general definition of the phasematching function, the PMF up to a point $z$ in the crystal can be written as

$$\phi\left(\Delta k, z\right)=\int_{\infty}^{z} \mathrm{d}z' g\left(z'\right)\exp\left(i\Delta k z'\right). \tag{2.36}$$

So for a bulk phasematched process where $g\left(z\right)=1$ the phasematching function up to a point in the crystal is given by

$$\phi_b\left(\Delta k, z\right)=z\exp\left(i\frac{\Delta k z}{2}\right)\operatorname{sinc}\left(\frac{\Delta k z}{2}\right). \tag{2.37}$$

One can see the from Eq. (2.37) that the PMF amplitude increases linearly with crystal length for $\Delta k = 0$ which can be seen in Fig. 2.8. It is also worth noting that the bandwidth of the sinc function decreases as one would intuitively expect, a wider box function (longer crystal) in real space results in a narrower Fourier transform in $\Delta k$ space.

As we have previously stated a periodically poled crystal inverts the sign of $g\left(z\right)$ every coherence length. The phasematching function for such a crystal can be written as

$$\begin{aligned}\phi_{pp}\left(\Delta k\right) &= \sum_{n=1}^{N}\int_{(n-1)l_c}^{nl_c}\mathrm{d}z\left(-1\right)^{n-1}\exp\left(i\Delta k z\right)\\ &= \underbrace{L\exp\left(i\left(\Delta k-\frac{\pi}{l_c}\right)\frac{L}{2}\right)\operatorname{sinc}\left(\left(\Delta k-\frac{\pi}{l_c}\right)\frac{L}{2}\right)}_{\phi_b\left(\Delta k-\frac{\pi}{l_c}\right)}\underbrace{\frac{1-\exp\left(i\Delta k l_c\right)}{1+\exp\left(i\Delta k l_c\right)}\frac{\Delta k-\frac{\pi}{l_c}}{\Delta k}}_{\phi_{\mathrm{add}}\left(\Delta k\right)}\end{aligned} \tag{2.38}$$

The explicit steps for deriving Eq. (2.38) are included in Appendix A. The PMF for a periodically-poled crystal can be seen as having two parts, the first term is the same bulk PMF but with the peak shifted to $\Delta k = \frac{\pi}{l_c}$. The second term is due to the poling structure, a point worth noting is that when $\Delta k = \frac{\pi}{l_c}$ this term is equal to $\frac{i2}{\pi}$ using L'Hôpital's rule. The upshot of these two points is that by choosing the correct poling-period we can phasematch any combination of wavelengths, with long interaction regions as the beams are collinear. The cost of this is that the PMF amplitude is reduced by a factor of $\frac{2}{\pi}$ compared to bulk phasematching. Depending on the wavelengths involved fabricating domain sizes $l_c = \Delta k/\pi$ might not be possible, in this case longer domains $l_c = m\Delta k/\pi$ with $m = \{3, 5, ...\}$ can be used to induce higher order quasi-phasematching. The efficiency of this type of process is reduced by $1/m^2$ compared to the case where $l_c = \Delta k/\pi$. Higher order phasematching will become relevant for the discussions in Section 4.5.6.

A reasonable question to ask is what happens if we change the poling structure to no longer have the up-down-up structure shown in Fig. 2.8. The next chapter will focus on how we can use aperiodic poling structures to make tailored shapes for the PMF. With the symmetric group-velocity condition available in type-2 KTP one can make sources of photons entangled in time and frequency at telecom wavelengths that are no more complicated to use than a standard periodically poled crystal.

# Chapter 3

# Time-Frequency entangled photon pairs

## 3.1 Aperiodic poling

The idea of aperiodic poling of nonlinear crystals was initially thought of in a classical context and dates back to the late 90s for applications in ultrafast pulse compression and shaping [44–46]. The transition to consider aperiodic poling for quantum optics applications happened more recently [47]. In Chapter 2 we discussed how spectral correlations reduce the purity of a heralded single photon produced using PDC. The solution to this problem was to filter the biphoton state to eliminate the spectral correlations at the cost of brightness and heralding efficiency.

An arguably better option is to design the phasematching of the PDC process to only allow for downconversion in a single pair of modes. It can be shown theoretically that the maximum purity is achieved for a product of a Gaussian PEF and Gaussian PMF [48]. It can also be shown that for an arbitrary PEF or PMF the purity is maximised if the other function is a Gaussian. While these results were not known at the time it was clear the sinc-lobes produced by standard periodically poled crystals were a limiting factor in the purity of heralded single-photon sources. The question then becomes how should the poling structure be changed to create a Gaussian function in the PMF.

The first work in this direction was from Branczyk et al. who showed by interleaving different periodic poling orders, an approximately Gaussian nonlinearity profile could be constructed by superposing box functions of varying width and amplitude corresponding to the different poling orders [47]. This then results in an approximately Gaussian PMF due to the Fourier transform relation between the nonlinearity profile and PMF.

Since this work there has been a variety of improvements on choosing the poling structure to closely match the desired nonlinearity profile. Previous work has kept the poling period fixed but varying the duty-cycle, the width of an "up" domain compared to a "down" domain [49, 50]. Machine learning techniques have also been applied to the problem [51] as well as high-level metaheuristic optimisation schemes [52]. Tambasco et al. [53] introduced a deterministic and computationally cheap algorithm for creating a poling structure based on tracking the PMF amplitude along the crystal in the $z$-direction. This work was then extended by Graffitti et al. [54] to work with sub-coherence length domain which are smaller than $l_c = \Delta k/\pi$. The work in this thesis is based on [54], but given the relatively long 30 mm crystals used and the typical coherence length for the down conversion process considerered $\approx 23\mu$m the sub-coherence aspect of the algorithm was not used. The designs presented later in this chapter were tested with one, two and three domains per coherence length but the increased number of domains did not impact the results. Sub-coherence engineering is expected to be important in short crystals matched to femtosecond pulsed lasers. For the designs presented in this thesis the work of [53] and [54] are therefore similar with the main difference being [53] choosing the orientation of "poling blocks" consisting of two adjacent domains and [54] choosing the orientation of each domain individually.

The key elements of the design process are outlined here with the example of a Gaussian PMF as the desired outcome, this is the basis of the experimental work presented in [55, 56]. How these steps can then be applied to make time-frequency encoded states is then presented in Section 3.3.

## 3.2 Design process for aperiodic poled crystals

The initial step in designing a poling structure for a particular PMF is of course choosing the desired PMF shape. A relatively straightforward example with practical relevance is a Gaussian PMF

$$\phi_{\text{target}}\left(\Delta k\right) = \exp\left(-\frac{1}{2}\left(\Delta k - \Delta k_0\right)^2 \sigma^2\right), \tag{3.1}$$

where $\Delta k_0$ is the phase mismatch for the desired signal and idler wavelengths and $\sigma$ controls the width of the Gaussian function. As discussed previously the nonlinearity profile is related to the PMF by a Fourier transform

$$\begin{aligned} g_{\text{target}}\left(z\right) = \mathcal{F}\left[\phi_{\text{target}}\left(\Delta k\right)\right] &= \frac{1}{\sqrt{2}}\int_{-\infty}^{\infty} \mathrm{d}\Delta k\, \phi_{\text{target}}\left(\Delta k\right)\exp\left(i\Delta k\right) \\ &= \frac{1}{\sigma}\exp\left(i\Delta k_0\right)\exp\left(-\frac{z^2}{2\sigma^2}\right). \end{aligned} \tag{3.2}$$

At this point you might protest that previously $g\left(z\right) = \{-1, +1\}$ and so how could we have a continuous function? In this sense the target nonlinearity profile is fictitious but persevering on we will see that this isn't a problem. The unintuitive next step is to work out how the PMF amplitude varies along the propagation direction in the crystal similar to Eq. 2.36 which depends on $z$ and $\Delta k$. For the Gaussian nonlinearity profile this is calculated as

$$\begin{aligned} \phi_{\text{track}}\left(z, \Delta k\right) &= \int_{-\frac{L}{2}}^{z} \mathrm{d}x g_{\text{target}}\left(x\right)\exp\left(-i\Delta k x\right) \\ &= \sqrt{\frac{\pi}{2}}\exp\left(-\frac{1}{2}\left(\Delta k - \Delta k_0\right)^2\sigma^2\right)\left[\operatorname{erf}\left(\frac{z + i\left(\Delta k - \Delta k_0\right)\sigma^2}{\sqrt{2}\sigma}\right)\right. \\ &\left. + \operatorname{erf}\left(\frac{-L + 2i\left(\Delta k - \Delta k_0\right)\sigma^2}{2\sqrt{2}\sigma}\right)\right], \end{aligned} \tag{3.3}$$

where erf is the error function. At this point we have been working with the convention of the crystal position centered at $z = 0$, we can change this to have the crystal begin at 0 and extend to $L$ with the replacement $z \to z - \frac{L}{2}$ which results in

$$\begin{aligned}\phi_{\text{track}}\left(z, \Delta k\right) = \sqrt{\frac{\pi}{2}} \exp\left(-\frac{1}{2}\left(\Delta k - \Delta k_0\right)^2 \sigma^2\right) \\ \times \left[\operatorname{erf}\left(\frac{z - \frac{L}{2} + i\left(\Delta k - \Delta k_0\right)\sigma^2}{\sqrt{2}\sigma}\right) + \operatorname{erf}\left(\frac{-\frac{L}{2} + i\left(\Delta k - \Delta k_0\right)\sigma^2}{\sqrt{2}\sigma}\right)\right].\end{aligned} \tag{3.4}$$

It is instructive to compare the PMF for the Gaussian PMF and the equivalent equation for a bulk crystal. These are shown in 3.1(a) and 3.1(b).

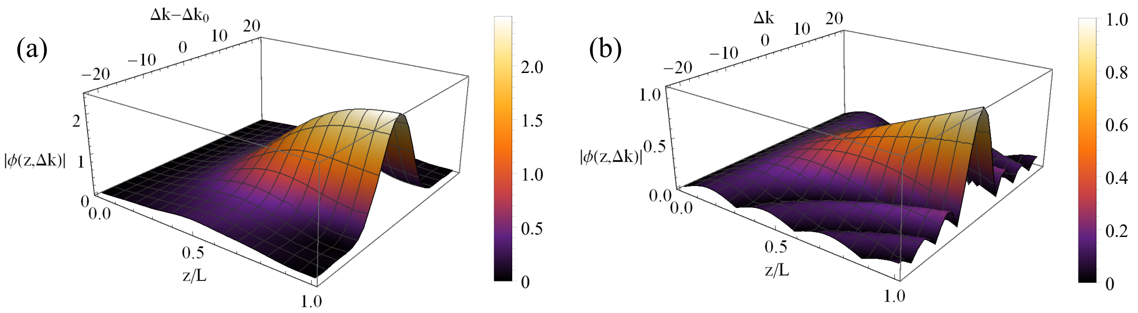

Figure 3.1: Comparison of PMF for a Gaussian crystal and a bulk phasematching crystal. The parameters for the Gaussian PMF are chosen to match those in [56]. The contour along $\phi\left(z = L/2, \Delta k\right)$ at the end of the crystal is the PMF that appears in the JSA in the previous chapter. The contour along $\phi\left(z, \Delta k = \Delta k_0\right)$ for the Gaussian crystal and $\phi\left(z, \Delta k = 0\right)$ for the bulk crystal is equivalent to the plots in Fig. 2.8.

Paying close attention to the amplitude along the crystal one can see the amplitude in the Gaussian crystal is larger than the bulk phasematching crystal at the end of the crystal. This seems strange as we know a periodically poled crystal, which is optimum in terms of increasing the amplitude for a non-phasematched process has a smaller gradient than bulk phasematching (see Fig. 2.8). The issue is that the function describing the Gaussian PMF in Eq. (3.4) is unphysical, the amplitude increases faster than the periodically poled case along the crystal. The next step in the process is to find the maximum gradient of Eq. (3.4) and set it equal to the periodic poling gradient of $2/\pi$.

At this point we define a normalisation factor $N$ which when multiplied into equation Eq. (3.4) reduces the maximum gradient to $2/\pi$

$$N = \frac{2/\pi}{\max\left\{\frac{\mathrm{d}}{\mathrm{d}z}\phi_{\mathrm{track}}\left(z, \Delta k = \Delta k_0\right)\right\}}. \tag{3.5}$$

It is worth noting this normalisation factor is not general and must be calculated on a case-by-case basis as the functional form of the PMF is changed. The final step is then to feed the PMF along the crystal at $\Delta k = \Delta k_0$ into the tracking algorithm which decides on a domain-by-domain basis the orientation of each domain. For the Gaussian crystal example the final PMF used is then,

$$\phi_{\mathrm{track}}\left(z, \Delta k = \Delta k_0\right) = \sigma\sqrt{\frac{2}{\pi}}\left[\mathrm{erf}\left(\frac{z-\frac{L}{2}}{\sqrt{2}\sigma}\right) + \mathrm{erf}\left(\frac{L}{2\sqrt{2}\sigma}\right)\right], \tag{3.6}$$

which includes the normalisation factor $N = \frac{2\sigma}{\pi}$. The entire design process is summarised in Fig. 3.2

The details of the domain-by-domain tracking algorithm used to decide the orientation of each domain is explained in detail in [54]. This process is quite robust and capable of designing a wide variety of different PMF shapes. There are a few points which must be considered in order for the method outlined to accurately reproduce the desired PMF. Changing the poling structure away from a periodically poled design will always reduce the effective length of the nonlinearity profile. This has two effects, the phasematching bandwidth is increased due to the Fourier relationship between $\phi\left(\Delta k\right)$ and $g\left(z\right)$. Secondly, the smaller nonlinearity reduces the effective brightness of the source. All other factors being equal a periodically poled crystal will produce more photons per unit pump power than an aperiodically poled crystal. Typically this isn't an issue, the reduction in nonlinearity can be compensated by using more pump power which will then give an equivalent squeezing. As we will see in Section 3.5, quite exotic PMF shapes can be made while still having a reasonable source brightness. If the same laser is driving a large number of sources then this power overhead may not be available, however multiphoton experiments involving up to six photons [57, 58], as well as the demonstration of Gaussian Boson Sampling with a 76-photon coincidence [59] have been demonstrated using aperiodically poled

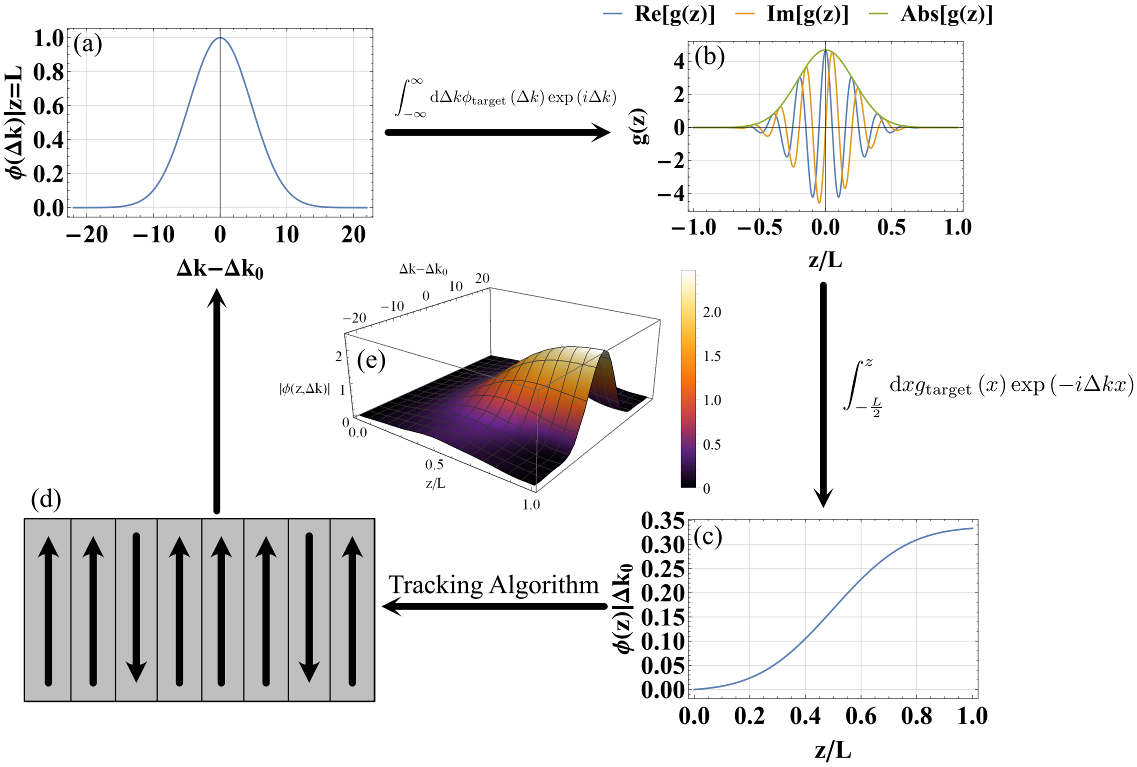

Figure 3.2: The different steps of the design process are summarised in each panel. The process starts in panel (a) where a target PMF is selected. This is the desired PMF at the end of the crystal and the function that ultimately goes into the JSA. From this PMF the nonlinearity profile shown in panel (b) is defined by a Fourier transform relationship with the PMF. From this nonlinearity profile the PMF amplitude up to an arbitrary point in the crystal is defined in panel (c). This amplitude along the crystal is then fed into a tracking algorithm which decides the domain orientation in order to minimise the difference between the target amplitude and the amplitude in the crystal. This poling structure then generates the desired PMF. It should be noted that the functions in panel (a) and (b) are really two halves of a more complete description of the PMF which is shown in panel (e).

crystals.

## 3.3 Time-Frequency encodings

Having discussed how the shape of the PMF can be modified with aperiodic poling the next question is what functions should we chose to encode qubits/qudits in the time-frequency DoF. There are broadly three different ways to encode in time and frequency, time-bin encoding, frequency-bin encoding and “pulse-mode” encodings.

Fig. 3.3 shows how the three encoding schemes fit together to effectively “tile” the time-frequency space.

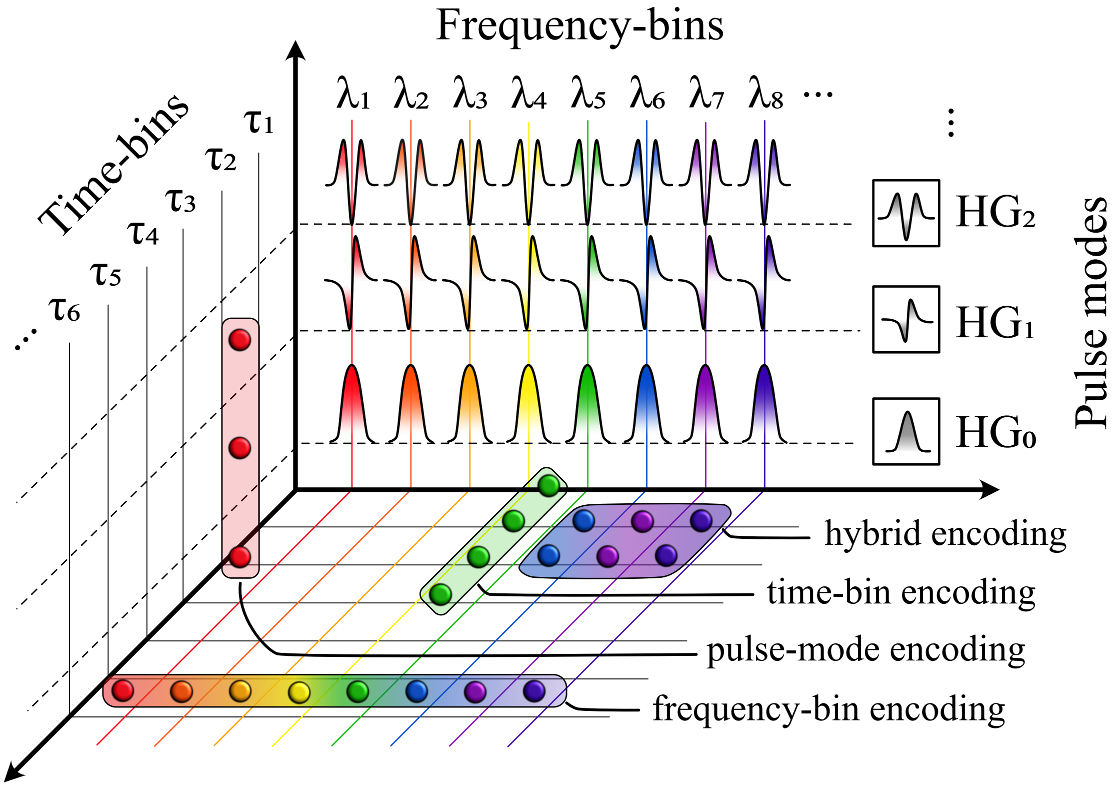

Figure 3.3: Encoding schemes in the time-frequency domain. Time-bin encoded states shown in green, encode bits in the arrival time of the photon $\tau_i$. Frequency-bin encoded states use the colour of the photons to encode information, $\lambda_i$. Pulse-mode encoding uses the longitudinal modes of single photons, here represented by Hermite-Gaussian modes, to encode information. Provided the time and frequency scales are well separated [60] information can be encoded in a hybrid manner using combinations of time-bins, frequency-bins and pulse modes, shown here with two time-bins and three frequency-bins (purple rectangle).

Time-bin encoding is arguably the oldest way to encode information in the time-frequency DoF. A time-bin qubit is defined as a photon arriving early $|e\rangle = |0\rangle$ or late $|l\rangle = |1\rangle$ relative to a clock signal. Considering a simplified Gaussian profile with two time-bins the temporal amplitude is of the form

$$\int \mathrm{d}t f\left(t\right) a^{\dagger}\left(t\right)|0\rangle = N \int \mathrm{d}t \left[\alpha \exp\left(-\frac{\left(t-\delta\right)^2}{2\sigma^2}\right) + e^{i\phi}\beta \exp\left(-\frac{\left(t+\delta\right)^2}{2\sigma^2}\right)\right] a^{\dagger}\left(t\right)|0\rangle\,, \tag{3.7}$$

where $N$ is a normalisation constant, $2\delta$ is the temporal separation between the bins and the encoded state is determined by the amplitudes $\alpha, \beta$ and the phase $\phi$. The dimensionality of the encoding space can be increased by adding other terms with increased time delay, $n\delta$ where $n \geq 2$. For orthogonality the separation between the time-bins should be much larger than the width of the individual bins.

Time-bin encoded states are manipulated using unbalanced interferometers with phase-shifters to control the relative phase $\phi$ and detected using standard single-photon detectors to resolve the arrival time [9, 61]. Time-bin states are particularly suited to quantum communication protocols due to the stability of the phase $\phi$. In order for a state of the form given by Eq. (3.7) to decohere the properties of the communication channel, either fibre or free-space must vary on a time scale on the order of $\delta$ which is typically nanoseconds. This means that the communication channel is an identity channel for time-bin encoded states, a clear advantage over polarisation encoded photons.

Time-bin encoded states can be represented in the frequency domain by taking a Fourier transform of $f\left(t\right)$,

$$\begin{aligned}\int \mathrm{d}\omega \mathcal{F}\left[f\left(t\right)\right] a^{\dagger}\left(\omega\right)\left|0\right\rangle = N' \int \mathrm{d}\omega \exp\left(-\frac{\omega^2\sigma^2}{2}\right) \\ \times \left[\alpha\cos\left(\omega\delta\right) + \beta\cos\left(\omega\delta - \phi\right)\right. \\ \left. + i\alpha\sin\left(\omega\delta\right) - i\beta\sin\left(\omega\delta - \phi\right)\right] a^{\dagger}\left(\omega\right)\left|0\right\rangle .\end{aligned} \tag{3.8}$$

In the frequency domain a photon encoded in time bins has a sinusoidal modulation in the amplitude. This is a hint that if we want to have time-bin encoded photons, the PMF as represented in Fig. 2.2 should have a sinusoidal modulation. This idea is revisited again in Section 3.7.1 taking into account real crystal parameters. Equivalently a frequency-bin encoded state can be written in the same way as Eq. (3.7) with the substitution $t \rightarrow \omega$

$$\begin{aligned}&\int \mathrm{d}\omega f\left(\omega\right) a^{\dagger}\left(\omega\right)\left|0\right\rangle \\ &= N \int \mathrm{d}\omega \left[\alpha \exp\left(-\frac{\left(\omega - \delta\right)^2}{2\sigma^2}\right) + e^{i\phi}\beta\exp\left(-\frac{\left(\omega + \delta\right)^2}{2\sigma^2}\right)\right] a^{\dagger}\left(\omega\right)\left|0\right\rangle\end{aligned} \tag{3.9}$$

and a similar equation to Eq. (3.8) exists with $\omega \rightarrow t$ for the frequency-bin representation in the time domain. The development of frequency-bin photonics has been a more recent addition to the time-frequency degree of freedom, photons are localised in discrete regions of frequency space. An advantage of encoding in frequency-bins is the carrier frequency for telecom wavelength photons is around 190 THz, given a picosecond duration photon is around 400 GHz, there is a naturally large encoding space available. Frequency-bins are manipulated and detected using electro-optic modulators [62] and Fourier transform pulse shapers, which can in principle be lossless [63]. This experimental complexity in manipulating frequency-bin encoded states comes from needing to change the frequency of a single photon including putting a single photon in a superposition of different frequencies. The upside of this experimental complexity is that frequency-bins are extremely robust to environmental noise, propagation along an optical fibre or free space does not change the central frequency of a single photon. Despite this experimental complexity, recent developments in coherent control of frequency-bins has allowed for full tomography of frequency-bin entangled photon pairs [64, 65] and generation of on-chip cluster states [60].

A third encoding in the time-frequency DoF is the "pulse-mode" encoding. Pulse-modes are overlapping in arrival-time and spectrum and are non-orthogonal in intensity, unlike time-bin and frequency-bin states. Their orthogonality exists at the amplitude level when considering the temporal or spectral phase. The idea of pulse-modes started with initial studies of PDC where the Schmidt decomposition was used to write down the effective modes of the process. For a JSA similar to Fig. 2.3 the biphoton generated is naturally encoded in pulse-modes [26] which are approximately Hermite-Gauss functions. Using the Hermite-Gauss basis pulse-mode encoded states are written as,

$$\left|\psi_n\right\rangle = \int \mathrm{d}\omega f_n\left(\omega\right) a^\dagger\left(\omega\right)\left|0\right\rangle = \int \mathrm{d}\omega H_n\left(\frac{\omega}{\sigma}\right) \exp\left(-\frac{\omega^2}{2\sigma^2}\right) a^\dagger\left(\omega\right)\left|0\right\rangle, \tag{3.10}$$

where $H_n\left(x\right)$ is the n-th order Hermite polynomial. An important point to note is the mode defined by Eq. (3.10) has the same form in the time domain as $f_n\left(\omega\right)$ is an eigenfunction of the Fourier transform. With the introduction of the quantum pulse gate [66], which is a mode selective FC process, similar to the single-mode process outlined in Fig. 2.4, it became possible to coherently manipulate and project onto pulse-modes. Unitary transformations between different pulse-modes requires cascaded FC steps which has so far limited their use to proof-of-principle demonstrations of quantum information primitives [67] although this may change in the future.

## 3.4 The role of group velocity

Having hinted at different PMF shapes which could be used to generate photons encoded in time and frequency we return to the idea of group-velocity matching and how this affects the type of state encoded, by tuning the group-velocity-matching conditions the biphoton generated can be tuned from maximally entangled to almost completely separable.

To illustrate this point consider a PMF which consists of two Gaussian functions that are centred at $\Delta k = \{-\delta, +\delta\}$ respectively for some separation $\delta$.

For the case of symmetric group-velocity matching introduced in Fig. 2.3 the pump inverse group velocity is equal to the mean of signal and idler inverse group velocity $v_p^{-1} = \left(v_s^{-1} + v_i^{-1}\right)/2$. For this case the PMF is aligned perpendicularly to the PEF. This case is illustrated in Fig. 3.4. The resulting state can be written as

$$|\psi\rangle = \frac{1}{\sqrt{2}}\left(|+\delta\rangle\,|-\delta\rangle + |-\delta\rangle\,|+\delta\rangle\right). \tag{3.11}$$

This biphoton state generated with symmetric group-velocity matching is maximally entangled in frequency-bins. It is worth noting for a state that is not separable, the exchange symmetry between signal and idler is a sufficient but not necessary condition for entanglement. Consider the case if the PMF was not centered at $\{-\delta, +\delta\}$ but $\{-2\delta, +\delta/2\}$ for example, this state has no exchange symmetry but is still maximally entangled.

If we now consider the case for an asymmetric group-velocity matched PDC process where the PMF is aligned to either the signal or idler axis. As a concrete example

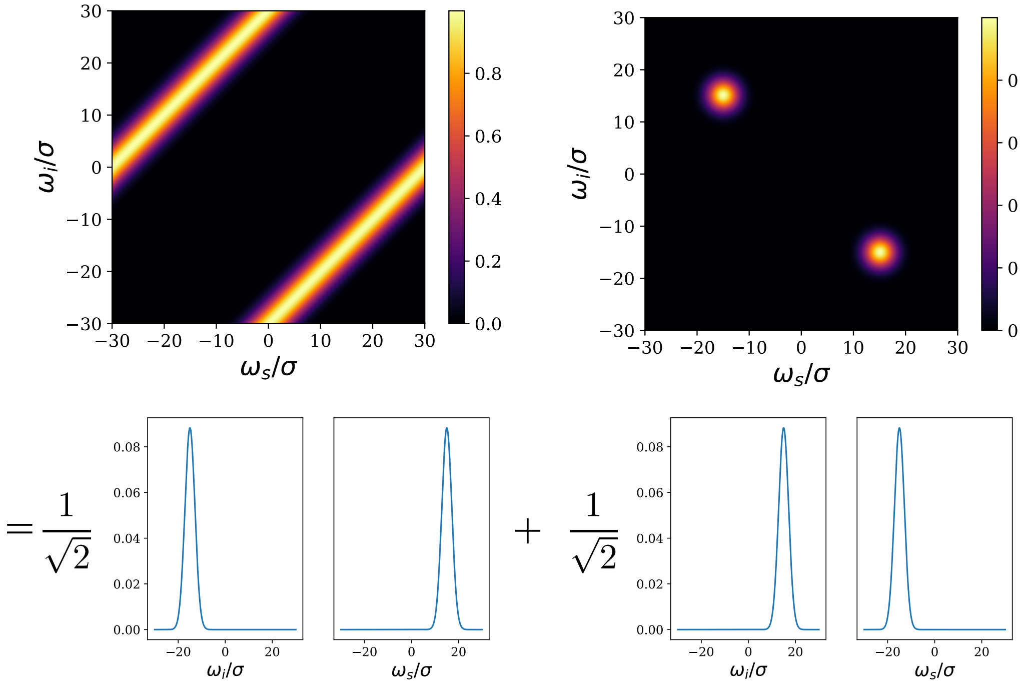

Figure 3.4: A frequency-bin entangled stated for two frequency bins. The two Gaussian PMFs are shown in the upper left corner. The JSA is shown in the upper right, with the PEF bandwidth matched to the PMF bandwidth. The Schmidt decomposition is shown in the lower half with the Schmidt modes consisting of well separated Gaussian functions. The Schmidt number for this example is exactly $K = 2$.

we will use the idler axis in this example. For this arrangement and the pump bandwidth sufficiently larger than the PMF bandwidth the resulting biphoton state is approximately separable. This is shown in Fig. 3.5.

The asymmetric group-velocity-matching condition then allows for heralded photons in particular time-frequency shapes to be generated by shaping the PMF appropriately. The symmetric-group-velocity matching condition allows a biphoton to be generated which is maximally entangled in a particular time-frequency encoding by shaping the PMF.

The path forward from this point is clear, pick a particular time-frequency encoding, from this decide the appropriate shape of the PMF. From here find a particular crystal that has the correct group-velocity-matching conditions at the wavelengths of interest for either an entangled biphoton or for producing a shaped heralded photon.

Luckily KTP has symmetric group-velocity-matching at telecom wavelengths for

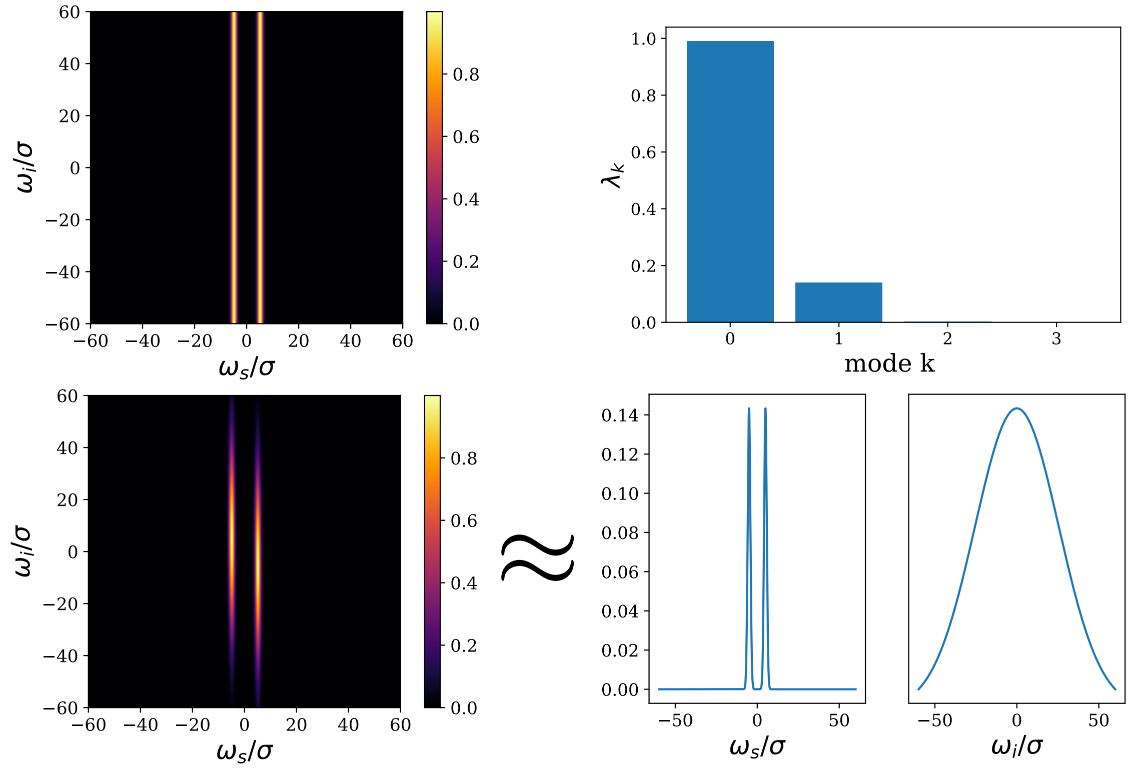

Figure 3.5: An almost pure single photon with two frequency bins could be generated by heralding on the idler photon for this case. The two Gaussian PMFs are shown in the upper left corner, aligned parallel to the idler axis. The Schmidt decomposition is shown in the upper right with one dominant mode with $\lambda_0 \approx 1$. The dominant pair of Schmidt modes is shown in the lower right. For this process the Schmidt number is $K = 1.04$ and therefore the purity of the heralded frequency bin state is 96%. An equivalent JSA (lower left) exists with the PMF aligned to the signal axis, in this case the shaped photon would be the idler.

type-2 phasematching. Using KTP with domain engineering has generated almost entirely separable Gaussian biphotons mentioned previously [55, 56] and recently by shaping the PMF to a first order Hermite-Gauss function generated a maximally entangled singlet state in pulse-modes [68]. Extending this work we use the same recipe to generate an eight-mode frequency-bin entangled source of photons around 1555 nm.

## 3.5 Experimental eight-mode frequency-bin entanglement

At this point it is important to highlight the motivation and possible advantages to moving to a frequency-bin design over previous work on pulse-modes [68]. While pulse-modes can be encoded in a high-dimensional $d > 2$ space it is difficult to produce maximally entangled state in $d > 2$. Naively, since shaping the PMF to a first order Hermite-Gauss function gives a maximally-entangled state in $d = 2$, one might imagine using a higher-order Hermite-Gauss mode might give a maximally entangled state in $d > 2$. Unfortunately this type of state has unequal Schmidt coefficients and is not maximally entangled [69]. Fortunately, frequency-bin and time-bin encodings do not have such restrictions, adding an additional bin with the same amplitude increases the dimension of the encoding space by one. For the remainder of this section we will focus on the eight-bin crystal tested experimentally, and return to potential time-bin encodings at the end of Section 3.7.1.

A second question one might ask is why would you use domain engineering to generate a frequency-bin entangled state? One could in principle take a pair source with a broadband correlated JSA and use a series of filters to generate discrete frequency-bin entanglement. This may be appealing as the bin spacing and bandwidth is set by the choice of optical filters with GHz bandwidths with 10s of GHz spacing available with a typical Fabry-Perot filter [70]. One could also use a WDM filter which would guarantee compatibility with existing WDM fibre networks [71]. Another approach is to use a cavity-assisted process where the down-conversion bandwidth spans multiple cavity resonances, this has been used to demonstrate frequency-bin entanglement on-chip with microresonator sources [60, 64, 65]. The main drawback of both of these approaches is the loss, either from filtering a broadband source or resonant losses inside the cavity which will limit the brightness and heralding efficiency of the source. By using domain engineering the efficiency is not limited by these factors.

Following the steps of Section 3.2 a target PMF can be defined as

$$\begin{aligned}\phi\left(\Delta k;\Delta k_0,\delta,\sigma,n\right)=\sum_{j}^{n}&\exp\left(-\frac{\sigma^2\left(\Delta k-\Delta k_0-\left(j+\frac{1}{2}\right)\delta\right)^2}{2}\right)\\&+\exp\left(-\frac{\sigma^2\left(\Delta k-\Delta k_0+\left(j+\frac{1}{2}\right)\delta\right)^2}{2}\right),\end{aligned}\tag{3.12}$$

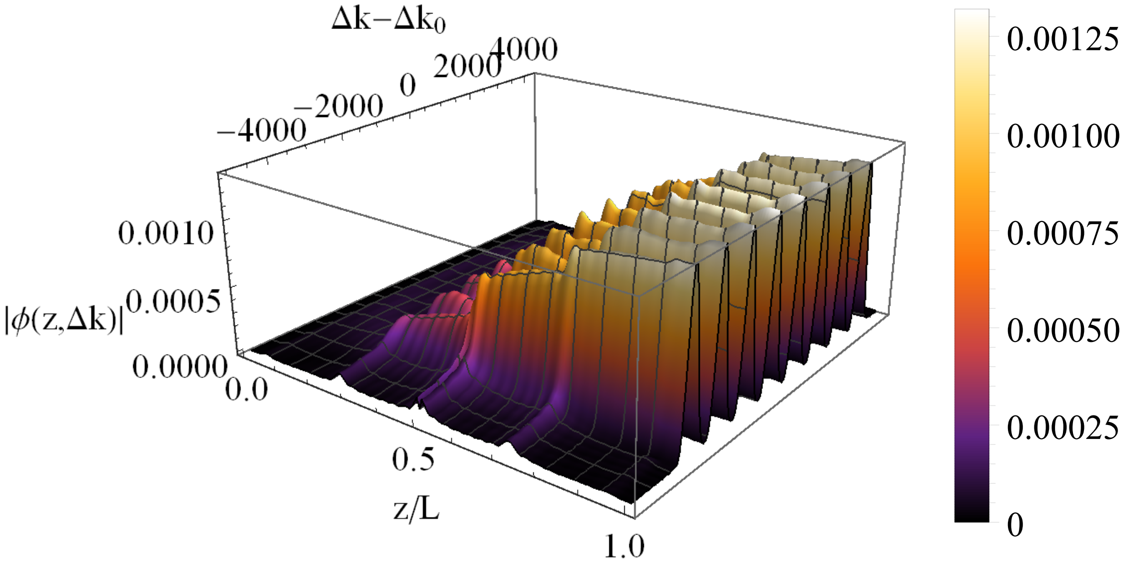

Figure 3.6: The absolute value of the PMF for the case of eight frequency-bins including normalisation to respect the maximum gradient available with periodic poling. This plot uses the parameters for the crystal design used in the rest of this chapter.

with the bin spacing $\delta$, the width of each Gaussian set by $\sigma$, the phase mismatch of the central frequencies $\Delta k_0$ and the number of bins equal to $2n$.

Setting $n = 4$ and carrying out the Fourier transform with respect to the phase mismatch $\Delta k$ the nonlinearity profile is then

$$g\left(z;\Delta k_0,\delta,\sigma\right) = \frac{2}{\sigma}\exp\left(i\Delta k_0 z - \frac{z^2}{2\sigma^2}\right)\sum_{n=0}^{5}\cos\left((2n+1)\frac{\delta}{2}z\right). \tag{3.13}$$

The next step is calculating how the amplitude grows along the crystal by integrating Eq. (3.13) with respect to $z$. This is quite painful for the case of eight bins but is not beyond the capabilities of Mathematica or your computer algebra system of choice. The resulting PMF is shown in Fig. 3.6.

The number of bins $n$, width of the bins $\sigma$ and bin spacing $\delta$ must be set such that the nonlinearity profile approaches zero at the crystal edges. If there is a non-zero nonlinearity profile at the crystal edge the sharp discontinuity generates lobes in the PMF similar to the sinc-shape seen with bulk and periodically poled crystals.

The width of each bin was chosen to generate an approximately separable Gaussian bin with the 1.3 ps pulse-duration of the Ti:Sapphire laser available. From previous work on pure Gaussian photons a sensible choice for the width is $\sigma = L/4.5$, where $L$ is the crystal length. This then sets the width of a single bin in frequency to be approximately 300 GHz FWHM.

For the bins to be individually resolved the spacing $\delta$ must then be much larger than $\sigma$ such that the PMF is close to zero between peaks. Another factor to remember is that the International Telecommunication Union standard wavelength-division multiplexing grid has a 100 GHz spacing, so ideally the peaks would be integer multiples of 100 GHz for potential integration in a fibre network. The $\delta$ parameter was tuned to set the spacing to be 500 GHz by simulating the JSA and fitting to the signal and idler marginal spectra.

The number of peaks was set to eight in order for the full spectrum to fit inside the window available with the time of flight spectrometer which is around 31 nm, see Section 3.5.1.1.

With the design parameters fixed the position of the domain walls, the point at which the nonliearity profile changes sign, was shared with *Raicol Ltd* who then manufactured the crystal. The JSA, nonlinearity profile and poling design for the designed crystal are presented in Fig. 3.7, Fig. 3.8 and Fig. 3.9 respectively.

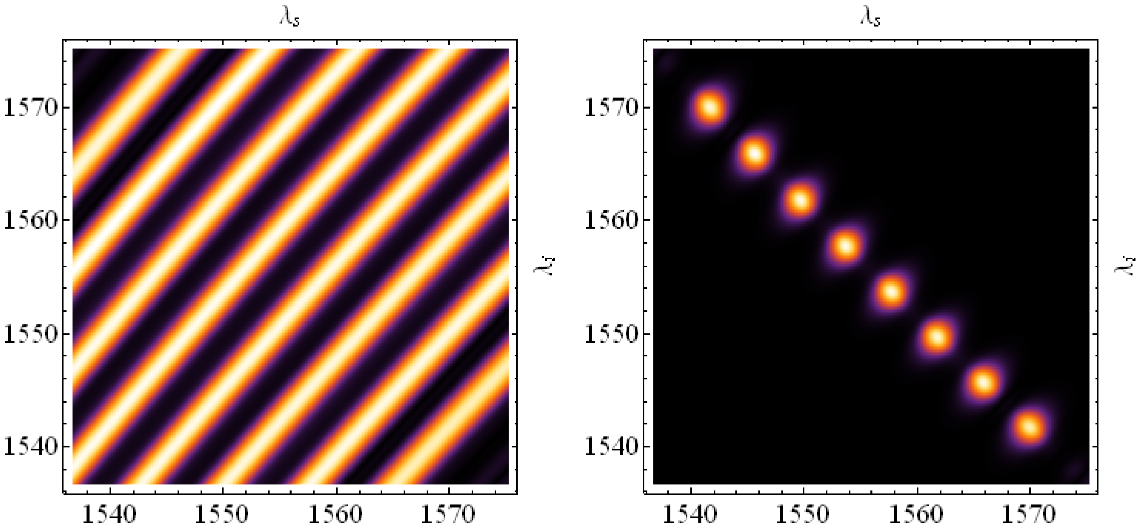

Figure 3.7: Simulated PMF and JSA for the crystal parameters stated and the Sech pulse with 1.3 ps duration. The Schmidt number for this joint spectrum is $K = 8.07$.

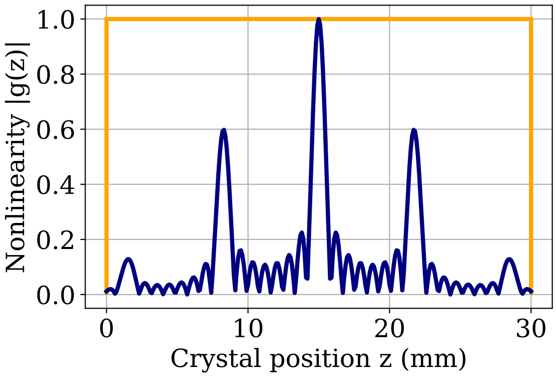

Figure 3.8: Theoretical nonlinearity profile of the 8b-KTP crystal used in this experiment (navy), a periodically poled crystal is shown (orange) for comparison. The crystal length is 30 mm which matches the crystal used. The nonlinearity of the crystal is substantially reduced compared to periodically poled crystal which reduces the overall brightness.

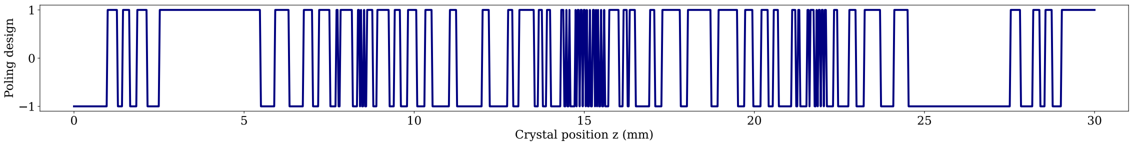

Figure 3.9: The poling design for the 8b-KTP crystal. Plus one and negative one represent the orientation or sign of the ferroelectric domains.

### 3.5.1 Experimental characterisation

Characterising entanglement in the time-frequency degree of freedom is arguably more difficult than other photonic DoFs. The standard route of taking a tomographically complete set of measurements and reconstructing the density matrix of the two-photon state is not easily done in the frequency domain as changing the frequency of a photon requires electro-optics or nonlinear optical effects. Despite these experimental hurdles there has been tremendous progress in measuring the complex spectral amplitude of single photons and photon pairs using electro-optic shearing [72, 73], borrowing ideas from the SPIDER technique for ultrafast pulse characterisation [74]. Process tomography of the quantum pulse gate has been carried out [75], this could be inverted to use the quantum pulse gate to carry out tomography of an unknown frequency encoded state. More recently, complete frequency-bin tomography has been carried out using electro-optics [65]. All of these techniques have considerable experimental overhead. We verify the eight-mode entanglement using a comparatively simpler combination of JSI measurements using time-of-flight measurements and probe the joint spectral phase by measuring biphoton and heralded Hong-Ou-Mandel interference. These sets of measurements are not tomographically complete for the joint spectrum, but under reasonable assumptions of starting from a pure biphoton state which is well established with PDC, agree well with the designed JSA.

Throughout all of the measurements the crystal is pumped by a Ti:Sapphire laser with a pulse duration of 1.3 ps, repitition rate of 80 MHz and a central wavelength of 777.85 nm. The 8b-KTP crystal is temperature tuned to degeneracy at 48.5 °C. The crystal is mounted in a Sagnac interferometer and pumped in one direction for all measurements except for the polarisation entanglement measurements presented in Section 3.5.2 where the Sagnac is pumped bidirectionally [76]. The pump is focussed into the crystal with a 40 cm focal length lens which gives a pump beam waist inside the crystal of $\approx 77\mu$m. The signal and idler photons are collected with 13 mm focal length aspheric lenses (Thorlabs) and the distance from the fibre couplers is optimised to maximise heralding efficiency. Silicon filters (Semrock) and long-pass interference filters (Thorlabs) at 1400 nm are used to isolate the single photons from residual pump light.

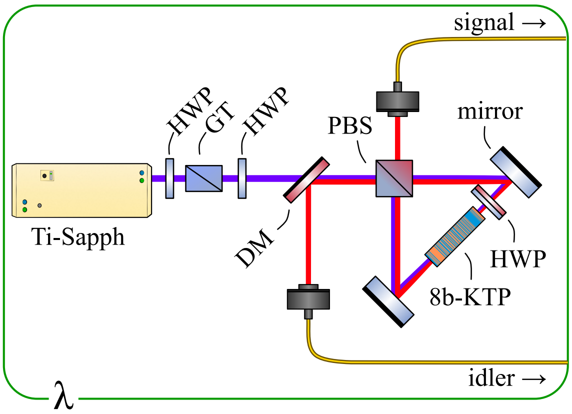

Figure 3.10: An 80 MHz, 1.3 ps Ti-Sapphire laser is sent through a half waveplate (Crylight) (HWP) and Glan-Taylor polariser (Thorlabs) (GT) for intensity and polarization control. The 8b-KTP is embedded in a Sagnac interferometer which allows the generation of polarisation entanglement. Down-converted photon pairs (signal and idler) are separated by a polarising beam splitter (PBS) (Foctek) then coupled into single mode fibres and sent to characterisation stages.

The measured brightness of the source is 450 coincidences/mW with a Klyshko efficiency defined as $\eta = cc/\sqrt{s_1 s_2} = 48\%$ (corrected to 60% by backing out the detector quantum efficiency of 80%). The difference in brightness is expected from the reduced nonlinearity, see Fig. 3.8. In similar experimental conditions a periodically poled crystal has a brightness of 4900 coincidences/mW. By comparing the nonlinearity profiles we expect a brightness of around 13% of a periodically poled crystal. There are likely some experimental factors which further reduce the measured brightness such as chromatic aberration in the collection optics across the 30 nm bandwidth of the downconverted photons compared to narrowband spectrum from the Gaussian crystal. These heralding efficiencies could likely be improved, Klyshko efficiencies greater than 60% have been demonstrated in similar setups with Gaussian crystals. When using Gaussian crystals additional 10 nm band-pass filters are used to reject uncorrelated single photons which reduce the ratio of photon pairs detected compared to signal and idler singles rate. Using larger band-pass filters of around 30 nm could be used to help lower the singles rate for the 8b-KTP crystal and boost the heralding efficiency.

#### 3.5.1.1 Joint Spectral Intensity Measurements

The JSI is measured using long single-mode fibres to map the frequency of the photons to arrival time at the detectors [77] as a time-of-flight spectrometer. Fast coincidence counting logic which is commonly used for multiphoton experiments is then used to record the arrival time of photons referenced to a clock signal derived from the Ti:Sapphire laser. The coincidence counts are then put into a two-dimensional histogram to reconstruct the JSI. For SMF-28 fibre shorter wavelengths travel faster than longer wavelengths (normal dispersion). Around 1550 nm the dispersion of SMF-28 is $\approx 20$ ps/nm/km. We use two 20 km spools of fibre in the TOFS, with the laser repetition rate of 12.5 ns we can look at photons that are ≈31 nm broad before the longest wavelength of the preceding clock cycle overlaps with the shortest wavelength of the current pulse. The size of this spectral window can be altered by pulse-picking the repetition rate to give longer times between pulses or using shorter lengths of fibre which reduces the resolution of the spectrometer. The design choices of the crystal were chosen with this spectral window in mind.

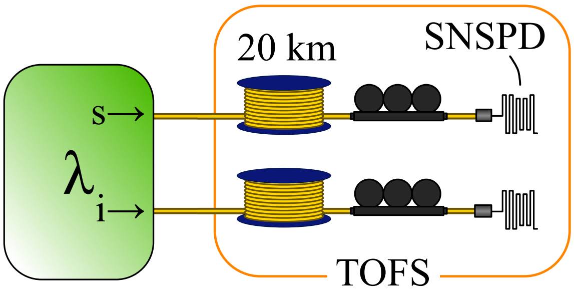

Figure 3.11: Signal and idler pairs from the source are sent to 20 km spools of single-mode fibre before being detected using SNSPDs. The green shaded region represents the source shown in Fig. 3.10. The polarisation is optimised at the detectors using in-fibre polarisation controllers to maximise the singles rate.

The time-tags are recorded using a *Hydraharp 400* time-tagger which has a binning resolution of 1 ps. This then limits the spectral resolution to 2.5 pm. Typically this resolution far exceeds what is needed for a JSI reconstruction, the timing-jitter of the superconducting detectors is on the order of 50 ps. For the JSI reconstruct the data is down-sampled into larger bins to reduce the sparsity of the data.

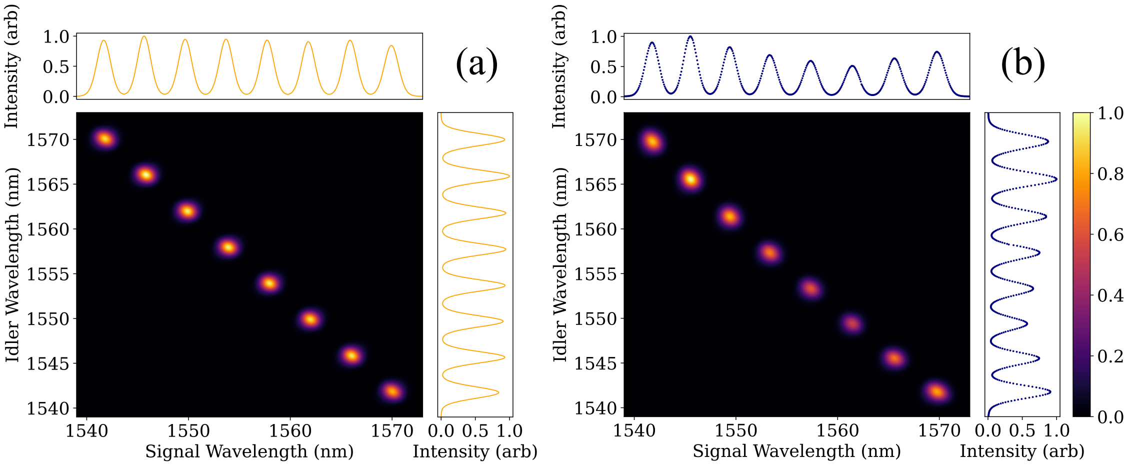

Figure 3.12: Theoretical (a) and experimentally measured (b) joint spectral intensity. The JSI is reconstructed through TOFS on a 500 × 500 grid with each pixel corresponding to an arrival window of 25 ps, which corresponds to a spectral resolution of around 0.06 nm. The spectral range of the spectrometer is set by the temporal separation between pulses from the pump laser corresponding to 12.5 ns, which is wide enough to contain all eight frequency-bins. The marginal distributions are shown on the left and top of the main JSI plot, with counts normalised to the maximum peak height.

The JSI is recorded over four hours of integration with the source pumped at 100 mW for a total number of $4.3 \times 10^7$ coincidence counts. The internal photodiode signal from the Ti:Sapphire is used as a reference clock signal sent to the time-tagger. This dramatically reduces the time needed for the reconstruction compared to previous experiments which used a second PDC source sent directly to a detector and required three-fold coincidence counting [56, 68].

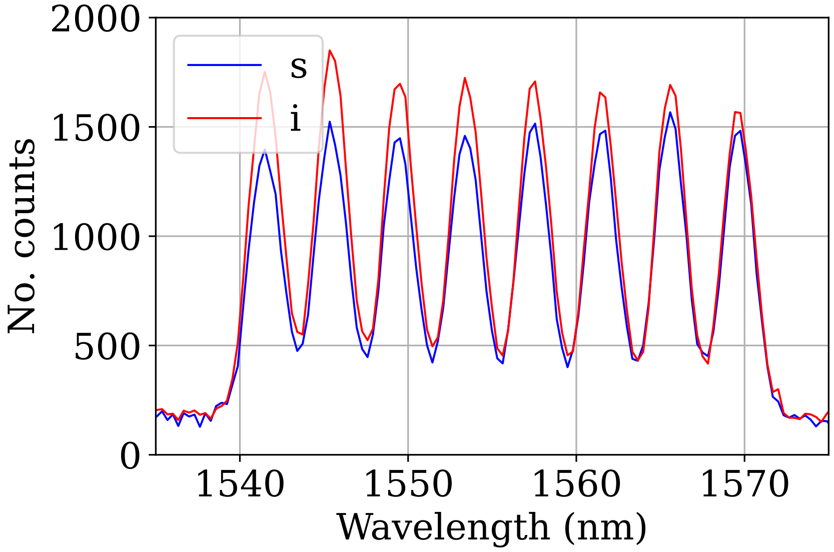

Figure 3.13: The signal and idler spectra measured on a commerical InGaAs EMCCD spectrometer under degenerate conditions for 60 seconds of integration time. These measurements are used to calibrate the time-to-frequency mapping of the TOFS by overlapping the marginal spectra of signal and idler from the JSI to the EMCCD measurements.

The average separation between peaks from these marginal measurements is measured to be 498 GHz which matches well with the designed separation of 500 GHz.

The Schmidt number estimated using the $\sqrt{\text{JSI}}$ is $K = 7.018(3)$. The overlap to an eight-mode maximally entangled state by comparing Schmidt numbers to the ideal value of $\lambda_i = 1/\sqrt{8}$ for the first eight modes and zero otherwise is 96.01(1)%. Errors are quoted at three sigma estimated from 1000 rounds of Monte Carlo simulation assuming Poissonian counting statistics. The Schmidt number and overlap from the theoretical JSA are 8.07 and 98.5% respectively.

The difference between the theoretical and experimental Schmidt values is due to the unequal peak heights and finite suppression between each peak, most clearly seen in the marginals of Fig. 3.12. The finite suppression is a result of the relatively dense packing of the frequency-bins. Reducing the number of bins, for example four bins over the same bandwidth, would improve the extinction ratio. The unequal peak heights are suspected to be an artifact of measuring the JSI using a dispersive fibre spectrometer. As the joint spectrum is relatively broad, around 30 nm, each

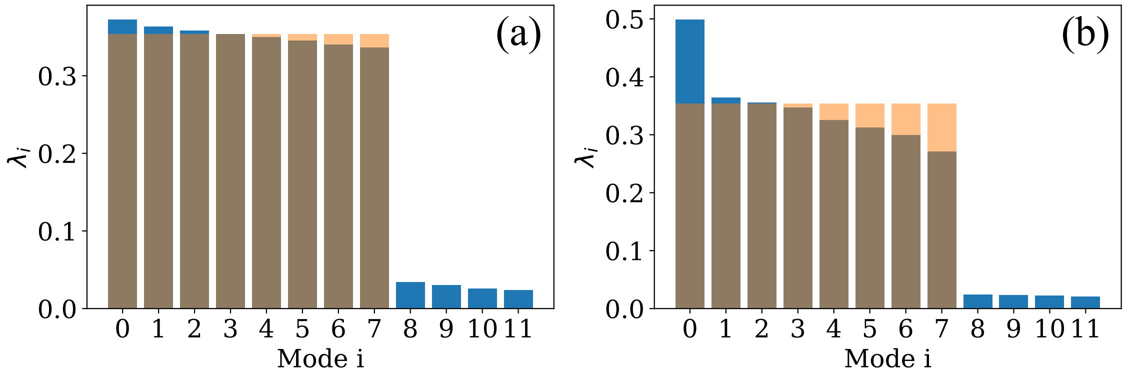

Figure 3.14: Comparison of the Schmidt coefficients for the theoretical JSA (a) and for the experimentally measured $\sqrt{\text{JSI}} = |\text{JSA}|$ (b). The ideal eight-mode entangled state with equal Schmidt coefficients is shown in orange.

bin experiences a slightly different birefringence over the 20 km of single-mode fibre and fibre polarisation controllers used in the reconstruction. This then gives a small variation in the detection efficiency for each bin at the SNSPDs which are polarisation sensitive. This could be mitigated by using spools of polarisation-maintaining fibre for the time-of-flight measurements. Looking at the marginal spectrum measured using a commercial InGaAs CCD which avoids this issue the peak height is much more consistent across the entire spectrum Fig. 3.13.

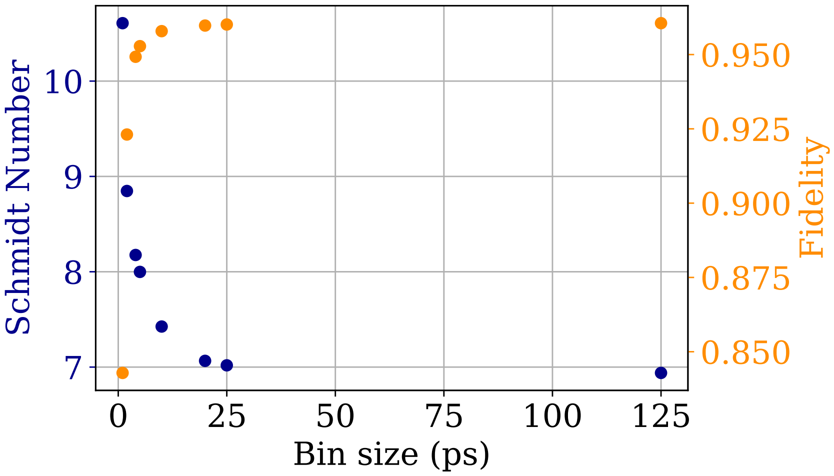

Figure 3.15: Variation in the Schmidt number and fidelity to an eight-mode entangled state with the bin size. For small binning factors the sparsity of the JSI results in an overestimation of the Schmidt number and understimation of the fidelity. For the result presented in this chapter we use a bin size of 25 ps, increasing the binning factor further reduces the extinction ratio between peaks in the JSI as the peaks become less well resolved.

#### 3.5.1.2 Biphoton inteference

As the JSI has no joint spectral phase information this must be assessed through other means. The signal-idler HOMI, which we term biphoton interference, can give some insight into possible spectral phase correlations in the JSA. For frequency-bin entangled states biphoton interference shows characteristic beating between the different frequency components of the JSA [78]. An important point to note is that HOMI reveals the exchange symmetry of the biphoton state under exchange of signal and idler [79]. The essence of this is that a state with perfect symmetric exchange symmetry will show a dip with unit visibility in HOMI, a perfectly antisymmetric state will show a peak with unit visibility [68]. A corollary of this is that a coincidence probability which exceeds 1/2 must come from a state which has antisymmetric exchange symmetry and is therefore a witness of entanglement. It is worth noting that the dimensionality of the entanglement cannot be probed using biphoton HOMI [80]. With the flat spectral phase in the PMF design we expect the biphoton state to be symmetric under exchange of signal and idler and therefore show a high visibility dip at zero time delay.

The biphoton HOMI dip shape as a function of time delay $\tau$ can be calculated from the JSA as

$$p_2\left(\tau\right) = \frac{1}{2} - \frac{1}{2}\int \mathrm{d}\omega_i \int \mathrm{d}\omega_s f^*\left(\omega_i, \omega_s\right) f\left(\omega_s, \omega_i\right) e^{i(\omega_i - \omega_s)\tau}. \tag{3.14}$$

To make the analytic calculation simpler we approximate the JSA as a product of a Gaussian PEF

$$\alpha\left(\omega_s + \omega_i\right) = e^{-\dfrac{\left(\omega_s + \omega_i\right)^2}{2\sigma^2}}, \tag{3.15}$$

and a PMF as a sum of $n$ different Gaussians functions with spacing $\delta$,

$$\begin{aligned}\phi\left(\omega_i,\omega_s\right) = &\sqrt{\frac{1}{\pi\sigma^2\left(n+1\right)}}\\ &\times\sum_{j=0}^{n}\left\{e^{-\frac{\left(\omega_i-\omega_s+\delta\left(j+1/2\right)\right)^2}{2\sigma^2}}+e^{-\frac{\left(\omega_i-\omega_s-\delta\left(j+1/2\right)\right)^2}{2\sigma^2}}\right\},\end{aligned} \tag{3.16}$$

where the number of bins is given by $2\left(n+1\right)$. The width parameter of the PEF and PMF $\sigma$ is assumed to be identical which simplifies the calculation, this is justified by the PMF design. Each bin width is set to match the parameters used for almost completely separable PDC sources [56].

Inserting these into Eq. (3.14) and assuming the overlap between the Gaussians is small the order of integration and summation can be swapped, the biphoton dip shape is given by,

$$p_2\left(\tau\right)=\frac{1}{2}-\frac{1}{2\left(n+1\right)}\sum_{j=0}^{n}e^{-\frac{\left(\delta+2j\delta\right)^2+\sigma^4\tau^2}{4\sigma^2}}\left(1+e^{\frac{\left(\delta+2j\delta\right)^2}{4\sigma^2}}\cos\left(\frac{\delta\tau}{2}+j\delta\tau\right)\right). \tag{3.17}$$

For the biphoton interference measurements the repitition rate of the Ti:Sapphire laser is temporally multiplexed up to 160 MHz from 80 MHz using a free space delay line [81]. For the same average power the 160 MHz pulse train reduces the higher order emission from the PDC source while keeping the single pair emission constant. For a repetition rate $R = 80$ MHz and pulse power $P$ the pair emission goes roughly as $p_{\text{pair}} \propto RP$ and the leading higher-order emission go as $p_{\text{higher}} \propto RP^2$. The effect of doubling the repetition rate is to send $P \rightarrow P/2$ and $R \rightarrow 2R$ such that $p_{\text{pair}}$ is constant but the higher order emission goes to $p_{\text{higher}} \rightarrow 2R\left(P/2\right)^2 = PR/2$. As the biphoton state is separable in all other degrees of freedom other than frequency we can attribute the anti-bunching peaks at ±1 ps to spectral entanglement, see Fig. 3.16.

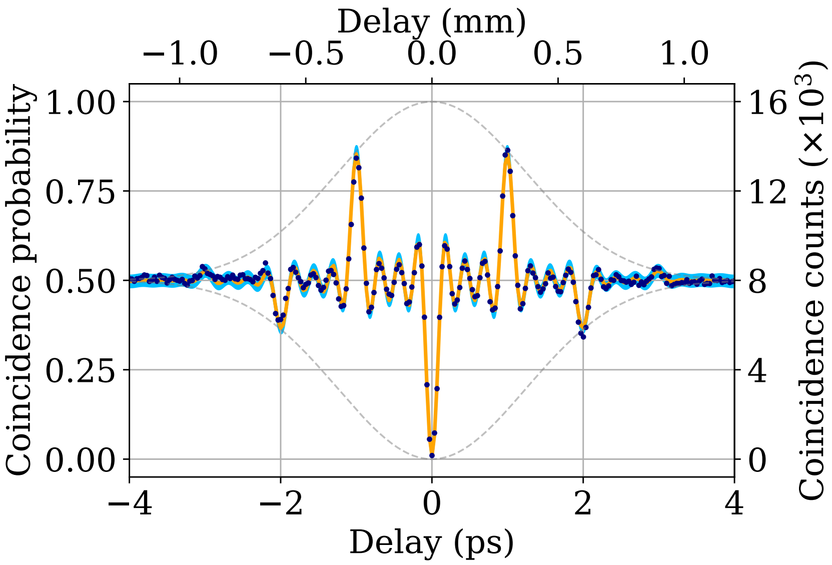

Figure 3.16: Biphoton HOM interference data (blue dots) with line of best fit (orange) with Eq. (3.17) with n = 3. Bin width, bin separation and visibility are free parameters. Coincidence counts are integrated over two seconds with an incident pump power of 400 mW. Counts are recorded every 0.1 mm using a motorised translation stage. The measured visibility is 97.9(3)%. The frequency-bin separation $\delta$ extracted from the best fit parameters is found to be 499.7(3) GHz which agrees with the designed spacing of 500 GHz. The shaded blue region is the three sigma confidence region assuming Poissonian counting statistics. The grey dashed line shows the Gaussian envelope expected from a single frequency bin which bounds the visibility of the frequency beating.

#### 3.5.1.3 Heralded two-photon interference

From earlier discussions of the Schmidt decomposition, the purity of a heralded single photon is related to the Schmidt number as $P = 1/K$, see Eq. (2.32). The single photon purity is also equal to the visibility in a HOMI measurement. Measuring the visibility in a heralded HOMI (signal-signal or idler-idler) experiment then gives some information about the spectral entanglement of the source.

With one crystal, the heralded HOMI is measured by delaying a signal photon to interfere with a signal photon produced at a later time using an unbalanced Mach-Zehnder interferometer (MZI). The idler photons are probabilistically split on a 50:50 beam splitter and sent to two SNSPDs to herald successive events. The delay in the MZI is set to three clock cycles, this was chosen for experimental convenience as fibre patch cables of $\approx 7.5$m are readily available. For the heralded HOMI measurements the pump beam was not temporally multiplexed and the base repetition rate of 80 MHz was used. Using similar arguments as the biphoton case the four-fold detection in the heralded HOMI goes as $P_{2\text{ pair}} \propto RP^2$ so reducing the pulse power but increasing the repetition rate does not increase the four-fold rate for a fixed pump power. A secondary issue is that if the delay line does not match exactly half the repetition rate the delay between photons generated by different pulses varies which will degrade the HOMI visibility.

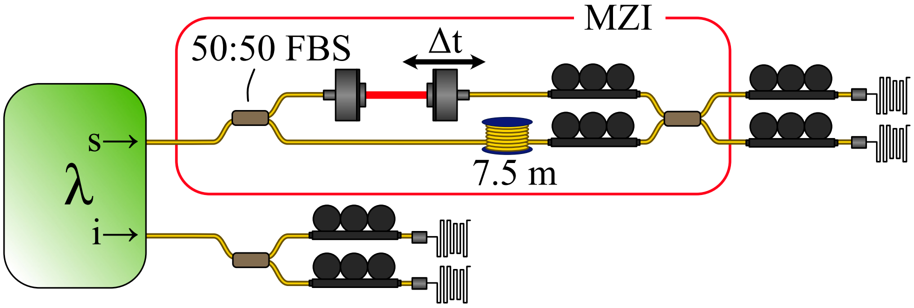

Figure 3.17: Heralded two-photon Hong-Ou-Mandel interferometer. The signal photon is sent through a 50:50 fibre beam splitter (FBS) which probabilistically directs each photon into an unbalanced Mach-Zehnder interferometer (MZI). One MZI path contains a ∼7.5 m fibre which introduces a temporal delay corresponding to three laser clock cycles. The second MZI path contains an adjustable free-space delay, $\Delta t$. Two signal photons passing through the MZI then interfere on a second 50:50 FBS before detection with SNSPDs. The idler mode is sent to a 50:50 FBS then detected with SNSPDs to herald successive probabilistic emissions from the source. Coincidence counts are recorded for successful four-fold events.

The version of the heralded HOMI using delayed pulses has some disadvantages to the case of using two independent crystals and interfering photons generated from the same clock pulse. With the probabilistic routing of photons on a 50/50 beam splitter and the electronic delays programmed into the timing logic the number of valid four-folds is 1/8 of the events where photons are generated in adjacent pulses. This comes from two factors of 1/2 on the heralded arm, the early idler must go to one of the detectors which has a 30 ns electronic delay and the second idler must reach the other detector. Similarly there are two factors of 1/2 for the signal photons, the early pulse must go down the longer path in order to temporally overlap the photons on the beam splitter where the interference takes place. This leads to the relatively low four-fold rate of around 0.3 Hz.[1]

---

[1] When someone asks “Do you think we should buy two crystals?” the answer is “Yes” and definitely not “I’m not sure we would need a second one...”.

The heralded HOMI dip can be calculated as

$$p_4(\tau) = \frac{1}{2} - \frac{1}{2}\int d\omega_{i1}\int d\omega_{s1}\int d\omega_{i2}\int d\omega_{s2} f^*(\omega_{i1},\omega_{s2})\, f^*(\omega_{i2},\omega_{s1})\, f(\omega_{i1},\omega_{s1})\, f(\omega_{i2},\omega_{s2})\, e^{i(\omega_{s1}-\omega_{s2})\tau}. \tag{3.18}$$

With the same assumptions used for the biphoton dip swapping the order of summation and integration and evaluating the integral over signal and idler frequencies gives the coincidence probability as,

$$\begin{aligned} p_4(\tau) &= \frac{1}{2} - \frac{1}{4(n+1)^2} \\ &\times \sum_{j=0}^{n} e^{-\frac{(\delta+2j\delta)^2+\sigma^4\tau^2}{4\sigma^2}} \left(1 + e^{\frac{(\delta+2j\delta)^2}{4\sigma^2}} + 2\cos\left(\frac{1}{4}(\delta+2j\delta)\tau\right)\right). \end{aligned} \tag{3.19}$$

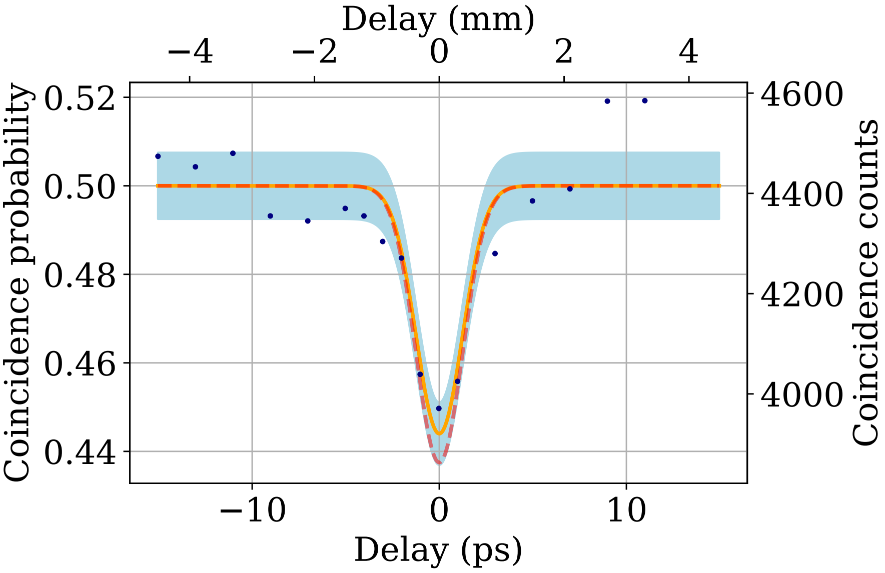

Figure 3.18: Heralded two photon interference data. Coincidence counts are integrated over 4 hours per data point with a step size of 0.5 mm. The incident pump power was set to 400 mW and the parameters $\delta$ and $\sigma$ are set to match the biphoton interference measurements. The orange line is the line of best fit, the light blue region is the one sigma confidence interval assuming Poissonian counting statistics. The measured visibility is 11.2(1.4)% which agrees with the expected value of 12.5% (red dashed line, Eq. (3.19)) for an eight-mode entangled state within experimental error.

The HOMI measured in the Fig. 3.18 shows reasonable agreement with the theoretical result based on Eq. (3.19). The small discrepancy between the theoretical visibility and the experimental data is attributed to small variations in the polarisation state across the full bandwidth of the signal photons induced by chromatic dispersion in the fibre polarisation controllers.

### 3.5.2 Polarisation frequency-bin hyperentanglement

Having demonstrated frequency-bin entanglement through a combination of JSI and HOMI measurements the source is pumped bidirectionally in the Sagnac interferometer to generate hyperentanglement in both frequency-bin and polarisation. Hyperentanglement between pulse-mode and polarisation has been demonstrated with domain engineered crystals in a Saganc interferometer [82].

Hyperentanglement between frequency and polarisation has been used in a demonstration of entanglement based QKD in a WDM network [71, 83]. Typically these sources are CW pumped, spectrally correlated type-0 sources. This frequency correlation is used indirectly, the strong correlation ensures that when a user detects a signal photon in a channel which is red detuned from half the pump frequency the idler photon will be detected in a channel blue detuned by the same amount. Typical sources in this type of experiment have a signal/idler bandwidth of $\sim$60 nm and the photons are collected in channels which cover $< 10$ nm [83]. Photons emitted into the remaining bandwidth are lost which reduces the overall efficiency and brightness of the source. A frequency-bin entangled source could be used in this type of demonstration with high efficiency and using the entire bandwidth of the downconverted photons.

We show that the polarisation entanglement persists across all eight bins by using TOFS after polarisation tomography, see Fig. 3.19. The TOFS measurement mimics the action of a WDM by temporally demultiplexing the frequency components into different arrival times compared to a typical WDM which maps frequency to spatial mode.

The state produced after the Sagnac interferometer can be written as,

$$|\psi\rangle = \sum_{\substack{i=-4\\ i\neq 0}}^{4} \frac{1}{\sqrt{2}} \left(|H\rangle |V\rangle - e^{i\phi_i} |V\rangle |H\rangle\right) \otimes \frac{1}{\sqrt{\mathcal{N}_i}} |i\rangle |-i\rangle , \tag{3.20}$$

where $\mathcal{N}_i$ is related to the intensity of each frequency bin. The phase $\phi_i$ varies between bins due to the chromatic dispersion of the polarisation optics inside the Sagnac interferometer and the waveplates used in the polarisation tomography setup.

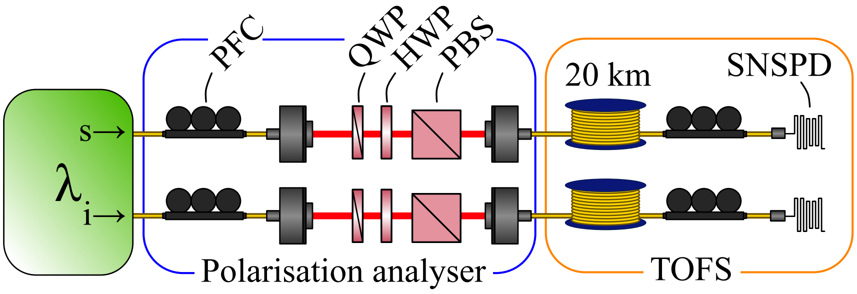

Figure 3.19: Experimental setup for polarisation-resolved TOFS. Polarisation tomography is carried out with a typical quarter-wave plate, half-wave plate and polarising beam splitter. The TOFS is identical to that of Fig. 3.11.

We carry out polarisation tomography using symmetric informationally complete (SIC) projections to limit the number of joint spectra required to 16 compared to 36 required if measuring mutually unbiased bases (MUB). The set of SIC states are the minimum set of states required for complete tomography with each state in the set having equal overlap with any other state in the set. For a single qubit the SIC states can be visualised as a tetrahedron on the Bloch sphere. Each projection contains on average $20 \times 10^6$ detection events, recorded over two hours of measurement.

The SIC states used are given by [84],

$$\begin{aligned} M_1 &= \frac{1}{2}\left(\mathbb{I} + \frac{\sigma_x + \sigma_y + \sigma_z}{\sqrt{3}}\right) \\ M_2 &= \frac{1}{2}\left(\mathbb{I} + \frac{\sigma_x - \sigma_y - \sigma_z}{\sqrt{3}}\right) \\ M_3 &= \frac{1}{2}\left(\mathbb{I} + \frac{-\sigma_x + \sigma_y - \sigma_z}{\sqrt{3}}\right) \\ M_4 &= \frac{1}{2}\left(\mathbb{I} + \frac{-\sigma_x - \sigma_y + \sigma_z}{\sqrt{3}}\right), \end{aligned} \tag{3.21}$$

where $\mathbb{I}$ is the identity matrix and $\{\sigma_x, \sigma_y, \sigma_z\}$ are the Pauli matrices. These states can be pictured as the vertices of a tetrahedron in the Bloch sphere. The waveplate settings for the SIC measurements are given by,

$$\begin{aligned} M_1 &= \{20.066°, 22.5°\} \\ M_2 &= \{42.566°, -22.5°\} \\ M_3 &= \{-42.566°, 22.5°\} \\ M_4 &= \{-20.066°, -22.5°\}\,. \end{aligned} \tag{3.22}$$

for the HWP and QWP respectively.

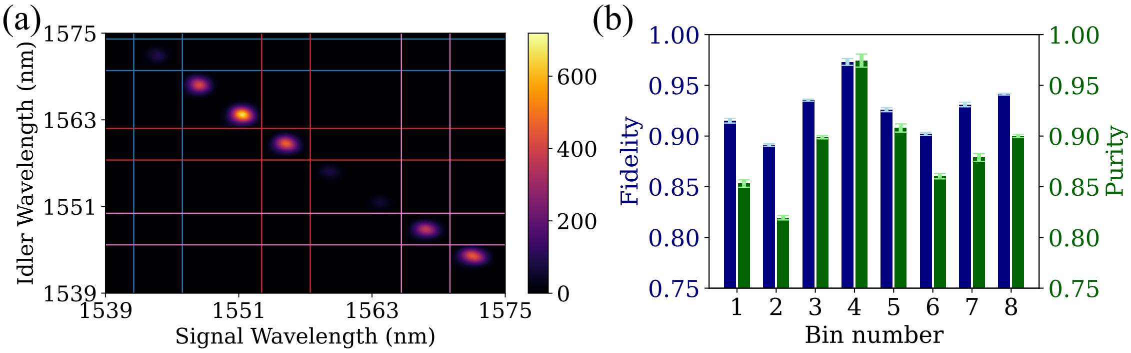

Figure 3.20: (a) Experimental JSI for polarisation projection $M_1$ on both qubits. The signal and idler filtering applied in post-processing is shown for bins 1 (blue), 4 (red) and 7 (pink). The bin width is 1.52 ns which corresponds to 3.8 nm filter width given the fibre dispersion of around 20 ps/(nm·km) and 20 km of fiber. (b) Results of polarisation tomography with frequency resolved measurements. The average purity and fidelity are 88.7(3)% and 92.6(1)% respectively. Error bars are calculated by 1000 rounds of Monte Carlo sampling assuming Poissonian counting statistics.

The fidelity to the singlet state is calculated by applying a correction for the phases $\phi_i$ in post-processing. In a wavelength-division multiplexed scenario this phase can be corrected by appropriate waveplate settings. The average purity and fidelity are 88.7(3)% and 92.6(1)% respectively with a maximum (minimum) fidelity of 97.3% (88.7%). The drop in purities compared to other telecom wavelength Sagnac sources [85] is attributed to the wavelength dependence of the polarisation optics inside the Sagnac interferometer and can be improved by using an achromatic half-wave plate inside the Sagnac. The waveplates in the tomography setup also impart different unitaries across the full bandwidth of the downconverted photons which reduces the purity of the reconstructed state. This can be mitigated by reconstructing the polarisation state of each bin individually using WDM filters [86] or again using achromatic optics.

## 3.6 A hint towards frequency-bin GHZ states

Frequency-bin encoded photonics has focused primarily on entanglement of two photons with dimension varying from $d = 8$ in this work up to as much as $d = 648$ [70] but restricted to only two photons. Even the demonstration of time-frequency encoded cluster states has used modal entanglement of two particles [60], using time-bins and frequency-bins as independent degrees of freedom. This reluctance to go beyond two photons likely comes from the loss associated with manipulating frequency encoded states or typical CW excitation which makes multiphoton experiments difficult.

Entanglement of more than two particles is a complex topic which I will not discuss in detail here but a particularly relevant state for quantum information tasks is the Greenberger-Horne-Zeilinger (GHZ) state [87, 88] which has the form,

$$|\mathrm{GHZ}\rangle = \frac{1}{\sqrt{d}} \sum_{i=0}^{d-1} |i\rangle^{\otimes N} \tag{3.23}$$

for $N$ $d$-dimensional qudits.

Inspired by ideas of generating polarisation GHZ states in a post-selected fashion using a polarising beam splitter I present a scheme for generating a four-photon, three frequency-bin GHZ state in a post-selected manner. This scheme uses a particular type of frequency-bin entangled state which could be generated using type-2 KTP at telecom wavelegnths with PEF shaping, the complement of PMF shaping with domain engineering presented in this chapter. PEF shaping can be easily achieved using Fourier transform pulse shapers on ultrafast pulses.

Consider the case of a three frequency-bin PEF pumping a PDC process in type-2 KTP at telecom wavelengths with symmetric group-velocity matching. This would produce the biphoton state of the form

$$|\psi\rangle = \frac{1}{\sqrt{3}}\left(|11\rangle + |22\rangle + |33\rangle\right). \tag{3.24}$$

This is similar to the frequency-bin state presented in this chapter but the frequency bins are aligned to the positive diagonal in the JSA not the anti-diagonal as with PMF shaping. Considering the joint state of two copies of such a source we have,

$$\begin{aligned}|\psi\rangle =& \frac{1}{3}\left(|11\rangle + |22\rangle + |33\rangle\right) \otimes \left(|11\rangle + |22\rangle + |33\rangle\right) \\ =& \frac{1}{3}\left(|1111\rangle_{abcd} + |1122\rangle_{abcd} + |1133\rangle_{abcd}\right. \\ &+ |2211\rangle_{abcd} + |2222\rangle_{abcd} + |2233\rangle_{abcd} \\ &\left.+ |3311\rangle_{abcd} + |3322\rangle_{abcd} + |3333\rangle_{abcd}\right),\end{aligned} \tag{3.25}$$

where we the subscripts label the spatial mode, see Fig. 3.21. We now act on this state with a multiport interferometer made up of 2 × 2 elements which reflect one of the three frequencies and transmit the other two. These could be made of either dichroic mirrors or fibre Bragg gratings with optical circulators on the input and output depending on the spacing and bandwidth of the frequency bins.

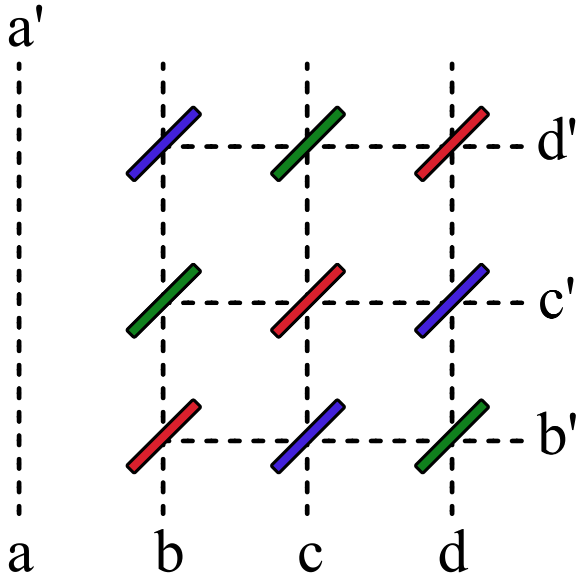

Figure 3.21: Multiport interferometer for generating a frequency-bin GHZ state from two frequency-bin Bell pairs. The colour coding reflects the frequency which is reflected by the mirror, blue for $|3\rangle$, green for $|2\rangle$ and red for $|1\rangle$.

After going through the mulitport the output state can be written as,

$$\begin{aligned} U\left|\psi\right\rangle =& \frac{1}{3}\left(\left|1111\right\rangle_{a'b'c'd'} + \left|1122\right\rangle_{a'b'd'b'} + \left|1133\right\rangle_{a'b'b'c'} \right. \\ & + \left|2211\right\rangle_{a'c'c'd'} + \left|2222\right\rangle_{a'c'd'b'} + \left|2233\right\rangle_{a'c'b'c'} \\ & \left. + \left|3311\right\rangle_{a'd'c'd'} + \left|3322\right\rangle_{a'd'd'c'} + \left|3333\right\rangle_{a'd'b'c'}\right). \end{aligned} \tag{3.26}$$

Post-selecting on a four-fold coincidence between modes $a', b', c', d'$ the final state is,

$$\left|\psi\right\rangle_{\text{post}} = \frac{1}{\sqrt{3}}\left(\left|1111\right\rangle + \left|2222\right\rangle + \left|3333\right\rangle\right), \tag{3.27}$$

which is a GHZ state of three frequency-bins.

For the scheme to be post-selectable the number of frequency bins $d < n$, where $n$ is the number of particles, such that one spatial mode does not take part in the interference. It is not clear if this type of passive frequency mixing generalises to creating GHZ states for other input Bell states such as those produced by PMF where the frequencies are anti-correlated. Despite the restriction on the input state this scheme demonstrates that passive optical fusion of frequency-bin Bell states into larger entangled states is possible.

## 3.7 Future designs for other time-frequency encodings

At this point we return to the ideas presented in Section 3.3 and Fig. 3.3 to discuss other crystal designs which include time-bin encoded states and hybrid encodings. These crystals were not manufactured during the course of this thesis but may form the basis for future work with domain-engineered crystals.

### 3.7.1 Time-bin crystals

As hinted at previously, in order to generate time-bin entanglement the PMF should have some sinusoidal modulation in the frequency domain Eq. (3.8). Following the same design process a crystal which generates time-bin entanglement between signal and idler can be constructed with a PMF of the form,

$$\begin{aligned}\phi\left(\Delta k;\Delta k_0,\tau,\sigma\right)=&\exp\left(-\frac{\left(\Delta k-\Delta k_0\right)^2\sigma^2}{2}\right)\exp\left(i\left(\Delta k-\Delta k_0\right)\tau\right)\\&+\exp\left(-\frac{\left(\Delta k-\Delta k_0\right)^2\sigma^2}{2}\right)\exp\left(-i\left(\Delta k-\Delta k_0\right)\tau\right).\end{aligned} \tag{3.28}$$

Eq. (3.28) is simply a Gaussian function times a cosine modulation. As the nonlinearity profile is the Fourier transform of the PMF and using the property that a phase in one domain gives a linear shift in the Fourier domain the nonlinearity profile is expected to be a pair of Gaussians shifted in position with respect to one another, see Fig. 3.22 (c).

This then illustrates how the time-bin entanglement is generated inside the crystal, as the pump beam propagates it generates photons in one of two well localised positions in the crystal with no photons produced between these positions. This also then is the main hurdle with using domain engineering to produce time-bin entanglement, the separation between the time-bins is on the order of the time it takes the pump and signal/idler to walk away from each other over the crystal length. As an illustrative calculation let us consider an ideal case where the Gaussian functions are infinitely narrow and at either end of the crystal such that they are separated by the full crystal length which we will take to be 30 mm. The time between the pump and signal/idler photon reaching the second nonlinear region after passing through the first is given by,

$$T_s-T_p=\frac{\left(n_{gs}-n_{gp}\right)L}{c}. \tag{3.29}$$

Putting in the group indices for 775 nm and 1555 nm in KTP the separation in time is around 4.4 ps. Sadly this is an upper estimate on the available time separation between the bins, the nonlinear regions cannot be infinitely narrow and placed at the crystal edges. In Fig. 3.22 the PMF, JSA and nonlinearity profile are presented for realistic parameters which has the nonlinear regions separated by 15 mm with therefore 2.2 ps separation. A point worth noting is that for the time bins to be well resolved the pump must be considerably shorter than the 1.3 ps used for the frequency-bin entangled crystal. For the simulated JSA presented in Fig. 3.22 the pump beam has a duration of 300 fs.

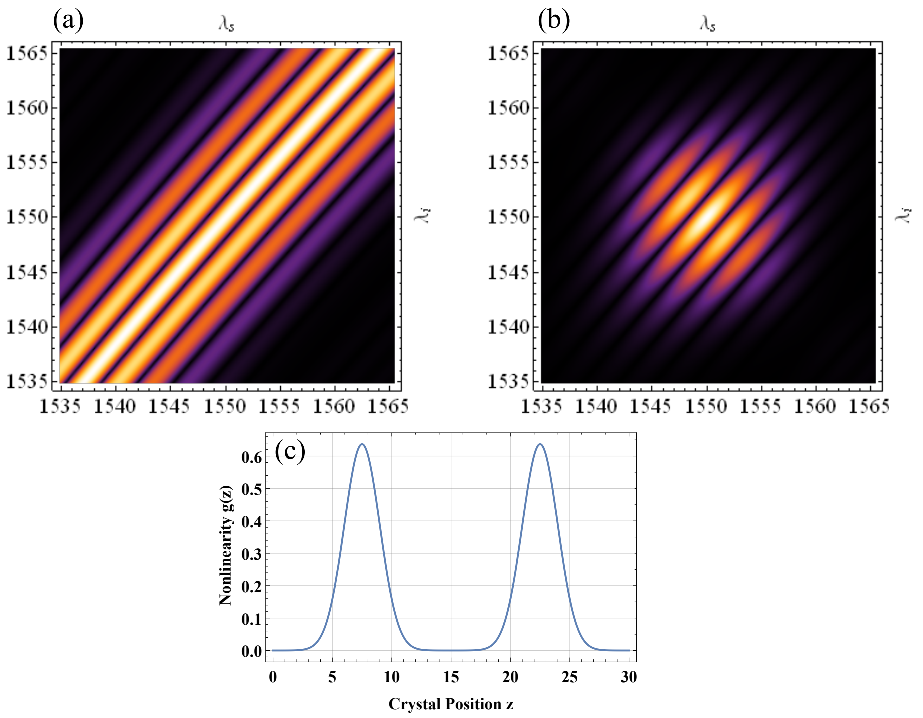

Figure 3.22: Time-bin phasematching function (a) and JSA with the corresponding crystal nonlinearity showing two well separated Gaussian peaks (c). The pump pulse duration is 300 fs which allows the time bins to be well resolved, the Schmidt number for this PDC process is $K = 2.02$ which is indicative of a two-mode maximally entangled state.

This may seem quite bleak, the time-bin separation is certainly experimentally challenging to deal with and outside the reach of standard SNSPDs which have 10s of ps jitter. The separation could be resolved using upconversion detection with ultrafast pulses [89]. Recently a lab demonstration of QKD using ultrafast time-bins with temporal separation of 4.5 ps was demonstrated using cross-Kerr nonlinearities to convert the time-bin qubits to polarisation qubits which were then analysed by standard polarisation tomography. As improvements to crystal fabrication increases and it becomes feasible to grow larger crystal with uniform poling quality the time-bin separation can be increased which will also relax the demanding experimental requirements. A future application of ultrafast time-bin qubits might be in QKD over free-space links with the advantage that the source could be clocked at 10s of GHz.

### 3.7.2 Hybrid encodings

We have shown experimentally how frequency-bins can be generated with domain engineering in this thesis and hinted at how time-bins could be realised in Section 3.7.1. With pulse-mode encoded crystals demonstrated experimentally in previous work [68], all of the methods of encoding in time and frequency have been covered. One possible future area of investigation could be using more than one encoding method in a single crystal in a hybrid-encoding scheme, such as the purple region in Fig. 3.3. Time-bins and frequency-bins have already been used together to form cluster states on chip [60]. So far the possibility of using pulse-modes with another type of encoding has not been explored. For instance consider a PMF combining a combination of pulse-modes and frequency-bins, see Fig. 3.23.

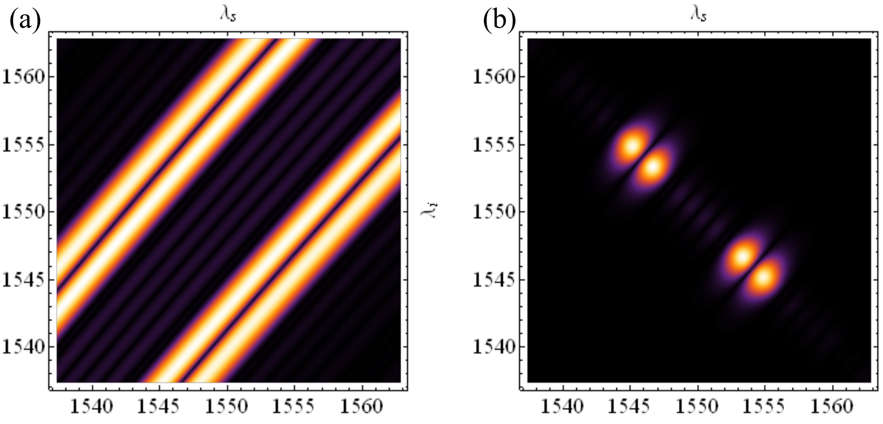

Figure 3.23: PMF (a) for the case of two frequency-bins with each frequency-bin consisting of two pulse-modes and the resulting JSA (b). The Schmidt number is $K = 4.03$, there are some unsuppressed sinc lobes between the two bins which could likely be improved by refining the crystal parameters.

The state produced by the PDC process shown in Fig. 3.23 can be written as

$$|\psi\rangle = \frac{1}{2}\left(|\omega_1\rangle|\omega_2\rangle + |\omega_2\rangle|\omega_1\rangle\right) \otimes \left(|\mathrm{HG0}\rangle|\mathrm{HG1}\rangle - |\mathrm{HG1}\rangle|\mathrm{HG0}\rangle\right), \tag{3.30}$$

which is a hyperentangled state of frequency-bins and pulse-modes where the states $|HG0\rangle, |HG1\rangle$ are the zero and first-order Hermite-Gauss modes. Considering projecting out one of the frequency-bins, say the signal photon at 1554 nm and the idler at 1545 nm, the remaining lobe is left in an entangled state in pulse-modes. An interesting open question is if pulse-modes can be coherently manipulated without disturbing entanglement in the other encodings in a similar manner to time-bin and frequency-bin hyperentangled states. Current methods of coherently operating on pulse-modes use the quantum pulse gate which would not preserve time or frequency-bin entanglement.

# Chapter 4

# Quantum dot frequency conversion

At this point we shift our focus away from tailored PDC sources and turn our attention to frequency conversion and specifically DFG. In this chapter we show results on frequency converting light from a quantum dot single-photon source to the telecom C-band. Many quantum emitters have desirable properties that make them arguably better candidates for single-photon sources than pair sources based on nonlinear processes. There is no inherent trade-off between the brightness of the source and the signal-to-noise ratio. For a PDC source as the probability of producing a single pair of photons increases the signal-to-noise ratio decreases due to higher order pair emission. With a single-emitter this is no such issue, increasing the brightness is *just* a matter of engineering the photonic structure the emitter lives in, and in principle this does not have to increase the background noise.

The main drawback of nearly all single-photon emitters is their emission wavelength, typically this is in the visible or near-infrared range. While these wavelengths might find use in QKD over free-space channels [90], they are incompatible with standard optical fibre which has the lowest loss around 1550 nm. For the remainder of this chapter we will restrict the discussion of single-emitters to quantum dots.

There are two possible solutions for this problem, the first is to change the materials and design of the QD to move the emission wavelength longer towards the telecom windows. There has been dramatic progress in this direction with excellent demonstrations of high purity single-photon emission, demonstrated by second-order coherences on the order of $g^{(2)} = 5 \times 10^{-3}$ [91]. Despite this progress, the performance of these sources still lags behind their counterparts in the NIR in terms of two-photon interference visibility and count rate. At the moment I think it is unclear if this is a fundamental issue or if it is simply a matter of time before the fabrication and control of these devices improves. [1]

The second option is to take the already excellent QD at NIR wavelengths and use frequency conversion to get to 1550 nm. This can in principle be noiseless and have high efficiency. The drawback is the additional experimental complexity in running a frequency conversion setup with an additional laser system in your single-photon source. FC based on three-wave mixing has been demonstrated with NIR quantum dots to the telecom bands has been demonstrated with MHz detected rates at 1550 nm with low multiphoton emission [92, 93]. It has also been used to demonstrate remote two-photon interference between distinct QDs which does not degrade the visibility of the sources before conversion [33, 94].

This chapter highlights the experimental steps required to carry out this frequency conversion process. Specifically the QD source, the driving laser and the lithium niobate waveguide used for DFG will be discussed in turn before the performance of the frequency converted single-photon source is discussed.

## 4.1 Quantum dot

The quantum dot source consists of a self-assembled InGaAs/GaAs QD coupled to an oxide-apertured micropillar cavity with a Q factor of $10^4$. The QDs are embedded in a *p-i-n* diode structure [95, 96] which enables charge control and tuning of the QD emission to the cavity mode via the Stark effect. The sample is kept at a temperature of 4 K in a closed-cycle helium flow cryostat. A dark-field confocal microscope is used to excite and collect the scattered photons from the QD before filtering in a cross-polarisation scheme with a $\sim 10^7$ extinction ratio to suppress the excitation

---

[1] You will get a different answer depending on who you ask this question to, often the answer is related to what they are currently working on so who knows what their real opinions are.

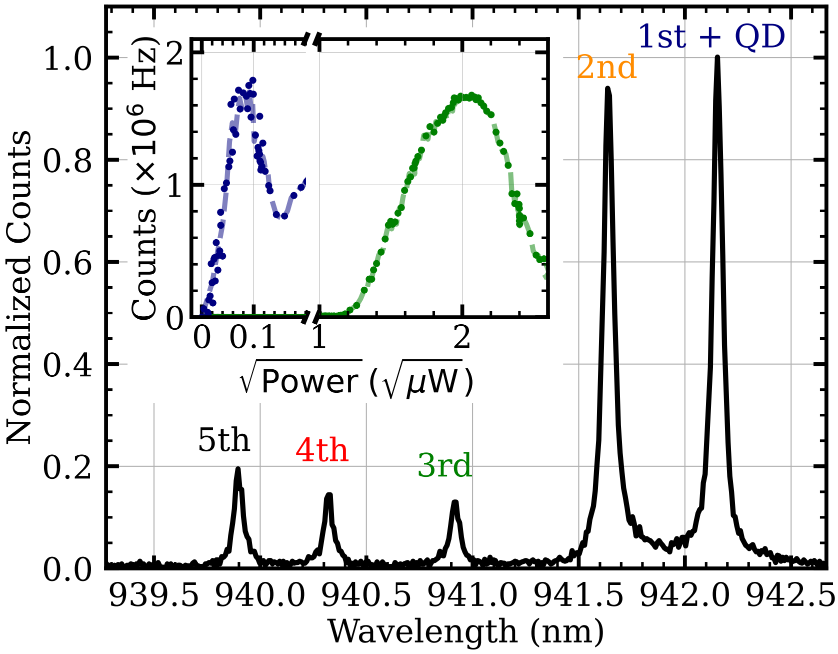

Figure 4.1: Photo-luminescence emission profile of the QD under 820 nm excitation shows cavity modes up to the $5^{\text{th}}$ order. The QD is resonantly coupled to the first cavity mode. Inset shows the detected count rate as a function of the excitation power when the excitation laser is resonant to the 1st (resonant, blue) or 3rd (non-resonant, green) cavity mode.

laser. Credit is given to N. Stoltz, P. Petroff and D. Bouwmeester for QD design and fabrication, and to Z. X. Koong for operating the QD during the course of the measurements presented in this thesis. More details on the device fabrication and design can be found in [97].

The QD was initially characterised by measuring the emission spectrum using a Silicon EMCCD spectrometer under CW excitation at 820 nm. This emission spectrum shows five cavity modes and emission from the QD which was electrically tuned onto resonance with the first cavity mode.

From this point forward we use the term resonant excitation to refer to excitation resonant with the first cavity mode (navy in Fig. 4.1) and quasi-resonant excitation to refer to excitation tuned to the third cavity mode (green in Fig. 4.1). The inset of Fig. 4.1 shows the count rate as a function of excitation power under resonant excitation showing Rabi oscillations (navy) and the quasi-resonant (green) which requires higher excitation power.

Throughout this chapter we use the neutral exciton $X^0$ resonant with the first cavity. Pulsed resonant excitation is carried out with a 80.3 MHz pulse train from a 140 fs Ti:Sapphire laser which is filtered down to 10 ps duration using a 4f pulse shaper. Under pulsed quasi-resonant excitation the Purcell enhancement is found to be $\approx 4$ by measuring the lifetime as a function of QD detuning to the first cavity mode and comparing the lifetime at zero detuning to the asymptotic value at large detuning. At zero detuning lifetime is measured to be $T_1 = 0.2622$ ns. The $T_2$ coherence time of the emission, measured using standard Fourier spectroscopy under $\pi$-pulse resonant excitation, shows $T_2 = 0.348\,(2)\,\text{ns}$, corresponding to a linewidth of 915 (5) MHz. This value is $\approx 1.5$ times larger than the transform-limited linewidth ($1/T_1 = 607\,\text{MHz}$). This limits the HOMI with large time separations between the photons being interfered to $T_2/2T_1 = 66\%$. The central emission wavelength of the QD is 942.33 nm. The second-order correlation of the source and HOMI visibilities are left to be presented in Section 4.4 alongside the same measurements after frequency conversion.

## 4.2 Mid-infrared laser

In order to convert the photons at 942 nm to a target wavelength of 1550 nm a light source at the difference frequency $\lambda = (1/\lambda_{\text{in}} - 1/\lambda_{\text{out}})^{-1}$ is required. For our QD source we need a light source at $\sim 2400$ nm for conversion to the C-band. There are different possible routes to realise this light source. There are a few requirements which any potential light source should satisfy, it should have sufficient output power to not be a limiting factor in the conversion efficiency process, it should be coherent such that it does not degrade the HOMI visibility of the input photons and it should also not introduce additional noise photons that are overlapped in spectrum or time with the converted photons. These requirements narrow the options down to either a laser or OPO/OPA system.

We will highlight some attractive properties of the OPO/OPA option in Section 4.5 which could be realised using the Ti:Sapphire used to drive the QD and a high power source at 1550 nm which could be realised with an erbium-doped fibre amplifier. This would be the complementary DFG process to the one used to frequency convert the single photons. This then causes some experimental problems in that this bright source of 1550 nm light must be fully extinguished before the single-photon conversion step but there are some advantages which are worth exploring.

The alternative option is to find a laser gain medium which works for 2400 nm. Chromium doped into a zinc-selenide host is an attractive option. Cr:ZnSe has a vibronically broadened gain spectrum and has been shown to emit from 1900 − 3300 nm. This has been used to demonstrate tunable CW operation and also pulsed operation with pulse durations down to 43 fs. [2] In this work we operate in a tunable CW mode.

The Cr:ZnSe crystal is pumped by a thulium-doped fibre laser which is capable of producing 20 W CW at 1900 nm.[3] The 1900 nm light is focussed into the Cr:ZnSe crystal with a 100 mm focal length $CaF_2$ lens. The cavity consists of a dichroic input coupler (50 mm radius of curvature (ROC), transmissive at 1900 nm reflective at 2400 nm), a gold mirror (50 mm ROC), two plane silver mirrors and the Cr:ZnSe crystal. The crystal which was not anti-reflection coated is placed at Brewster's angle ($\sim 70^\circ$) to minimise losses due to reflection. The output coupler has a transmission of 60% at 2401 nm, allowing a good trade-off between the cavity enhancement and available output power. The input and output couplers are both custom mirrors from Layertec, all other components are off-the-shelf components. The Cr:ZnSe crystal was mounted on a water-cooled copper plate to control the temperature of the crystal and avoid thermal lensing effects which reduce output power and can cause optical damage [98].

Initially, a silicon prism was used as a dispersive element inside the cavity to control the emission wavelength. For the lasing wavelength of 2400 nm silicon has good transmission properties which allowed for high output powers approaching 3 W. Unfortunately the silicon prism had quite poor wavelength selectivity. The output

---

[2] In this sense Cr:ZnSe is similar to a Ti:Sapphire laser with wavelengths in the mid-infrared.

[3] Cr:ZnSe can be pumped with 1550 nm light from an EDFA which is preferable to the thulium fibre laser due to reduced absorption in air which can cause instabilities in the laser emission. We only learned this after speaking to people who build these lasers for a living.

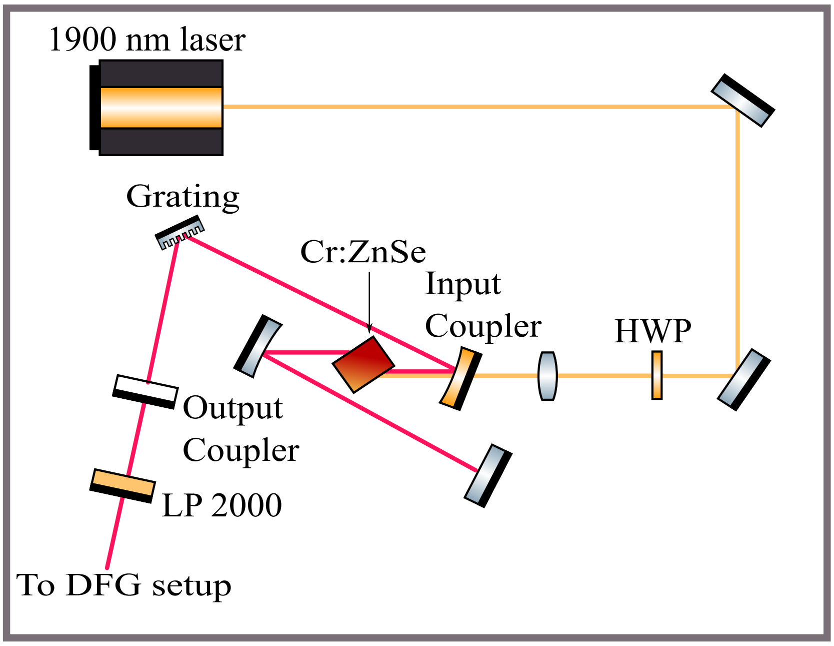

Figure 4.2: Experimental layout of the seed laser used to produce the 2400 nm light. Yellow lines indicate the beam path of the 1900 nm thulium fibre laser, pink represents the 2400 nm light. The first-order diffracted beam from the diffraction grating is sent towards the output coupler. Any noise photons and excess pump light at 1900 nm is removed using long-pass filters at 2000 nm (LP2000).

spectrum was broadband with discrete peaks which fluctuated in relative intensity and position. Fig. 4.3 shows a typical set of spectra measured using an optical spectrum analyser with sensitivity between $1-5\mu$m with a spectral resolution of 2 GHz. A fluctuating pump spectrum will mean that shot-by-shot each photon will have a different spectral shape after the DFG step and which would result in a spectrally mixed state. On top of this the mode hopping meant the output power of the laser was fluctuating over time such that optimising the other factors which affect the conversion efficiency such as waveguide coupling and mode overlap would prove difficult.

The spectral stability of the laser needed to be improved in order to proceed. The intuition was that the prism did not have enough dispersion to create a narrow enough gain bandwidth. Having a narrower gain bandwidth would mean fewer cavity modes inside the gain bandwidth and perhaps a more stable spectrum. A diffraction grating with 450 lines/mm was inserted in place of the silicon prism with the first order diffracted beam aligned to the output coupler. This dramatically

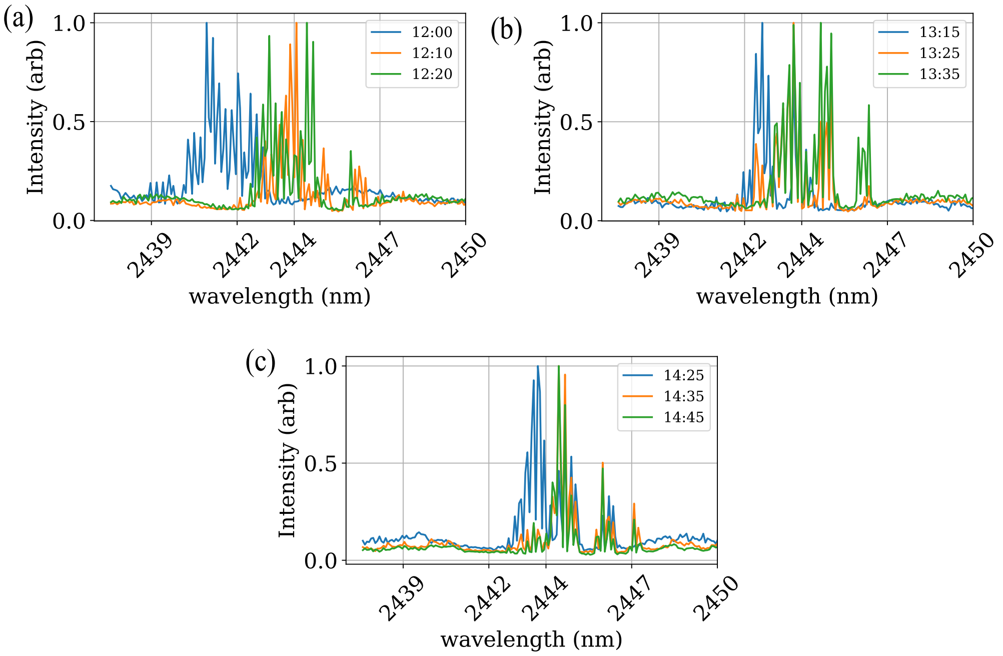

Figure 4.3: The measured spectrum using an OSA of the 2400 nm seed laser over two hours of measurement using a silicon prism as the dispersive element. Frequency converting single photons using this laser would result in a broadband spectrally mixed state.

improved the spectral stability of the laser. The spectrum consists of one narrow Lorentzian peak with a FWHM of around 4 GHz, see Fig. 4.4. The price of this additional spectral stability is the higher round-trip loss from the diffraction grating compared to the silicon prism, this results in a lower slope efficiency of 5% compared to 13% for the silicon prism where the slope efficiency is the ratio of the optical power in at 1900 nm to the output power at 2400 nm.

With the FWHM of 4 GHz the laser emits over multiple longitudinal modes (lasing over multiple FSR). The FSR of the cavity is measured using a second-order correlation measurement, $g^{(2)}$, of frequency converted laser light using SNSPDs. Consider the superposition of two different waves with slightly different frequencies from different cavity lines,

$$E(\omega) = A\exp(i\omega t) + A\exp(i(\omega+\delta)t) \tag{4.1}$$

The intensity of this field $I \propto |E|^2$ will vary with the beat frequency $\delta$. This can be seen in the $g^{(2)}$ measurement which is approximately equal to one as expected

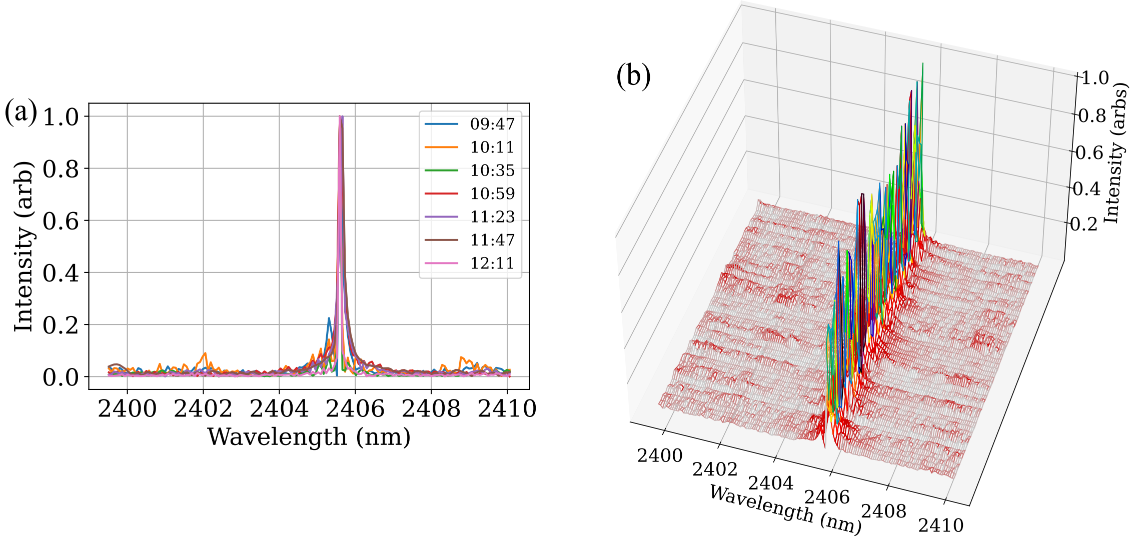

Figure 4.4: The measured spectrum with a grating as the dispersive element inside the cavity over approximately two hours of measurement. The spectral fluctuations are massively reduced compared to the silicon prism arrangement shown in Fig. 4.3. (b) contains the same data as (a).

for a coherent state but shows small oscillations. Taking a Fourier transform of this trace shows a peak with a fundamental frequency of 177 MHz with other peaks at integer multiples of this frequency due to beating between cavity modes seperated by more than one FSR. This agrees well with the expected FSR of the cavity based on the cavity length of around 0.8 m. Given the 4 GHz bandwidth we estimate around 22 longitudinal modes are contributing to the laser output. An uncoated silicon etalon was purchased and inserted into the cavity in an effort to select a single mode for lasing, unfortunately due to the large reflection losses lasing was not possible. The affect of these different longitudinal modes on the coherence of the frequency-converted single photons is discussed in Section 4.4. Future work on this laser should focus on reducing the number of modes in the emission spectrum through tighter dispersion control and making the cavity more compact to increase the FSR. Active locking of the emission wavelength will also improve the quality of the converted single photons.

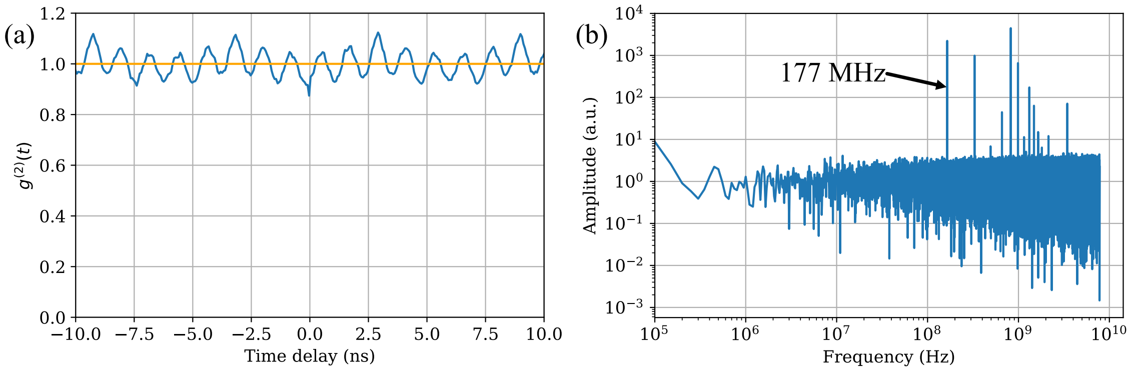

Figure 4.5: (a) Measured second order correlation of laser light after frequency conversion. The oscillations in the measureed $g^{(2)}$ are attributed to intensity fluctuations from mode beating between different cavity modes. (b) Shows the Fourier transform of the $g^{(2)}$ timetrace, the initial peak is at 177 MHz with further peaks at integer multiples corresponding to beating between non-adjacent cavity modes.

### 4.2.1 Experimental tips for aligning a cavity

In this section I quickly highlight some points which may be of use to future students working on this system based on the numerous times I have had to realign this cavity. Typically, the cavity requires alignment once per day to ensure consistent central wavelength between measurements.

#### Alignment laser

Use a visible wavelength laser and a flip mirror to at least approximately position all of the optical components. A HeNe laser is almost always an excellent choice for this. Using the pump laser at 1900 nm is a bad option to try and position the components, it isn't easy to see with a fluorescent detector card and the minimum emission is around 100 mW.

#### Use a camera

When the cavity is roughly aligned a camera to view the different cavity round trips is critical to getting the laser working in an approximately Gaussian fundamental mode. It is possible to align the cavity and have lasing with just a power meter to feedback on the mirror positions, but lasing can occur in higher order transverse modes which couple poorly into the LN waveguide.

### Getting the grating into the cavity

The trick to getting the cavity aligned with the grating in the correct position is to use a pair of output couplers. Initially the cavity should be aligned with no grating in place. The first output coupler should be positioned between the Cr:ZnSe crystal and the position of the grating in Fig. 4.2. The laser will then output light at whatever wavelength the round trip loss is lowest. At this point the laser light should be sent to the diffraction grating *outside* the cavity. The first order diffracted beam should then be sent to the second output coupler and the reflected beam should be aligned back onto the incoming beam. At this point the first output coupler can be removed. Some small adjustment of the grating angle and second output coupler should then recover lasing operation. At this point the grating can be adjusted to centre the emission at the desired wavelength.

## 4.3 Lithium niobate waveguide

The DFG process occurs in a 48 mm LN waveguide fabricated by NTT Electronics. The chip consists of 12 ridge waveguides with poling periods ranging from $26 - 26.25\mu$m. The chip was initially designed for conversion between 939 nm light to 1550 nm with a seed beam of 2380 nm in a type-0 process, $e \rightarrow e + e$. The crystal is triple anti-reflection coated for these wavelengths. It was found that temperature tuning the crystal 30 degrees hotter than the quoted phasematching temperature was enough to phasematch the dot wavelength of 942 nm converted to 1550 nm. The dimensions of the waveguides are designed to be approximately single mode at 1550 nm with dimensions of $13\mu\text{m} \times 13.4\mu\text{m}$.

The coupling into the waveguide was optimised for the seed beam first. As wavelength decreases the waveguide becomes more multimode, so the seed beam is the hardest to couple in and the quantum dot light at 942 nm is the easiest. A NIR-coated aspheric lens with 11 mm focal length is used to couple light into the waveguide. This coating reduces the loss for the single photons but imparts significant loss of around 40% on the 2400 nm beam. To compensate for the chromatic aberration

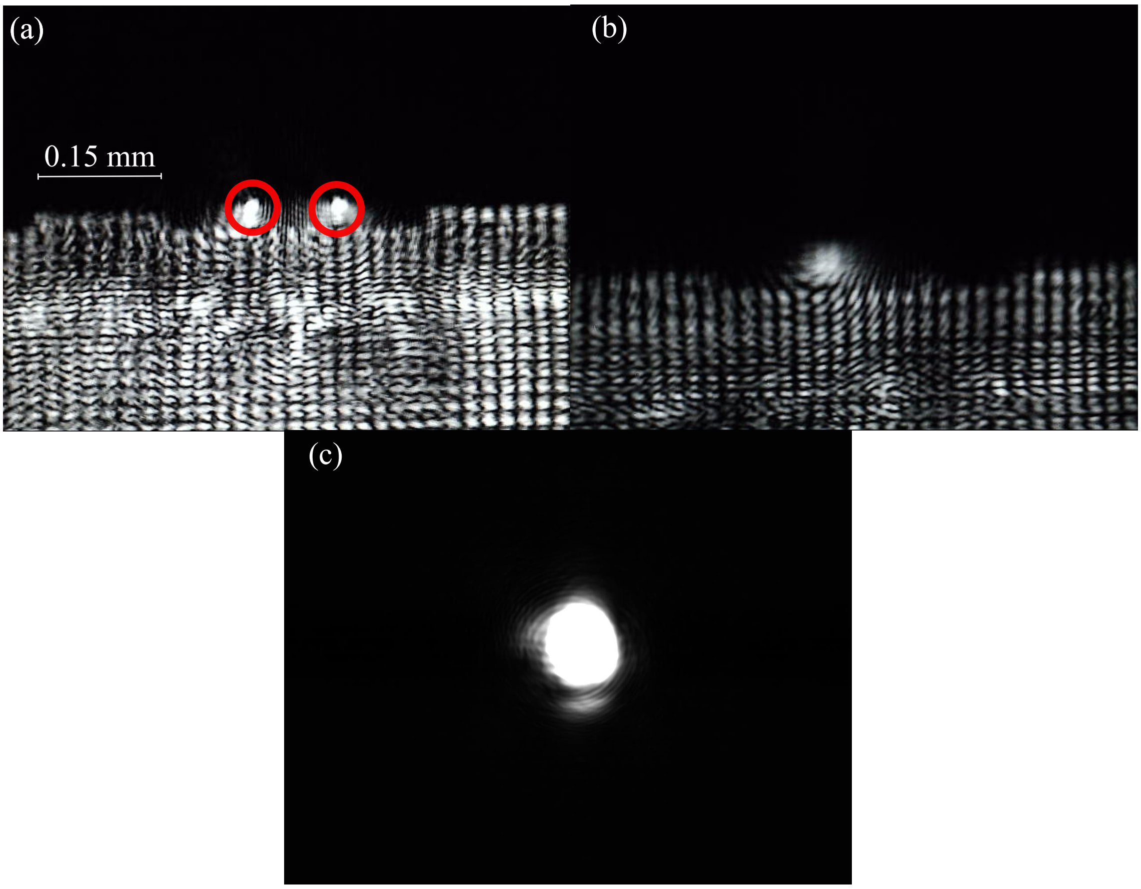

Figure 4.6: Far field images of the waveguide chip taken with a CMOS camera used when coupling into the waveguides. Image (a) shows two ridge waveguides marked with red, the chip is illuminated with a 942 nm laser which is poorly coupled into the guides and shows scattering through the entire chip. (b) As the coupling improves into the waveguide, the substrate and second waveguide becomes less visible. (c) With the light correctly coupled only one bright spot is visible.

of the coupling lens an additional 100 mm focal length lens is inserted in the QD beam path. This choice of lens was found empirically by testing various focal lengths and optimising over the conversion efficiency. The 1550 nm light at the output of the waveguide is collimated with a second aspheric lens, focal length 11 mm, coated for low loss at 1550 nm. Waveplates are used to rotate the polarisation of the QD and seed light to align with the extraordinary axis of the crystal which is vertically oriented with respect to the optical table.

The coupling efficiency for the QD beam including coupling into, propagation and outcoupling losses is found to be 83% found by comparing the power before and immediately after the waveguide. The efficiency for the seed beam was found to be 32%.

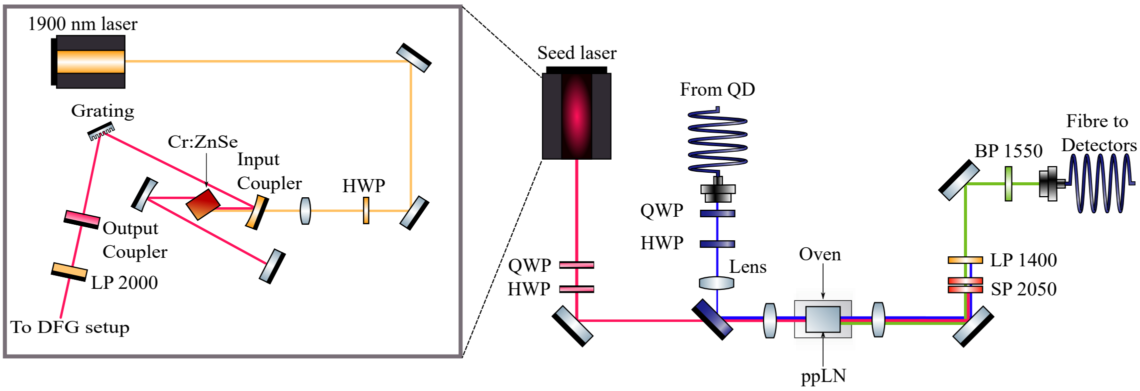

Figure 4.7: Difference-frequency generation schematic. Blue lines indicate the optical path of the QD photons. Pink lines represent the path of the 2400 nm seed light. Green lines represent the path of the 1550 nm light. The polarisation of both beams is aligned to the extraordinary axis of the ppLN crystal with a quarter-wave plate (QWP) and half-wave plate (HWP). A 100 mm focal length lens is used in the QD beam path to mode match the seed beam at the waveguide facet. The green lines represent the converted 1550 nm light after the frequency conversion. The converted light is sent through two short pass filters at 2050 nm (SP 2050), a 1400 nm long pass filter (LP 1400) and a bandpass filter at 1550 nm (BP 1550) before being collected in a single mode fibre for detection.

The filtering stage consists of two shortpass filters at 2050 nm (>OD 4), which are used to remove seed light impinging on the collection fibre; a longpass filter at 1400 nm (>OD 5) to remove weakly phase-matched second-harmonic generation from the seed beam and unconverted quantum dot light; and finally, a 2.8 nm FWHM bandpass filter (>OD 4) to isolate the converted single photons. The converted 1550 nm light is collected into a single mode fibre with 86% coupling efficiency and sent to SNSPDs with a nominal quantum efficiency greater than 80%.

## 4.4 Conversion results

The DFG conversion efficiency is characterised by sending CW coherent light from a Topica DL Pro CW laser into the QFC setup. From the discussion in the first chapter on multimode FC (see Fig. 2.5) the conversion efficiency does not depend on the temporal mode shape of the input light for FC pumped by a CW seed. This allows characterisation with a CW laser despite the single photons' decaying exponential wavepacket. Under the approximation that the seed beam is unamplified and considerably higher intensity than all other modes, the conversion efficiency measured with a low power (500 $\mu$W) CW coherent field is equivalent to the single-photon conversion efficiency. The efficiency is defined as the ratio of photon number and therefore can be related to the optical power measured as,

$$\eta = \frac{n_{\text{out}}}{n_{\text{in}}} = \frac{P_{\text{out}}}{P_{\text{in}}}\frac{\lambda_{\text{out}}}{\lambda_{\text{in}}} \tag{4.2}$$

using the fact that the energy of a beam containing $n$ photons is $E = \frac{nhc}{\lambda}$.

The conversion efficiency can be written in terms of experimentally useful quantities as

$$\eta = \eta_{max} \sin^2\left(\sqrt{\eta_{nor}P}\ L\right), \tag{4.3}$$

where $\eta_{max}$ is the maximum possible conversion efficiency, $\eta_{nor}$ is the normalised conversion efficiency of the process, $P$ is the input power, and $L$ is the waveguide length. The fit gives a normalised conversion efficiency (to waveguide length in the limit of small pump powers [99]) of $\eta_{nor} = 44\,(1)\ \%\ /\ \left(\text{W cm}^2\right)$. The maximum external conversion efficiency i.e. the ratio of photons collected into single-mode fibre after the conversion stage to the number of NIR photons impinging on the waveguide is $\eta_{max} = 38\,\%$, leading to a maximum internal conversion efficiency of 56.7 (4) % when taking losses into account. This $\eta_{max}$ is higher than previously reported values for NIR QD frequency conversion to 1550 nm with similar waveguides [33].

Noise photons are measured by recording the count rate as a function of power with the SNSPD with the QD beam path blocked. This count rate was found to increase linearly with a gradient of 12 Hz/mW. As the noise count rate increased linearly with pump power it is believed the noise is due to anti-Stokes Raman scattering from the seed beam. Another possible contribution to the noise photons which is linear with pump power is leakage of the pump beam through all of the filters and collected in the final fibre. We rule this contribution out by removing one of the LP2050 filters, see Fig. 4.7, the noise rate did not change for this scenario which would be expected if the seed beam was making it through the filtering stage. For all conversion efficiencies of interest the SNR is greater than 250 indicating the noise

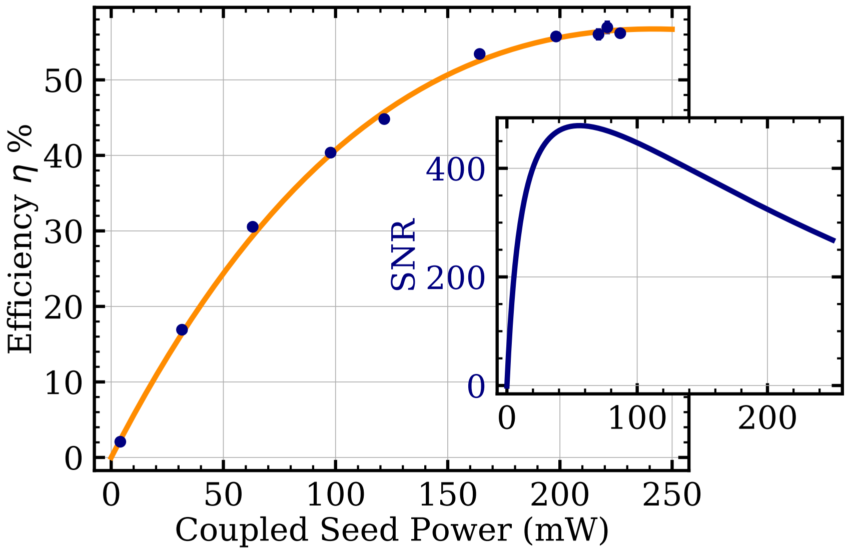

Figure 4.8: Conversion efficiency of the difference-frequency generation process as a function of seed power coupled into the waveguide. The power in the waveguide is determined by measuring the pump power after the waveguide and factoring out the loss through the aspheric collimation lens anti-reflection coated for 1550 nm. The transmission through this lens is measured to be 64 % at the pump wavelength. The data is fitted with Eq. (4.3). Inset shows the signal to noise ratio for off-resonant excitation with a measured noise count rate of 12 (1) Hz/mW. Frequency conversion with similar ppLN devices where anti-Stokes scattering is expected to dominate have demonstrated a noise flux rate per unit filter bandwidth of 5.8 Hz/mW/nm [35], comparable to our noise flux rate of 5.3(4) Hz/mW/nm.

contribution from the DFG process itself has minimal affect on the multiphoton component of the telecom signal.

We now compare the characteristics of the converted telecom photons to the QD NIR photons. For non-resonant characterisation, the QD photons are spectrally filtered with a grating filter with a 30 GHz FWHM to suppress the excitation laser. We detect a count rate of 1.85(5) MHz at an excitation power of 6.8 $\mu$W. The grating filter was removed when characterising the converted photons as low-loss bandpass filters were used at 1550 nm. For resonant driving, we detect a count rate of 1.46(4) MHz. This value is slightly lower than for off-resonant excitation due to the presence of spectral fluctuations [100]. After QFC, the detected count rate at 1550 nm, for the off-resonant and on-resonant case is 856(18) kHz and 456(14) kHz, respectively. Comparing the NIR and telecom counts under resonant excitation gives an end-to-end conversion efficiency of $\approx 35$ %, after accounting for the difference in the detection efficiency of both NIR ($\sim 90\%$) and telecom C-band ($\sim 80\%$) detec-

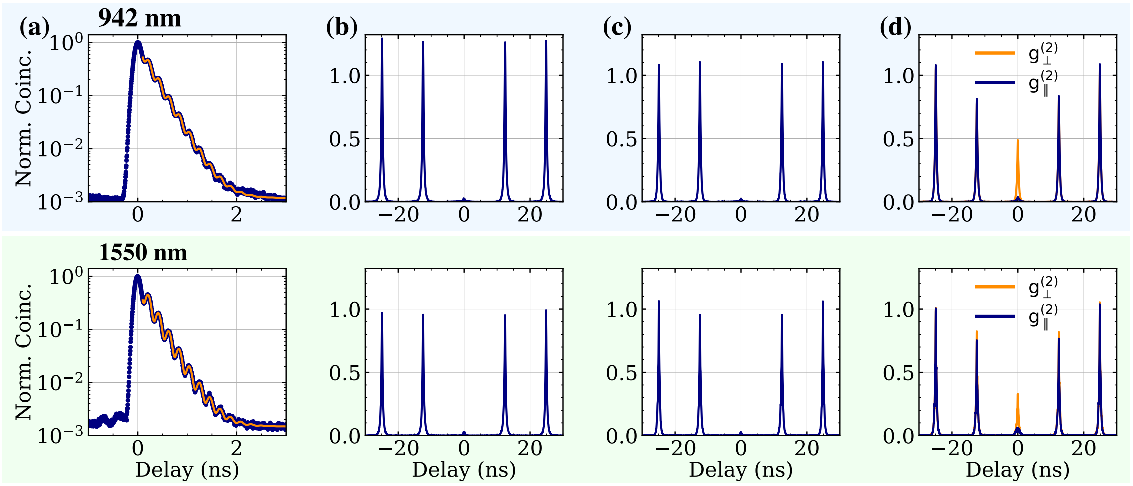

Figure 4.9: Characterisation of the single-photon properties before (upper row) and after (lower row) QFC. **(a)** Time-resolved emission spectra under pulsed resonant excitation reveals an exponential decay which gives the emitter's lifetime $T_1$ and a fast oscillation indicating the quantum beating between the fine-structure peaks of the neutral exciton emission, $\Delta_{\mathrm{fss}} = 4.807\,(3)\,\mathrm{GHz}$. **(b, c)** Second-order intensity correlation histogram $g^{(2)}$, of the emitted photons under off-resonant (b) and resonant (c) excitation. The lack of coincidences in the central peak indicates the low probability of multi-photon emission. **(d)** Two-photon interference of consecutively scattered photons delayed by 12.5 ns, prepared in cross ($g^{(2)}_{\perp}$) and parallel ($g^{(2)}_{\parallel}$) polarisations, under resonant $\pi$-pulse excitation. The extracted photon indistinguishability, given by the ratio of zero-delay-coincidences from both configurations, along with the extracted values ($T_1$ and $g^{(2)}(0)$) from the fits (solid lines) are summarised in Table 4.1.

tors. This agrees well with the measured loss budget through the optical components including the conversion efficiency. The difference in efficiency for off-resonant excitation is accounted for by the loss of the grating filter.

Fig. 4.9 shows the comparison between the performance of the QD signal before and after QFC. The lifetime measured under resonant excitation in Fig. 4.9(a) remains unchanged within experimental error after conversion. The oscillation in the time-resolved emission, indicative of the quantum beating of the $X^0$ fine-structure splitting, shows a frequency of 4.807 (3) GHz extracted from a fit of, $\exp(-t/\tau)\,(1 + A\sin(\Delta_{FSS}t))$ to the data [101]. The equivalent oscillation after the QFC process is unchanged (4.803 (1) GHz), indicating that the CW-seeded frequency conversion preserves the temporal mode of the input photons as we would expect from the discussion of multimode FC.

Next, we measure the second-order intensity correlation $g^{(2)}$ for the converted and

| | 942 nm | 1550 nm |
|---|---|---|
| Lifetime $T_1$ (ns) | 0.2622 (2) | 0.2621 (2) |
| Resonant count rate (kHz) | 1,460 (40) | 456 (14) |
| Off-resonant count rate (kHz) | 1,850 (50) | 856 (18) |
| Off-resonant $g^{(2)}(0)$ | 0.045 (0) | 0.051 (1) |
| Resonant $g^{(2)}(0)$ | 0.040 (0) | 0.043 (1) |
| Resonant $\mathrm{V_{HOM}}$ | 0.88 (1) | 0.60 (1) |
| Resonant $M_s$ | 0.95 (1) | 0.67 (2) |

Table 4.1: Summary of the lifetime, count rate, $g^{(2)}(0)$ and indistinguishability $\mathrm{V_{HOM}}$ for converted and unconverted photons. Values are obtained from measurement results, illustrated in Fig. 4.9. The corrected photon indistinguishability $M_S$ is estimated based on the measured $g^{(2)}(0)$ and uncorrected $\mathrm{V_{HOM}}$[108]. The error, given by the standard deviation from the fit, is included in brackets.

unconverted photons. For a perfect single-photon source $g^{(2)}(0) = 0$, indicating the absence of multi-photon emissions. Under off-resonant driving, Fig. 4.9(b), we observe a slight increase from $g^{(2)}(0) = 0.045\,(0)$ to $g^{(2)}(0) = 0.051\,(1)$ before and after the QFC process, respectively. We observe similar values under resonant driving, Fig. 4.9(c), demonstrating near-ideal single-photon emission with $g^{(2)}(0) = 0.040\,(0)$ and $g^{(2)}(0) = 0.043\,(1)$ before and after the QFC process, respectively. The slight increase in the normalized coincidences in the uncorrelated side peaks in the HBT histogram is due to blinking of the emitters, a common effect resulting from QD coupling to the solid-state charge environment [102]. The imperfection in $g^{(2)}(0)$ can be due to imperfect suppression of the cavity emission due to cavity feeding [103–105], slight imperfection in the wave-plate retarders used in our confocal microscope, and presence of multi-photon capture processes [106, 107]. Nevertheless, with a modest increase in $g^{(2)}(0)$ after the QFC process, we have demonstrated near background-free single-photon frequency conversion from NIR to the telecom C-band, with the photon-number purity predominantly limited by the quantum dot.

To demonstrate that our QFC setup preserves photon coherence, we perform HOMI between photons emitted from two consecutive excitation pulses. We use an unbalanced Mach-Zehnder interferometer with a free-space delay of 12.5 ns to match photons temporally on a 50/50 beam splitter, the setup is similar to Fig. 3.17 without the heralding detectors and the fibre-delay replaced with a free-space delay line. The polarisation of the photons is controlled by a linear plate polariser and HWP to set the orthogonal and parallel polarisation states. We measure the coincidence counts for parallel and perpendicular polarised photons and evaluate the visibility as $\mathrm{V_{HOM}} = 1 - g^{(2)}_{\parallel}/g^{(2)}_{\perp}$. For a pair of indistinguishable photons, $\mathrm{V_{HOM}} = 1$. For resonant excitation we achieve an interference visibility of $\mathrm{V_{HOM}} = 0.88\,(1)$ before QFC. As the delay is increased we expect the visibility to tend towards $\mathrm{V_{HOM}} \rightarrow \mathrm{T_2/2T_1} \approx 0.66$ at longer delays, inferred from the coherence time, $T_2$ measured using a Michelson interferometer [109, 110]. We calculate the single photon indistinguishability $M_s$ as $M_s = \frac{\mathrm{V_{HOM}}+g^{(2)}(0)}{1-g^{(2)}(0)}$[108]. This gives an upper bound to the HOM visibility taking the finite $g^{(2)}\,(0)$ into account. Before conversion, $M_s$ is equal to $0.95\,(1)$. After conversion we find the raw visibility and corrected indistinguishability to be $0.60\,(1)$ and $0.67\,(2)$ respectively. The raw and corrected visibilities are calculated by summing the raw counts in the central peaks in Fig. 4.9 (d).

The reduced HOMI is attributed to the spectral instability in the seed beam. At this point it is unclear if it is due to fluctuating power in each of the cavity modes in time or if the position of the cavity modes in frequency space is changing due to fluctuations of the cavity length. Regardless it is expected that locking the emission wavelength of the cavity to a fixed reference and having a single longitudinal mode laser would improve the indistinguishability of the converted photons to match the levels before conversion. This has recently been demonstrated with a quantum dot using a frequency conversion setup almost identical to the one used in this work except for a commercial single-mode Cr:ZnSe laser [93].

At this point it is worth quickly comparing this work to quantum dots emitting natively at telecom wavelengths. Lower multiphoton noise has been demonstrated $g^{(2)}\,(0) \sim 4 \times 10^{-4}$ alongside count rates on the order of 200 kHz [111], however two-photon interference visibilities lag behind the value demonstrated in this work or other frequency-converted sources [93, 94].

## 4.5 From CW to pulsed conversion

Having explored the multimode CW version of FC experimentally and shown that the mode profile is left almost unchanged before and after conversion, the lifetime measurements in Fig. 4.9 are an example of this, we switch now to the pulsed version and show theoretically that it can be used to improve the spectro-temporal purity of photons emitted from a noisy single emitter. This work takes inspiration from the quantum pulse gate [66] and quantum pulse shaper [112]. Simply put, a single-mode frequency conversion process can reject photons which do not overlap spectrally and temporally with the mode defined by the Schmidt decomposition of the conversion process, Fig. 2.4. Luckily with type-0 conversion from around 940 nm to 1550 nm the group velocity of the 2400 nm pump and 1550 nm single photon have similar group velocities which means a single-mode FC process similar to one outlined in Fig. 2.4 is possible. A single-mode FC process can be seen as a filter at the amplitude level, not at the intensity level which can be done with spectral or temporal filtering alone. Couple this to the conversion process where the photons are converted to a telecom wavelength this technique might find application in connecting independent single-photon emitters in a future quantum network where each of the emitters has an independent dephasing environment. Recently it has been shown that quantum memories can also have a similar spectral purifying operation but without frequency conversion over a large enough spectral range to reach telecom wavelengths [113].

We use a simplified model of the emission from a quantum dot, considering the photons as transform-limited and then introducing time and frequency jitter and show that both effects can be removed after frequency conversion. A full treatment would include the dynamics of the QD levels coupled to a phononic bath under different excitation schemes. The FC modelling should also include the effects of modal dispersion in the waveguide and time-ordering effects. We opt for a simpler analysis here which demonstrates the principles involved in the clearest way possible, a more rigorous approach will be the content of future work.

### 4.5.1 Density matrix for single photons from a quantum dot

Pure single photons from a quantum dot have a transform-limited decaying exponential waveform,

$$|\psi\rangle = \mathcal{N} \int \mathrm{d}t \Theta\left(t\right) \exp\left(-\gamma t\right) a^{\dagger}\left(t\right) |0\rangle\,, \tag{4.4}$$

where $\Theta\left(t\right)$ is the Heaviside step function, $\gamma$ defines the decay rate of the quantum dot and $\mathcal{N}$ is a normalisation factor.

In the Fourier domain this can be expressed as

$$|\psi\rangle = \int \mathrm{d}\omega g\left(\omega, \mu, \gamma, t\right) a^{\dagger}\left(\omega\right) |0\rangle \tag{4.5}$$

$$g\left(\omega, \mu, \gamma, t\right) = \sqrt{\frac{\gamma}{\pi}} \frac{1}{\gamma - i\left(\omega - \mu\right)} \exp\left(-i\omega t\right), \tag{4.6}$$

where $g\left(\omega, \mu, \gamma, t\right)$ is the frequency domain representation of the single-photon wavepacket and we have explicitly included the central frequency $\mu$ and the linear spectral phase due to propagation for a time $t$ from emission. The reason for explicitly including this time will become clear when considering the effects of emission time jitter.

The density matrix for this pure state is then given by

$$\rho = \int \mathrm{d}\omega_1 \int \mathrm{d}\omega_2 f\left(\omega_1, \omega_2, \mu, \gamma, t\right) a^{\dagger}\left(\omega_1\right) |0\rangle \langle 0| a\left(\omega_2\right), \tag{4.7}$$

where

$$f\left(\omega_1, \omega_2, \mu, \gamma, t\right) = g\left(\omega_1, \mu, \gamma, t\right) g^{*}\left(\omega_2, \mu, \gamma, t\right) \tag{4.8}$$

.

### 4.5.2 Frequency jitter

We want to include the effects of frequency jitter on the quantum dot emission due to charge noise in the environment of the quantum dot. We can take consider the spectral diffusion to be normally distributed in around the central frequency $\mu$ with a deviation $\delta$. The resulting state is

$$\rho_{(\delta\mu)} = \int \mathrm{d}\Delta \int \mathrm{d}\omega_1 \int \mathrm{d}\omega_2 \\ G\left(\Delta,\delta\right) f\left(\omega_1,\omega_2,\mu+\Delta,\gamma,t\right) a^\dagger\left(\omega_1\right)\left|0\right\rangle\left\langle 0\right| a\left(\omega_2\right),$$

with the weight function

$$G\left(\Delta,\delta\right) = \frac{1}{\delta\sqrt{2\pi}}\exp\left(-\frac{\Delta^2}{2\delta^2}\right). \tag{4.9}$$

Carrying out the integration over the frequency jitter $\Delta$ the resulting density matrix can be written as

$$\rho_{(\delta\mu)} = \int \mathrm{d}\omega_1 \int \mathrm{d}\omega_2 \\ h\left(\omega_1,\omega_2,\mu,\gamma,t,\delta\right) a^\dagger\left(\omega_1\right)\left|0\right\rangle\left\langle 0\right| a\left(\omega_2\right), \tag{4.10}$$

with the density matrix elements given by,

$$h\left(\omega_1,\omega_2,\mu,\gamma,t,\delta\right) = \\ \exp\left(-\frac{\left(-\mu+i\gamma+\omega_1\right)^2+\left(\mu+i\gamma-\omega_2\right)^2+2it\delta^2\left(\omega_1-\omega_2\right)}{2\delta^2}\right)\times \\ \gamma\left[\exp\left(\frac{\left(\mu+i\gamma-\omega_2\right)^2}{2\delta^2}\right)\left(i+\operatorname{erfi}\left(\frac{\mu-i\gamma-\omega_1}{\sqrt{2}\delta}\right)\right)- \\ \exp\left(\frac{\left(-\mu+i\gamma+\omega_1\right)^2}{2\delta^2}\right)\left(-i+\operatorname{erfi}\left(\frac{\mu+i\gamma-\omega_2}{\sqrt{2}\delta}\right)\right)\right]\times \\ \frac{1}{\left(\sqrt{2\pi}\delta\left(2i\gamma+\omega_1-\omega_2\right)\right)} \tag{4.11}$$

Where $\operatorname{erfi}\left(z\right) = -i\operatorname{erf}\left(iz\right)$ and erf is the error function.

Note that in the limit of no spectral jitter we recover the pure state density matrix elements

$$\lim_{\delta\to 0} h\left(\omega_1,\omega_2,\mu,\gamma,t,\delta\right) = \frac{\gamma\exp\left(-it\left(\omega_1-\omega_2\right)\right)}{\pi\left(\mu-i\gamma-\omega_1\right)\left(\mu+i\gamma-\omega_2\right)} = f\left(\omega_1,\omega_2,\mu,\gamma,t\right). \tag{4.12}$$

For $\rho_{\delta\mu}$ to be a valid density matrix the weight function must satisfy

$$\begin{aligned} \rho = \rho^\dagger \rightarrow & h\left(\omega, \omega', \mu, \gamma, t\right) = h^*\left(\omega', \omega, \mu, \gamma, t\right) \\ \mathrm{Tr}\left(\rho\right) = 1 \rightarrow & \int \mathrm{d}\omega h\left(\omega, \omega, \mu, \gamma, t\right) = 1. \end{aligned} \tag{4.13}$$

The purity can be calculated as,

$$\mathrm{Tr}\left(\rho^2_{(\delta\mu)}\right) = \int \mathrm{d}\omega \int \mathrm{d}\omega' h\left(\omega, \omega', \mu, \gamma, t\right) h\left(\omega', \omega, \mu, \gamma, t\right). \tag{4.14}$$

### 4.5.3 Emission time jitter

For timing jitter we replicate the same treatment as spectral jitter but now we introduce a variation in the time since emission $t$.

$$\begin{aligned} \rho_{(\delta t)} = & \int \mathrm{d}\Delta \int \mathrm{d}\omega_1 \int \mathrm{d}\omega_2 \\ & G\left(\Delta, \delta\right) f\left(\omega_1, \omega_2, \mu, \gamma, t + \Delta\right) a^\dagger\left(\omega_1\right) \left|0\right\rangle \left\langle 0\right| a\left(\omega_2\right). \end{aligned}$$

In an analogous way the explicit integral over the emission time can be carried out which gives

$$\begin{aligned} \rho_{(\delta t)} = & \int \mathrm{d}\omega_1 \int \mathrm{d}\omega_2 \\ & p\left(\omega_1, \omega_2, \mu, \gamma, t, \delta\right) a^\dagger\left(\omega_1\right) \left|0\right\rangle \left\langle 0\right| a\left(\omega_2\right), \end{aligned}$$

with density matrix elements are given by,

$$p\left(\omega_1, \omega_2, \mu, \gamma, t, \delta\right) = \frac{\gamma \exp\left[-\frac{1}{2}\left(i2t\left(\omega_1 - \omega_2\right) + \delta^2\left(\omega_1 - \omega_2\right)^2\right)\right]}{\pi\left(\mu - i\gamma - \omega_1\right)\left(\mu + i\gamma - \omega_2\right)}. \tag{4.15}$$

In the limit of no time jitter we recover the same density matrix as in the case of no spectral jitter as expected

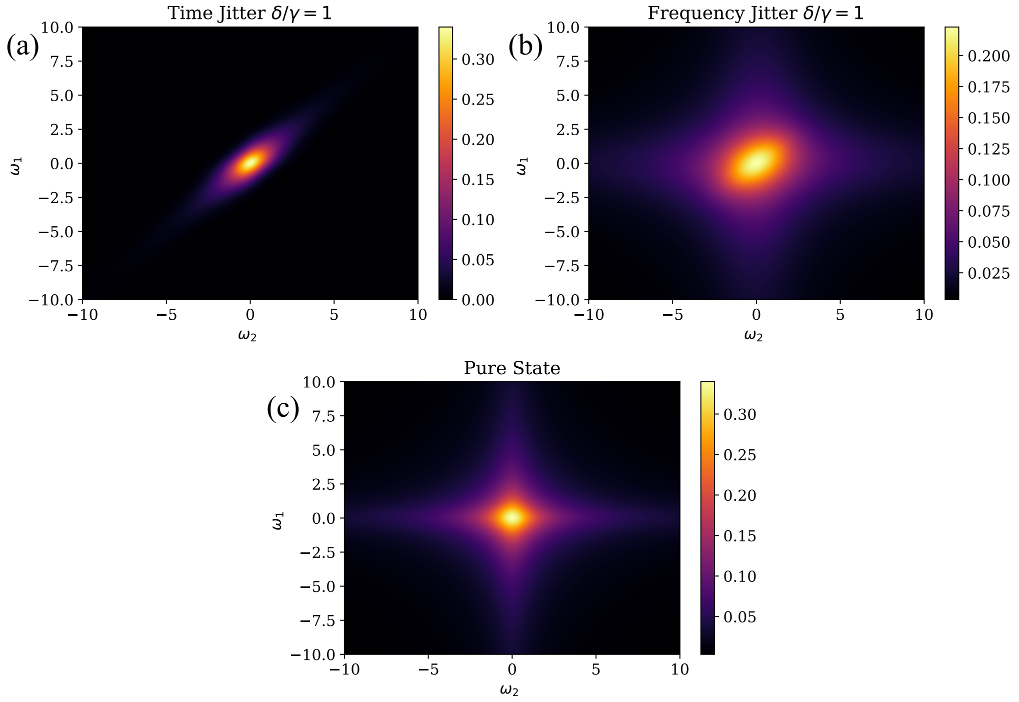

Figure 4.10: Plots of the absolute value of the different density matrices for (a) time jitter with purity 0.3 (b) frequency jitter with purity 0.75 and the pure state which was the starting point for the noisy cases. Notice that both noise cases make the matrices more diagonal as expected for a mixed state.

### 4.5.4 Calculating the output state

The output state of the frequency conversion process can be calculated by taking a Taylor expansion of Eq. (2.25),

$$|\psi\rangle = \left(\mathbb{I} + \int\int \mathrm{d}\omega_o \mathrm{d}\omega_i f\left(\omega_o, \omega_i\right) a^\dagger\left(\omega_o\right) b\left(\omega_i\right) + ...\right) |0,1\rangle \,. \tag{4.16}$$

Taking the first order term in the expansion the output can be written as,

$$|\psi\rangle = \int\int\int \mathrm{d}\omega_o \mathrm{d}\omega_i \mathrm{d}\omega_j f\left(\omega_o, \omega_i\right) g\left(\omega_j\right) a^\dagger\left(\omega_o\right) b\left(\omega_i\right) b^\dagger\left(\omega_j\right) |0,0\rangle \,, \tag{4.17}$$

where the spectral shape of the input single photon $g\left(\omega_j\right)$ is included. A little bit of work with the commutation relations and dropping the input state which is now vacuum, the output state can be written as

$$|\psi\rangle = \int\int \mathrm{d}\omega_o \mathrm{d}\omega_i f\left(\omega_o, \omega_i\right) g\left(\omega_i\right) a^\dagger\left(\omega_o\right) |0\rangle \,. \tag{4.18}$$

This then allows us to make the identification that an input photon at frequency $\omega_i$ is mapped to output frequency $\omega_o$ with the coupling given by $f\left(\omega_o, \omega_i\right)$. This can be extended to the case of a density matrix with elements $p\left(\omega_1, \omega_2\right)$

$$\rho = \int\int\int\int \mathrm{d}\omega_1 \mathrm{d}\omega_2 \mathrm{d}\omega_3 \mathrm{d}\omega_4 f\left(\omega_3, \omega_1\right) p\left(\omega_1, \omega_2\right) f^*\left(\omega_2, \omega_4\right) a^\dagger\left(\omega_3\right) \left|0\right\rangle \left\langle 0\right| a\left(\omega_4\right). \tag{4.19}$$

The mapping from input state to output state is not solved analytically so Eq. (4.19) is replaced with the discretised version to be calculated numerically,

$$\rho_{i,l} = f_{i,j} p_{j,k} f^*_{k,l}. \tag{4.20}$$

We are now in position to consider different frequency conversion processes and how they affect the purity of the output state.

### 4.5.5 Numerical results on pulsed frequency conversion

The first step is finding the JSA for the pulsed FC process with the three wavelengths we are considering. We choose a pump duration of around 1 ps with a Gaussian spectrum and a crystal length of 48 mm to match the waveguide used in the experimental work in this section.

We follow Eq. (4.20) to calculate the output state and plot the purities as a function of the input state purity for different frequency and time jitter strengths. We vary the pump duration to show that as the pump duration increases, the process becomes more multimode and the purity of the output state is lower for the same noise strength. We set the bandwidth of the QD single photon $\gamma$ to be 1 GHz which is similar to the linewidth of the QD used experimentally in this work.

The mapping from input frequency to output frequency is shown in Fig. 4.11 (b), but how the frequency conversion process can erase time jitter from the QD is less obvious. For the JSA to be aligned almost vertically in Fig. 4.11 the pump and telecom photon have almost the same group velocity. This is then how the time-jitter is removed, the pump pulse at 2400 nm walks through the QD photon and the

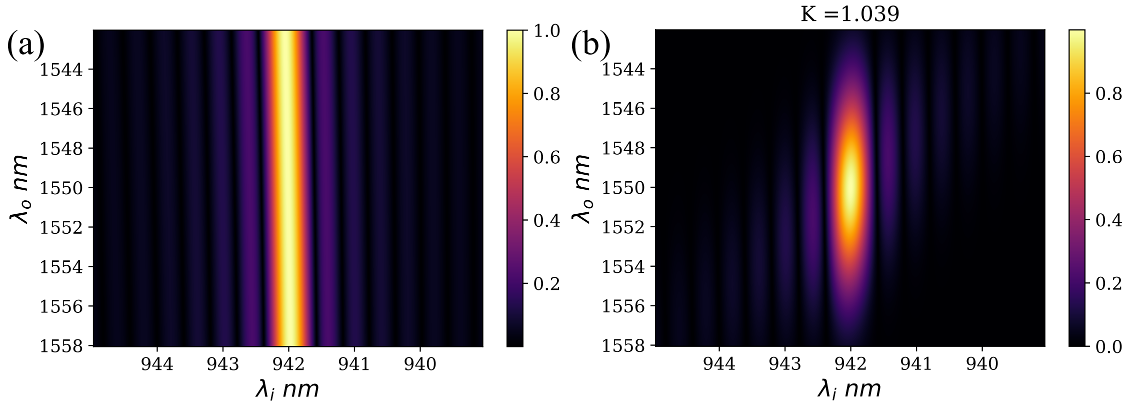

Figure 4.11: (a) PMF and (b) JSA for the LN used for the FC experiment in this thesis pumped with a 1 ps Gaussian pulse at 2400 nm. The axes are plotted in terms of wavelength for clarity. The Schmidt number $K = 1.039$ which indicates an almost single-mode process. The Schmidt number is increased from one due to the sinc lobes present on the positive diagonal. The intuition behind the FC process improving the spectral purity is that variation in the input frequency along the x-axis is mapped to the same output frequency on the y-axis axis.

arrival time of the converted light is locked to the arrival time of the pump pulse due to the matched group velocities, see Fig. 2.6.

This also highlights the potential drawback of pulsed frequency conversion, the lifetime of the QD is on the order of 1 ns i.e. the pump pulse cannot walk through the entire QD photon while it is inside the crystal. Another way to see this is the ideal mode to perfectly match the frequency conversion process is defined by the PMF bandwidth in Fig. 4.11, which is on the order of 100 GHz.

This bandwidth mismatch can be reduced by considering non-standard arrangements of the wavevectors in the FC process. The idea of counter-propagating signal and idler photons in PDC has been theoretically studied [114–116] and experimentally demonstrated [117, 118]. A similar idea has recently been discussed theoretically for FC [119]. We show that by considering this type of arrangement for FC the noise mitigating properties of the FC are greatly improved compared to the traditional arrangement of wavevectors.

### 4.5.6 Reverse wave frequency conversion

Consider again the Taylor expansion of the phase-mismatch introduced in Eq. (2.19) in terms of the input and output frequencies with the group velocities $v_j$ and the

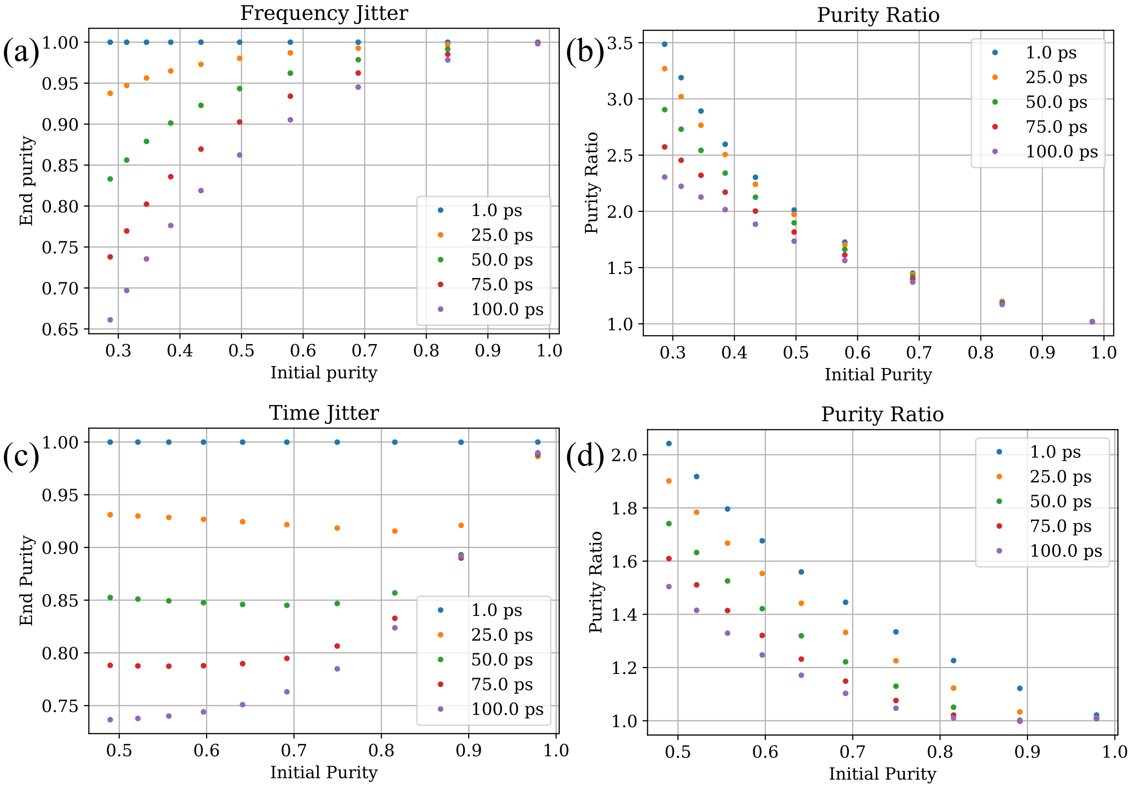

Figure 4.12: Numerical results on the purity of the frequency-converted photons as a function of the frequency jitter (a) and (b), and time jitter (c) and (d). The plots show the initial state purity on the x-axis and either the output state purity or the ratio of purity out/purity in on the y-axis. The pulse duration is varied from 1 ps up to 100 ps. In the limit of CW pumping the ratio of input and output purity is 1 as the state is left unchanged.

differences from the central frequencies $\Omega_j$. We had from equation Eq. (2.22) for a typical arrangement of the three fields $k_i \rightarrow k_p + k_o$,

$$\frac{\Omega_o}{\Omega_i} = \left( \frac{v_p^{-1} - v_i^{-1}}{v_p^{-1} - v_o^{-1}} \right), \tag{4.21}$$

which sets the gradient of contours in the JSA. If we consider the case where we reverse the direction of the input field, $-k_i \rightarrow k_p + k_o$, this changes the gradient to

$$\frac{\Omega_o}{\Omega_i} = \left( \frac{v_p^{-1} + v_i^{-1}}{v_p^{-1} - v_o^{-1}} \right). \tag{4.22}$$

The change in sign results in the large difference in the bandwidth in the PMF seen in Fig. 4.13. Physically what this describes is the case where the input photon travels in one direction and the pump and output photon travel in the opposing direction. We term this reverse-wave FC. This is subtly different from the case of

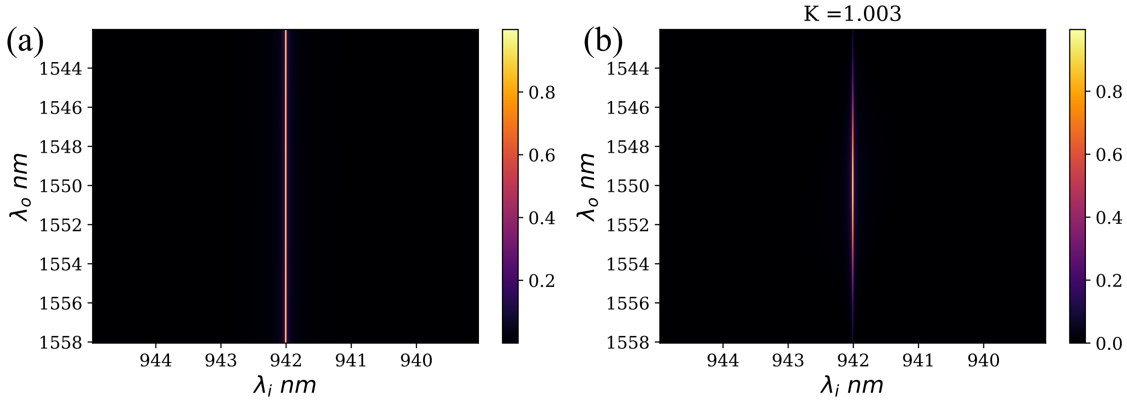

Figure 4.13: (a) PMF and (b) JSA for the reverse wave FC with a 10 mm crystal pumped with a 1 ps Gaussian pulse at 2400 nm. The axes are plotted in terms of wavelength for clarity. The plots use the same scale as the standard wavevector arrangement for comparison.

counter-propagating signal and idler which has been demonstrated experimentally. That scenario is the equivalent of the pump and output counter-propagating in the labelling used here for FC. To describe the interaction proposed here in the language of PDC it is equivalent to the signal and idler co-propagating but in the opposite direction to the pump pulse.

The main drawback of this technique is the large phase mismatch which must be compensated by the poling period of the crystal. Consider typically the phase-mismatch for the standard arrangement is given by $\Delta k = k_i - k_p - k_o = 2\pi/\Lambda$, this is now modified such that all terms are the same sign $\Delta k = -k_i - k_p - k_o = 2\pi/\Lambda$. For the wavelengths considered in this example with type-0 LN the required poling is 220 nm. While this sounds technically challenging it is within a factor of two of state-of-the-art demonstrations with KTP and LN. With this in mind the phasematching constraints could be satisfied with a higher-order phasematching at the cost of reduced efficiency, for quasi-phasematched process of order m the efficiency scales as $1/m^2$. As an example, fifth-order quasi-phasematching would require poling periods of around 1.1 $\mu$m which is commerically available in KTP and LN.

The reverse-wave case has higher purities for all values of noise. The FC process can use longer pulse durations which may be experimentally easier to realise and still remove spectral and temporal jitter. For pump durations of 100 ps the output

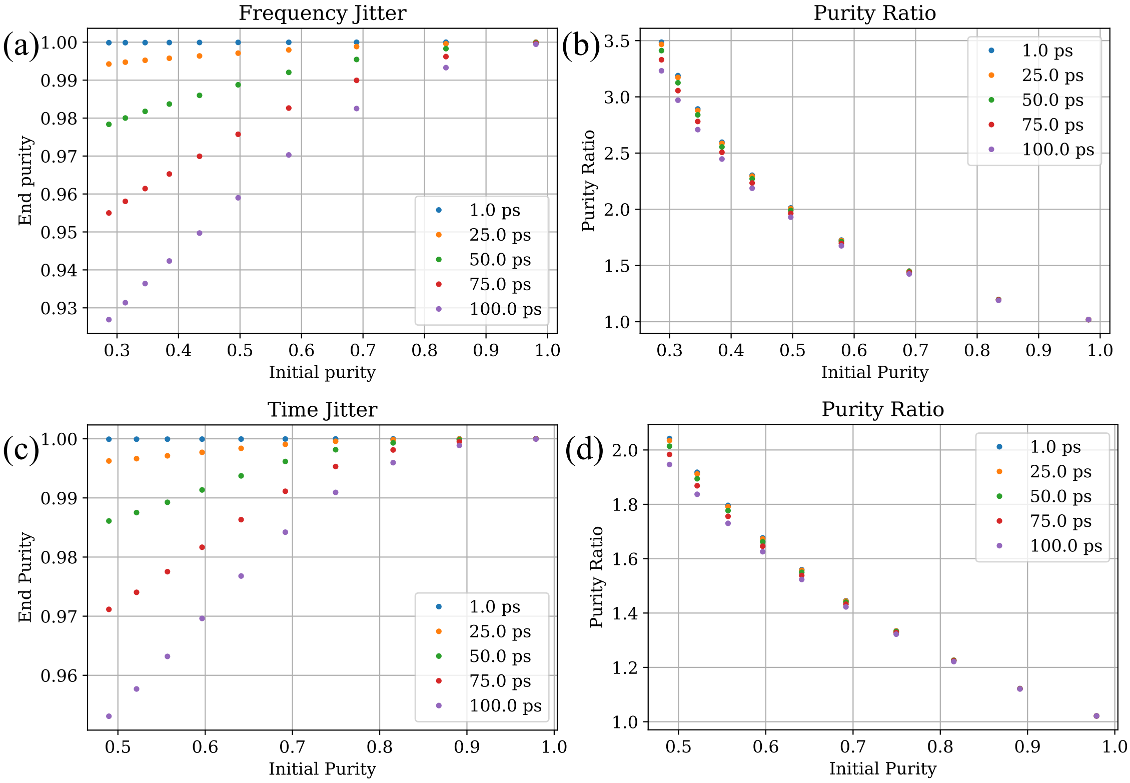

Figure 4.14: Numerical results on the purity of the frequency-converted photons as a function of the frequency jitter (a) and (b), and time jitter (c) and (d) for the reverse wave FC process proposed. As with Fig. 4.12 the plots show the initial state purity on the x-axis and either the output state purity or the ratio of purity out/purity in on the y-axis. The pulse duration is varied from 1 ps up to 100 ps. In the limit of CW pumping the ratio of input and output purity is 1 as the state is left unchanged.

purity is above 90% for all values of noise considered.

A second potential application is the idea of spectral compression with this reverse wave FC process. Instead of considering the downconversion of a NIR photon to telecom wavelength, consider the upconversion procsess. The broadband 1550 nm photon is spectrally compressed when upconverted to 942 nm. Broadly speaking quantum memories operate at shorter wavelengths than 1550 nm and have linewidths much narrower than the ≈ 100 GHz of photons from typical PDC sources. This then motivates upconversion with spectral compression as potentially enabling integration with quantum memories. Comparing the bandwidth of the first pair of Schmidt modes the bandwidth ratio is 130:1. The 1 ps duration 1550 nm photon can be upconverted to 942 nm with a bandwidth compression down to 3.4 GHz. For the standard arrangement the compression is 6.58 and the NIR bandwidth is 68 GHz.

Pulse compression using a standard group-velocity matched FC process has been demonstrated [120] with PDC photons upconverted from 1545 nm to 550 nm with a compression of 7.5. Compression by a factor of 40 has been demonstrated in sum-frequency generation by chirping the single photon input at 800 nm and pulse pump at 800 nm with equal magnitude but opposing signs [121]. The reverse wave conversion process compares favourably in terms of the compression available and is also completely passive without requiring the input photon to be chirped. The price you pay for this passive compression is the technical challenge of poling a crystal with a period less than 1$\mu$m.

Note the bandwidth of the telecom photon could be larger and still be converted down to 3.4 GHz using a shorter pulse at 2400 nm, this would extend the JSA along the y-axis in Fig. 4.13, but the final bandwidth is still set by the PMF bandwidth of 3.4 GHz.

To compress a pulse below 1 GHz the length of the crystal must be increased (10 mm considered for these simulations) or using a cavity assisted process where the cavity mirrors are AR-coated at 1550 nm and 2400 nm but highly reflective at 940 nm.

Similar compression results can be achieved for other technologically relevant wavelengths, converting a 1550 nm photon to 780 nm to interface with a rubidium quantum memory the compressed bandwidth is again 3.4 GHz which is too broad to directly interface with the memory but might reduce the number of photons lost to tight spectral filtering.

While optimum compression is achieved when the output and pump group velocities are matched which can be seen by looking at the denominator of Eq. (4.22), some spectral compression can be achieved when this is not the case. Consider 422 nm, the wavelength of the strontium ions recently used to demonstrate device-independent quantum key distribution [122]. The spectral compression is 25:1, which may still be useful for interfacing different quantum systems with different photon bandwidths.

Having discussed how pulsed FC can be used to improve the coherence of single photons emitted by a QD we return back to the experimentally demonstrated work presented at the beginning of this chapter. We have realised a bright source of single photons at 1550 nm with relatively low multiphoton noise, the clear next step is to send the photons over some fibre and attempt to carry out a quantum key distribution protocol. This will be the focus of the next chapter.

# Chapter 5

# Quantum key distribution with a frequency-converted quantum dot

Quantum communication is among the most mature quantum technologies with some practical demonstrations outside the laboratory setting. This is in part due to the relatively simplicity of the physical requirements compared to tasks like computation. Quantum communication is uniquely suited to photonics, as the only flying qubit photons are the sole option for encoding information. Of the various quantum communication tasks quantum key distribution is arguably the most well studied and well demonstrated experimentally. There are even commercially available systems for the paranoid [1]. Plainly put QKD allows two users, Alice and Bob in the common setting, to generate a shared cryptographic key which is not known to a third party Eve. QKD in the ideal setting, ignoring issues with experimental implementation, is information-theoretically secure. This is in contrast to classical cryptographic methods such as Rivest–Shamir–Adleman (RSA) which are typically based on the "hardness" of a particular mathematical problem. With the belief that one day we will have large-scale fault tolerant quantum computers and with algorithms such as Shor's algorithm for prime factorisation [123] these classical cryptographic methods are susceptible to attack from an adversary armed with a quantum computer.

Broadly speaking QKD protocols can be divided into two groups, entanglement-based or prepare-and-measure schemes. The security of both types is backed by fundamental properties of quantum mechanics, the monogamy of entanglement for entanglement-based schemes, the property that a maximally entangled state of $n-$particles cannot be an entangled state of $n+1$ particles. For prepare-and-measure schemes the critical property is the incompatiblility of mutually unbiased bases; for a state prepared in the eigenbasis of one observable, measurement outcomes in a complementary observable are random.

---

[1] https://www.idquantique.com/

There is a complete zoo of QKD protocols. The earliest proposed protocols rely on trust in the experimental apparatus such as the sources or detectors. More sophisticated protocols relax some of these requirements such as measurement-device-independent QKD [124] which introduces a third party Charlie who operates the measurement apparatus, and allows the trust in the measurement apparatus to be removed. This can be extended to fully device-independent QKD [125] where Alice and Bob trust none of the experimental apparatus to operate faithfully, including the photon sources in their own labs. Typically, the cost of removing trust in some part of the QKD apparatus is a smaller secret key rate and reduced tolerance to loss.

In this chapter we will focus on the original QKD BB84 protocol [126], where Alice prepares states in two MUBs which are then sent to Bob over a channel who randomly measures in the same pair of bases. This protocol has the simplest experimental requirements: Alice maintains a single-photon source and a method to encode in a particular photonic DoF with Bob owning the receiver which consists of four detectors, one for each of the states in the pair of MUBs.

As the QD source demonstrated in Chapter 4 is converted to 1550 nm this opens up fibre optic cable as a viable channel between Alice and Bob. Optical fibre is the ideal channel for metropolitan or inter-city scale distances, allowing connections between points without line-of-sight connections unlike free-space links. For connections on the order of hundreds of kilometres the losses in fibre are manageable ($< 40\,$dB for 200 km). Beyond 1000 km satellite-based QKD may become preferred for point-to-point QKD where the losses are not due to propagation but are geometric losses due to finite apertures of the collection optics.

## 5.1 Brief overview of the BB84 protocol

In the following section I will briefly outline the BB84 protocol for polarisation encoding in the ideal experimental setting,

- Alice and Bob initially authenticate their identities over a classical channel with some pre-shared random bits.
- Alice encodes single photons randomly in one of the two bases, we will use the linear (Pauli Z) and diagonal (Pauli X) bases for concreteness. One of the bases is used for key generation and the other is used for parameter estimation in the post-processing step. We will follow the convention that the Z basis is used for key generation and X is used for parameter estimation.
- Bob randomly measures in one of the two bases.
- Alice and Bob announce publicly their respective basis choice and discard all rounds where they measure in a different basis. This is referred to as key sifting.
- Of these rounds where Alice and Bob measure in the same basis (Z for example), a subset is used to detect the presence of an eavesdropper typically referred to as Eve. If Eve tries to measure the photon in the opposing basis to the one Alice encoded in (X in this case), Bob will detect errors in his measurement outcomes.
- If the error rate is above a particular threshold the protocol is aborted.
- If error rate is acceptable Alice and Bob perform error correction to remove potential errors in the key and privacy amplification to increase the secrecy of the key. Both of these steps reduce the overall length of the key generated.
- They now share a private and secure key which can be used to encode a message between both parties.

## 5.2 Key rate for a noisy single-photon source

This ideal scenario requires an ideal single-photon source, which emits exactly one photon with 100% efficiency every round. This is currently far from reality with current single-photon sources which are lossy and have multiphoton noise which can be exploited by Eve in the photon-number splitting attack. In this attack Eve splits the incoming pulse and stores one part in a quantum memory and sends the other part on to Bob. When Alice and Bob announce their random basis selection for each round Eve measures in the correct basis and therefore has perfect knowledge of the key. This potential security loophole can be mitigated by the decoy-state method which will be discussed in more detail in Section 5.5. If the decoy-state method is not used the multiphoton terms must be incorporated directly into the security analysis. This analysis for realistic devices was carried out by Gottesmann, Lo, Lutkenhaus and Preskill [127]. The secret key rate in the asymptotic regime, assuming an infinite number of rounds, can be written as

$$S = p_{\text{sift}} p_{\text{click}} \left[ A \left( 1 - H \left( \frac{e_p}{A} \right) \right) - f \left( e_b \right) H \left( e_b \right) \right], \tag{5.1}$$

where $S$ is the probability that a given round contributes a bit to the final key, $H(e) = -e \log_2(e) + (1-e) \log_2(1-e)$ is the binary Shannon entropy. $p_{\text{click}}$ is the probability that Bob's detectors click in a given round which can be approximated as $p_{click} \approx \bar{n}T + d$, where $\bar{n}$ is the mean photon number injected into the communication channel, $T$ is the channel transmission and $d$ is the probability a detector fires due to a dark count. $p_{sift}$ is the probability that Bob measures in the key generation basis, in the asymptotic limit Alice sends key generation encoded photons with probability approaching one. The key rate per second is then determined by multiplying the probability a given round contributes a bit (bit per pulse) by the repetition rate of the source.

$A = (p_{\text{click}} - p_m) / p_{\text{click}}$ is the fraction of signals due to single-photon pulses with $p_m$ the probability that Alice sends a pulse which contains more than one photon. $H(e_p/A)$ is the fraction which must be discarded for privacy amplification, with $e_p$

the phase error or error in the basis used for parameter estimation. An important point is that the factor $A$ decreases with increasing loss as $p_{\text{click}}$ decreases proportional to the channel loss but $p_m$ is constant. For a particular loss, $p_{\text{click}} \approx p_m$, the probability on a given round that Bob's detectors fire is about the same probability that Alice emitted a multiphoton pulse. At this point one must make the pessimistic assumption that *all* of Bob's clicks are due to multiphoton pulses from Alice. Eve can have perfect knowledge of these bits using the photon-number splitting attack and so the protocol must end. This is why the factor $A$ appears in the denominator of the privacy amplification fraction.

The factor $f\left(e_b\right) H\left(e_b\right)$ is the fraction of rounds which must be discarded in order to error correct the raw string of bits, $e_b$ is the error rate in the key generation basis and $f\left(e\right) > 1$ is the error correction efficiency. Ideally, $f\left(e\right) = 1$, which is the information-theoretic optimum for correcting a bit string (the Shannon limit), However, in practice $f\left(e\right) = 1$, even for the best error correcting algorithms. Hence, the number of bits that need to be discarded following the error correction process is always higher than just the number of erroneous bits. For this thesis the error correction efficiency is interpolated between the values presented in [128].

It is worth highlighting the impact of multiphoton noise on the key rate with a noisy single-photon source. The important factor to consider is the single-photon fraction $A$. Not only is the source term in Eq. (5.1) $p_{\text{click}}$ scaled by the single-photon fraction, the amount of key removed for privacy amplification scales strongly as the single-photon fraction decreases.

The central issue then is estimating the multiphoton probability $p_m$ for real experimental sources. Luckily, the second order correlation $g^{(2)}$ can be used to provide an upper bound to $p_m$ which is experimentally accessible and robust to detector inefficiency and loss [129]. Using the approach of [130] the multiphoton emission

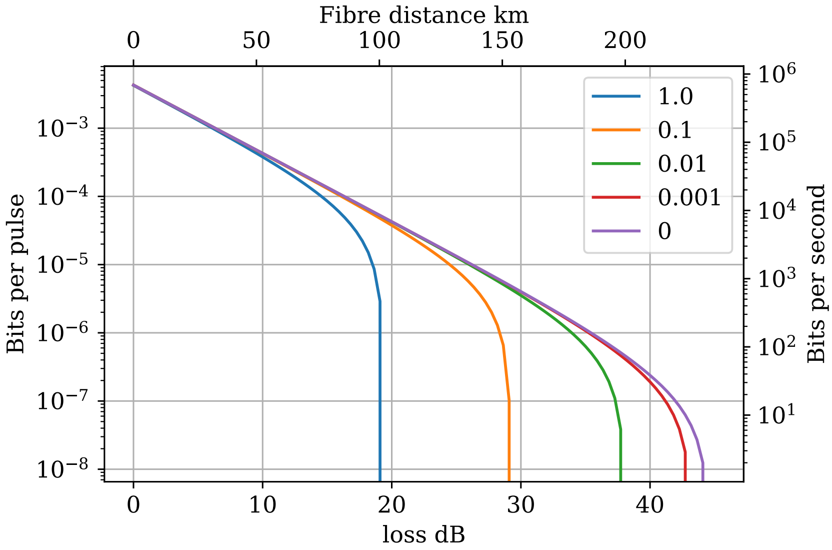

Figure 5.1: Comparison of the secure key rate for different photon sources with all parameters left identical except for the $g^{(2)}$ which varies from $g^{(2)} = 1$ for a weak coherent source to $g^{(2)} = 0$ for an ideal single-photon source. The brightness of the source $\bar{n} = 0.01$ and error rates are fixed between each curve. The repetition rate is set to 160 MHz and the fibre loss is set to 0.19 dB/km to match the experimental parameters from Section 5.3.

probability can be upper-bounded by the $g^{(2)}$ in the following way,

$$\begin{aligned} g^{(2)} &= \frac{\langle \hat{n}\left(\hat{n}-1\right)\rangle}{\bar{n}^2} \\ &= \frac{\sum_{i=2}^{\infty} i\left(i-1\right)p_i}{\bar{n}^2} \geq \frac{\sum_{i=2}^{\infty} 2p_i}{\bar{n}^2}, \end{aligned} \tag{5.2}$$

where we have used the fact that $i\left(i-1\right) \geq 2$ for $i \geq 2$. The vacuum and single-photon terms are removed from the summation by the $i$ and $(i-1)$ factors respectively. From this then one can write,

$$\begin{aligned} g^{(2)} &\geq \frac{2p_m}{\bar{n}^2} \\ p_m &\leq \frac{g^{(2)}\bar{n}^2}{2}, \end{aligned} \tag{5.3}$$

where the definition $\sum_{i=2}^{\infty} p_i := p_m$ has been made. The curves in Fig. 5.1 show the same source for different values of $g^{(2)}$. At short distances the key rates are all similar regardless of the multiphoton emission probability but the maximum tolerable loss is restricted to less than 20 dB for a weak coherent pulse where $g^{(2)} = 1$ compared to over 40 dB for an ideal single photon source with $g^{(2)} = 0$.

It is worth noting that counter-intuitively, Alice can extend the maximum tolerable loss by adding additional attenuation to the source before injecting pulses into the communication channel. Adding an additional attenuation factor $\eta$ before sending photons to Bob changes the click probability and the multiphoton fraction in the folliowing way,

$$\begin{aligned} p_{\text{click}} &= \bar{n}T + d \rightarrow \bar{n}\eta T + d \\ p_m &= \frac{g^{(2)}\bar{n}^2}{2} \rightarrow \frac{g^{(2)}\bar{n}^2\eta^2}{2}. \end{aligned} \tag{5.4}$$

The click probability decreases linearly as Alice adds loss to her source but the multiphoton probability decreases quadratically. In the scenario where the key rate is limited by $A \rightarrow 0$ the maximum tolerable loss can be extended by adding additional loss before the communication channel. While increasing the maximum distance, adding additional loss reduces the key rate at short distances. The ideal solution is for Alice to optimise the attenuation added to her source for the loss of the communication channel value.

At this point it is worth making a detour to consider why we should bother with noisy single-photon sources for QKD applications. The decoy state method works well, it is experimentally simple compared to most single-photon sources and has been shown to work for over 400 km in optical fibre [131]. This is a valid question and one the author of this thesis has argued on both sides of throughout the course of this work. If a quantum network infrastructure containing quantum repeaters exists in the future, the memories in these repeaters are designed to operate with true single photons. If we are going to incorporate these types of sources in a network in the future we should also consider their applications in QKD as a corollary. Another more aspirational reason is that if ideal single photons are going to be developed for other applications such as optical quantum computing, then these sources could also be leveraged for QKD. In the limit of an ideal single-photon source $\bar{n} = 1$ and $g^{(2)} = 0$ such a source can be competitive and exceed the rates and distances available with decoy states which reduces the bandwidth of the channel by interleaving decoy states with real signal states. From a security point of view the additional complexity of the decoy-state method which may introduce additional side-channels due to experimental implementations deviating from the ideal theoretical performance. We will return to this point in Section 5.5.

At this point we dive into the experimental work towards a demonstration of QKD with our frequency-converted QD source. This work is not a true faithful implementation of the BB84 protocol as it is missing some key steps. The state Alice encodes is not changed on a round-by-round basis. Slow motorised waveplates are used to change the state which are not compatible with the 160 MHz repetition rate of the source. A fast electro-optic modulator can be used to change the polarisation state on a shot-by-shot basis. A GHz rate electro-optic modulator (iXblue PSW-LN-10) was purchased for this experiment but unfortunately it was unusable due to the spectral fluctuations in the seed laser used in the FC process increasing the polarisation encoding error. More details on this can be found in Appendix B. The fibres used in the demonstration which connect the source and receiver are also in the lab. This is a controlled environment which is quite different to deployed optical fibre in a real communication network which might require active polarisation stabilisation over the course of key distribution. Despite this the *expected* performance in a deployed setting can be predicted from this type of “in-lab” demonstration which is common with noisy single-photon sources [90, 91, 132–135] . An extensive review of this type of “in-lab” demonstration of QKD with QDs can be found in [136].

## 5.3 Experimental Results

The experimental setup for the QKD demonstration consists of three distinct parts: Alice’s source, the communication channel which in this case is optical fibre and Bob’s polarisation receiver module. The source is similar to the frequency converted source setup in Fig. 4.7 with one change being the repetition rate has been temporally multiplexed up to 160 MHz in a similar fashion to the 8b-KTP source

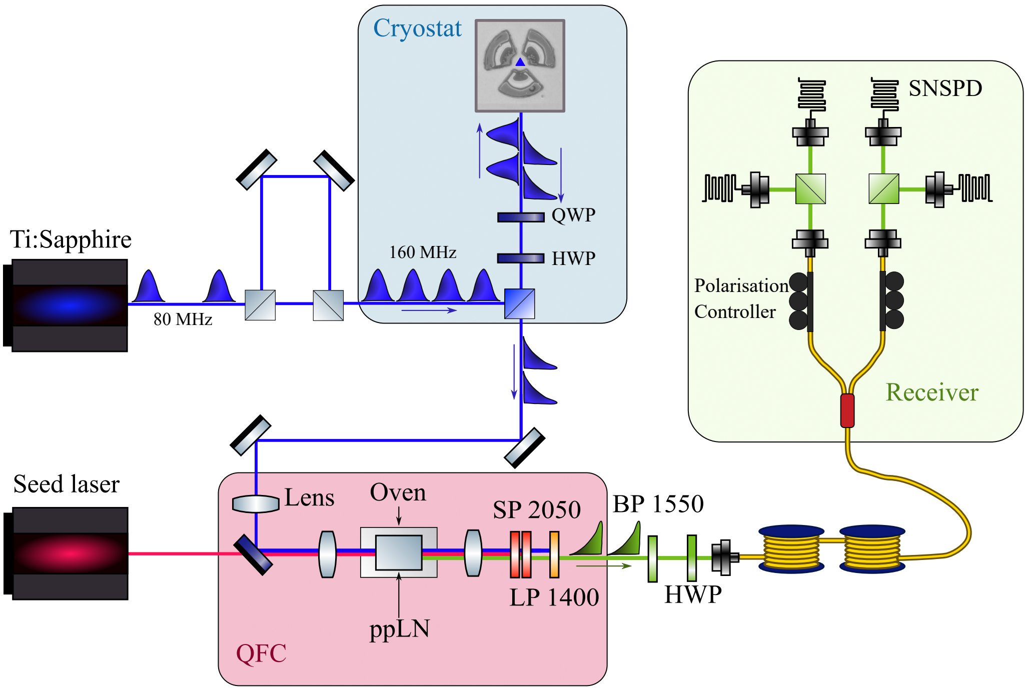

Figure 5.2: Experimental layout of the QD source (blue shaded region), the quantum frequency conversion setup (pink shaded region) and passive BB84 receiver (green shaded region). The 80 MHz pulse train from the Ti:Sapphire laser is temporally multiplexed up to 160 MHz using a free-space delay-line matched to half the pulse separation of 12 ns. The frequency-conversion setup is identical to the description in the previous chapter. The combination of the QD source and the frequency-conversion setup constitute Alice's source in the classic BB84 scenario. The transmission channel consists of spools of fibre of various length which are connected using physical contact fibre connectors to make up the distances measured in Fig. 5.5. Bob's receiver passively chooses between X and Z basis measurements using a 50/50 fibre beam splitter. This sets the sifting fraction to $p_{sift} = 1/2$. Projections are made using polarising beam splitter cubes and in-fibre polarisation controllers to align the measurement basis.

in Section 3.5. This improves the overall key rate by a factor of two but does not improve the probability of each pulse producing a secure bit as error rates and the single-photon fraction are evaluated on a per-pulse basis. The $g^{(2)} = 0.036$ of the source was also improved compared to the measured values for off-resonant excitation after conversion presented in Section 4.4. This was due to optimisation of the excitation frequency and improved suppression of reflected laser light from the third cavity mode of the QD.

The encoded state is controlled by a single motorised HWP placed before the collection fibre in Alice's source to encode $\{H, V, D, A\}$ polarisation states and sent down the fibre channel. Bob's receiver is aligned to these four states at the start of the integration time using in-fibre polarisation controllers. Counts are monitored for each state for 30 mins. The long fibres which act as a communication channel are housed in an insulating box to minimise fluctuations in the polarisation state over the course of the measurement. These fluctuations are stable over at least the 30 min integration time, an example time trace of the encoded error is shown in Fig. 5.3.

For each fibre distance 30 minutes is long enough to accumulate at least $5 \times 10^6$ counts which is sufficient to accurately estimate the errors and click probabilities and then estimate what the key rate would be. This number of raw bits would not be enough to generate a secure key in the finite key regime which is discussed in Section 5.4.

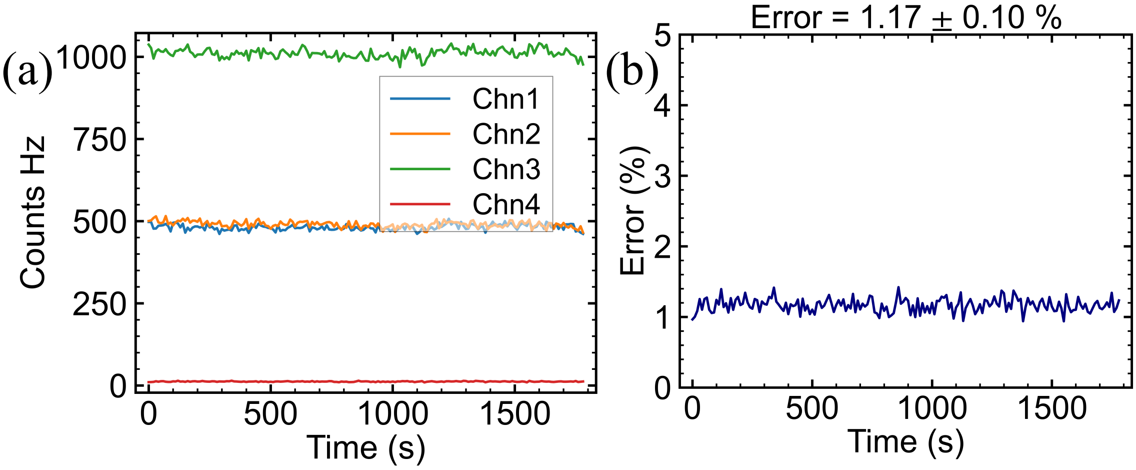

Figure 5.3: Time trace of the recorded counts over 30 minutes of measurement with the encoding error. Subfigure (a) shows the timetrace of the counts arriving on each of the four detectors in Bob's receiver over 30 mins of integration. The error rate shown in (b) which is the ratio of the orange to blue line is essentially constant over the 30 mins integration time. This data set is from a measurement at 150 km which is the largest distance which had a positive key rate. The green and red curves correspond to projections on the complementary basis to the encoded basis.

After frequency conversion and filtering the detected count rate at 0 km is 1.6 MHz, which gives a mean photon number of $\bar{n} = 0.0142$ backing out the known receiver transmission (87%) and the estimated quantum efficiency of the detectors ($\approx 75\%$). The breakdown of how these values are reached is summarised in Table 5.1. This mean photon number at the end of Alice's setup is the critical value for the security analysis as it determines the multiphoton probability along with the $g^{(2)}$ at the initial point where Eve can in principle perform a photon-number splitting attack.

| Projection | Coupling % | Relative Efficiency % | DCR Hz | Total Efficiency % |
|---|---|---|---|---|
| V | 94.2 | 93.4 | 13 | 87.98 |
| H | 88.4 | 95.2 | 13 | 84.16 |
| D | 90.3 | 98.3 | 10 | 88.76 |
| A | 87.6 | 100 | 10 | 87.6 |

Table 5.1: Summary of the losses and efficiencies for Bob's receiver. The coupling losses are characterised with a 1550 nm diode laser and a power meter. The relative efficiency of the four detectors are measured using a PDC source sending the idler photon to a 5th detector and sending the signal photon to each of the detectors in turn and measuring the heralding efficiency. The detectors were chosen for having the lowest dark-count rate of the detectors available. The total efficiency is the product of the coupling and relative efficiencies. There is an unknown factor of the absolute efficiency of the detectors. This is estimated to be around 75% based on the manufacturer's characterisation.

The error due to polarisation leakage and polarisation controller misalignment is found to be $e_p = 0.3\%$ by fitting the measured error rate with

$$e_{b/p} = \frac{p_d/2 + e_p \bar{n} T}{p_d + \bar{n} T}, \tag{5.5}$$

where $T$ is the transmission of the channel and $p_d$ is the dark count probability. The dark-count probability is set as $p_d = 1.47 \times 10^{-7}$. This is the product of the average time-gate used in the experiment of 3.1 ns and the average dark count rate of 11.5 Hz.

At this point it is worth comparing this demonstration with similar works with other types of single photon-emitter based on QDs, molecules and defects in two-dimensional materials. This comparison is made in Table 5.2. Due to the high intrinsic brightness of the QD, the efficiency of the frequency conversion and collection, and the low multiphoton noise, the key rate at short distance is significantly higher and the maximum tolerable loss is around 5 dB higher than previous work, see Table 5.2. As this source is at 1550 nm the physical distance over which a key can be generated is significantly further than the sources operating in the O-band around 1300 nm or in the NIR around 800 nm. It should be said that there are other sources which could be frequency converted [13] or have been used with frequency conversion [93, 94], that would outperform the current work but these have so far

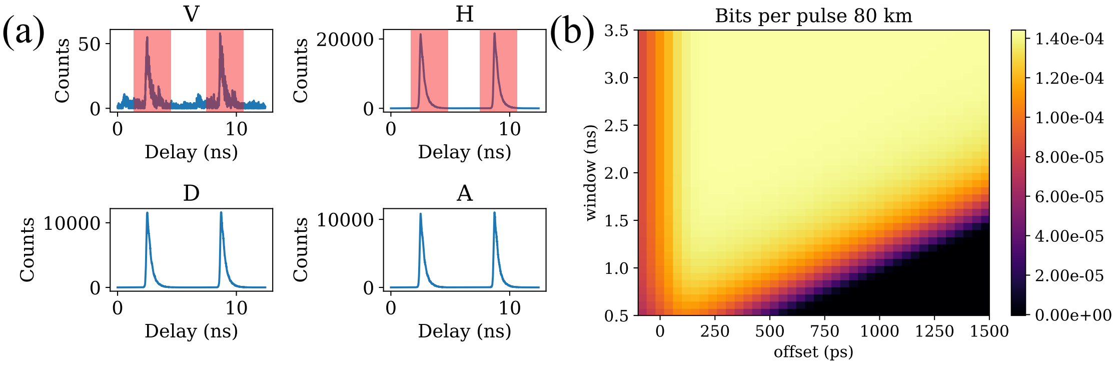

Figure 5.4: Typical data set for encoding H over 80 km of fibre and the effect of time gating on the number of bits generated per pulse. (a) The counts on each detector are histogrammed over a 30 minute integration time relative to a clock signal derived from the Ti:Sapphire laser at 80 MHz which results in two pulses per clock cycle. The counts are time gated with respect to the clock signal and the width and position i.e. the offset relative to the peak of each histogram, is varied to optimise the total key rate (b). The maximum probability of generating a bit per pulse is then used as the value shown in Fig. 5.5. The data shown in this plot is for preparing and sending horizontally polarised photons and sent over 80 km of fibre.

not been used in a QKD demonstration.

| Reference | AKR at 0 km (kbps) | Maximum loss (dB) |
|---|---|---|
| This work | 689 | 33.3 |
| This work with active encoding* | 298 | 34.4 |
| QD [91] | 4 | 23 |
| QD [132] | 2 | 23 |
| Molecule [135] | 500 | 22 |
| 2D Material [137] | 0.24 | 21 |
| 2D Material [138] | 150 | 23 |
| [134] | 25 | 28 |

Table 5.2: Comparison of other QKD demonstrations based on single-photon emitters. *Prediction based on 3 dB loss and 2% polarisation encoding error typical with fibre-based electro-optic modulators. Reference [91, 137] includes active switching of the encoded state, all other demonstrations use static encoding in a similar spirit to this work.

Comparing the asymptotic key rate is the cleanest way to compare the performance of different sources as the key rate has relatively few free parameters. Arguably a more relevant metric is the key rate in the finite regime where the number of key exchange rounds is no longer considered infinite. This is the realistic scenario if a QKD system was used in practice. The experimental parameters used to evaluate the key rate must be estimated from a finite sample size of the data and are therefore not known perfectly. This must be taken into account to guarantee the information

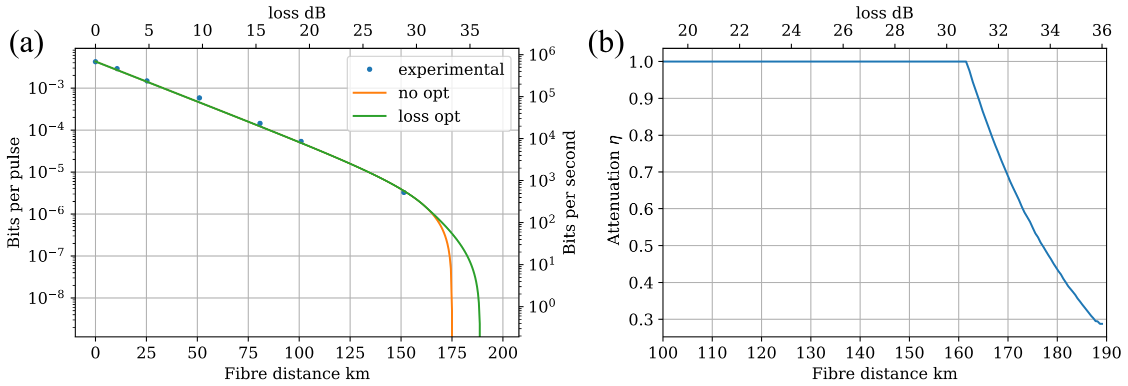

Figure 5.5: The theoretical asymptotic key rate based on the measured experimental parameters alongside the experimentally measured counts. (a) Comparison of the measured key rate in the asymptotic regime (blue dots) from processing the experimentally measured count rates and the theoretical key rate based on the experimental parameters (solid orange line) with and without without additional attenuation. The green line shows the maximum key rate optimising Alice's pre-attenuation which adds an additional 2.6 dB of tolerable loss. The theoretical prediction comes from Eq. (5.1). (b) The variation of the additional pre-attenuation, plotted as transmission) Alice adds to her source before injecting into the fibre with distance. No pre-attenuation is needed until the “shoulder” of the key rate plot where the key starts to drop off sharply.

theoretic security of the key produced. The next section will focus on estimating the finite key rate for the measured experimental parameters.

## 5.4 Finite key rate

The key rate presented in the previous section assumed an infinite number of rounds between Alice and Bob a highly idealised scenario. In a realistic setting Alice and Bob can only exchange a finite number of rounds, at this point the fraction of signals which contain a single photon and the error rates must be estimated from the observed counts taking into account statistical fluctuations which assume the most pessimistic case. The finite key rate for a noisy single-photon source is developed following the approach of [139]. This is the common reference used within the community of people working on single-photon emitters although is perhaps dated compared to more modern security analysis which has been developed for decoy-states [2].

---

[2] An updated finite key analysis using more modern approaches is being developed with collaborators at the time of writing this thesis.

There are essentially two different ways of presenting the finite key rate in the finite key regime. One approach is to fix the block size, i.e. the number of raw bits generated, and consider how the key rate changes as a function of block size. This essentially lets the integration time vary when presenting the key rate as a function of distance. The time required to generate a fixed number of bits is different at 0 dB loss compared to 30 dB where a large fraction of the signals are lost in transit. This approach is more common with theoretical work on finite key rates in QKD.

The second approach is to fix the integration time, with this approach the block size decreases with distance as fewer signals make it to the receiver in the fixed integration window. This is the approach which is used in the rest of this chapter as it is more intuitive from an experimentalist point of view. It is also arguably a more practical approach for future quantum networks where multiple users may only have a finite amount of integration time to generate a key with a shared quantum resource.

The probability a given pulse generates a bit in the finite key regime is given by,

$$\begin{aligned} S = \frac{p_{\text{click}}}{2}\frac{n}{m+n}\Bigg[\tilde{A}\left(1-H\left(\frac{\tilde{e}}{\tilde{A}}\right)\right) - f\left(e\right)H\left(e\right) \\ -7\sqrt{\frac{\log_2\left(\frac{2}{\bar{\epsilon}}\right)}{n}} - \frac{2}{n}\log_2\left(\frac{1}{\epsilon_{\text{PA}}}\right) - \frac{1}{n}\log_2\left(\frac{2}{\epsilon_{\text{EC}}}\right)\Bigg]. \end{aligned} \tag{5.6}$$

Eq. (5.6) is quite involved so a little bit of time will be spent unpacking what is meant by each of the terms. In the finite key regime a total number of $N$ bits are generated where a fraction of bits $n$ is used for key generation and $m$ is used for parameter estimation. The prefactor $n/(n+m)$ then is the fraction of signals Alice sends in the key generation basis compared to the parameter estimation basis. This is missing in the asymptotic regime where the fraction approaches one. The sifting fraction is set to 1/2 to match the asymptotic data presented previously. In a real implementation this parameter should be optimised over for a given distance and integration time taking into account the expected error rates. The final three terms are purely due to finite size effects: $\bar{\epsilon}, \epsilon_{\mathrm{PA}}, \epsilon_{\mathrm{EC}}$ can be roughly interpreted as the failure probabilities for entropy smoothing, privacy amplification and error correction respectively. In the modelling presented here these are all set to $10^{-10}$. The error rate and single-photon fraction must be estimated from the raw detected events which is denoted with a tilde.

The finite size correction is of the form [139],

$$\xi\left(N, \varepsilon_{\mathrm{PE}}\right) = \left[\frac{2\log_2\left(\frac{1}{\varepsilon_{\mathrm{PE}}}\right) + 2\log_2\left(N+1\right)}{N}\right]^{1/2}, \tag{5.7}$$

with $\varepsilon_{\mathrm{PE}}$ the failure probability for parameter estimation. With this, the new finite key version of the error and single photon fraction are,

$$\begin{aligned} \tilde{A} &= \frac{p_{\mathrm{click}} - p_m - \xi(N)}{p_{\mathrm{click}}} = A - \frac{\xi(N)}{p_{\mathrm{click}}} \\ \tilde{e} &= e + \xi\left(m\right). \end{aligned} \tag{5.8}$$

These estimates come from the fact that the error rate must be estimated from $m$ rounds and the single photon fraction must be estimated from the total number of observed clicks N. [3]

The fraction of the key which must be removed for privacy amplification $\left(1 - H\left(\frac{\tilde{e}}{\tilde{A}}\right)\right)$ is hit by two finite corrections as both the error rate and the single photon fraction are estimated quantities.

The finite key rate is presented in Fig. 5.6 for illustrative integration times, the key generation fraction Alice sends is numerically optimised for each distance and integration time.

The general picture for Fig. 5.6 is quite bleak. Even with an entire year of integration time the maximum tolerable loss is considerably smaller than the asymptotic distance. Over shorter distance reasonably key rates are achievable. For practical acquisition times of one hour a key rate of 31 kbps can be generated over 50 km of

---

[3] This second point has been repeatedly overlooked by the QD community when calculating the finite key rate [90, 132, 133], even when citing and using the same formalism as [139].

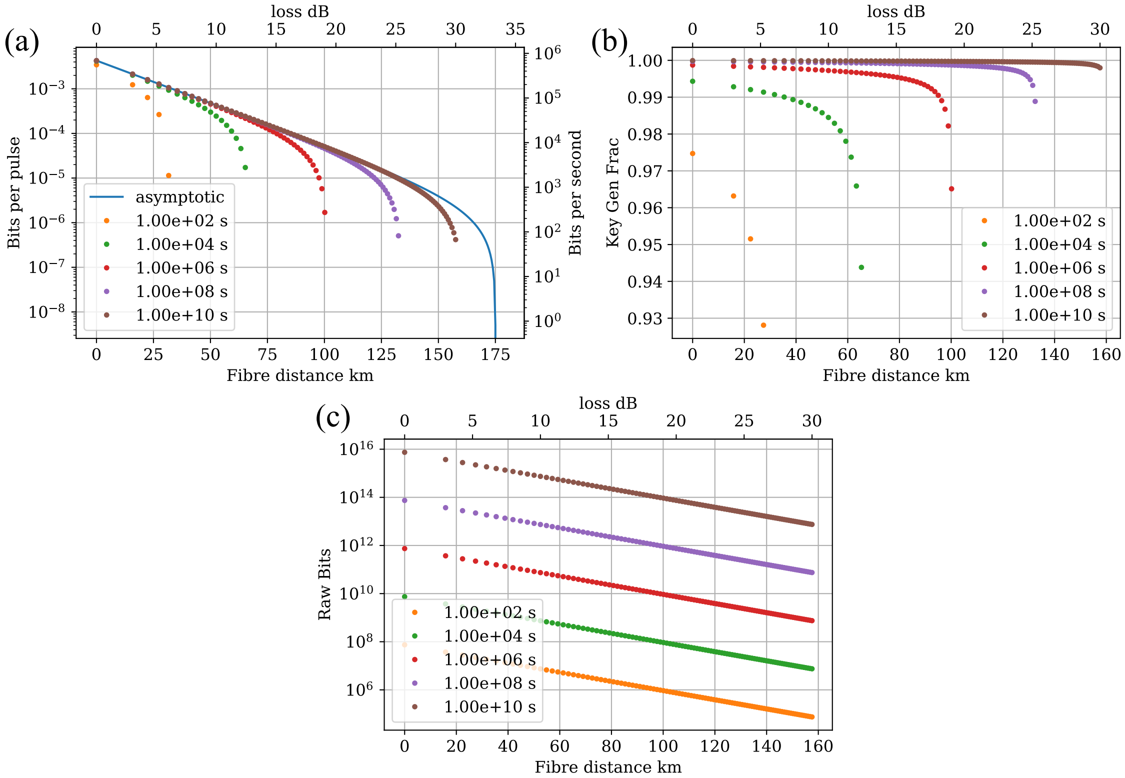

Figure 5.6: The finite key rate, key generation fraction and number of raw bits generated for a variety of integration times. (a) Comparison of the finite key rate. The optimised key generation fraction is shown in (b) which is above 90% for all distances. The data is cut off before the fraction of signals in the key generation basis approaches zero as the key rate approaches zero. (c) Shows the number of raw bits generated for each distance and time to allow comparison with fixed block size work.

fibre.

From the analysis presented to this point it is quite clear that multiphoton noise is a fatal problem for QDs when it comes to practical QKD implementation, the photon-number splitting attack is a potent tool that Eve can use to gain information on the secret key. The decoy state method was developed as an effective counter to this attack and this is where we head in the next session.

## 5.5 Extending the range with decoy states

Up to this point the decoy-state method and using a single-photon source have been presented as separate approaches to QKD. In the limit of a noiseless single-photon source the decoy-state method is redundant, but with multiphoton noise the decoy-state method can be used in tandem with a single-photon source. This idea has been suggested in the literature [140], the analysis here was developed independently of this work and goes much deeper into the implementation of the decoy-state protocol than the existing literature.

The decoy-state method was introduced in [141] with a heuristic argument and put on more sure footing in [142] which also contains an excellent comparison to the GLLP (named after Gottesman, Lo, Lutkenhaus and Preskill)which is the security analysis used previously for a noisy single-photons source. Some of the nomenclature and a brief sketch of how the decoy-state method works will be presented here with the application of the decoy-state method to a noisy single-photon source later in this chapter.

In the decoy-state method Alice randomly replaces some of the signal states with so-called decoy states with different mean photon number to the signal state. At the end of the protocol when Alice and Bob reveal their respective basis choice in the basis reconciliation step Alice also reveals which type of pulse she sent, either a signal or decoy. As these pulses have different intensities they should have different probabilities of generating a click at Bob's detectors. By monitoring these click probabilities for each pulse type Alice and Bob can detect if Eve is implementing a photon-number splitting attack on the channel.

Let us define the yield $Y_{i|\mu}$, which is the probability a pulse containing $i$ photons reaches the end of the communication channel and sets off Bob's detector given that Alice chose the pulse distribution $\mu$ (which labels the signal or decoy).

The gain of this signal is defined as

$$Q_\mu = \sum_i p_{i|\mu} Y_{i|\mu}, \tag{5.9}$$

where $p_{i|\mu}$ is the probability that pulse distribution $\mu$ contains $i$ photons. This is the sum of all the photon-number probabilities for a given distribution weighted by the probability that a particular photon number survives the channel and sets off Bob's detector.

The error rate is then defined as

$$E_\mu = \sum_i p_{i|\mu} Y_{i|\mu} e_i, \tag{5.10}$$

where $e_i$ is the error rate for $i$ photons.

The essence of the decoy-state method can be summed up with the following equations,

$$\begin{aligned} Y_{i|\mu} &= Y_{i|\nu} \\ e_{i|\mu} &= e_{i|\nu}. \end{aligned} \tag{5.11}$$

These equations state that the probability a pulse makes it to the end of the channel and the error rate depends only on the photon number $i$ and not the pulse distribution that the pulse is selected from. From Eve's point of view she detects a multiphoton pulse in the channel but has no idea which distribution it comes from.

Since Alice and Bob can know the gains $Q_\mu$ and error rates $E_\mu$ experimentally they can use an infinite number of decoys to solve for $Y_1$ and $e_1$ from Eq. (5.9) and Eq. (5.10) respectively. $Y_1$ and $e_1$ are then the quantities required to predict the secret key rate. In practice, a finite number of decoys can be used to provide an upper bound to $e_1$ and a lower bound to $Y_1$. Typically, either two decoys (signal + weak decoy + vacuum) [143] or one decoy (signal + weak decoy) [131] are used experimentally.

The single-photon fraction and error rate are typically derived for coherent state sources which follow a Poissonian photon-number distribution [144]. This type of photon source is characterised by a single number which describes the mean photon number and photon-number variance. Recently this has been extended to sources with arbitrary photon-number distributions which is the approach followed here [145]. The upshot of this work is that for all other parameters being equal the photon source which is mostly sharply peaked with the smallest variance has a higher key rate and largest maximum tolerable loss.

From [145] the key rate in the asymptotic regime is,

$$S = \frac{1}{2}\left(\sum_k p_k P_{0|k} Y_0 + \sum_k p_k P_{1|k} Y_1^L \left(1 - h(e_1^U\right) - \sum_k p_k Q_k f\left(E_k\right) h\left(E_k\right)\right). \quad (5.12)$$

The form of Eq. (5.12) is similar to Eq. (5.1), the key point is that $\sum_k p_k P_{1|k} Y_1^L$ and $e_1^U$ are much tighter to the true single-photon rate and error than the pessimistic counterparts $p_{\text{click}}A$ and $e/A$. The source term $\sum_k p_k P_{1|k} Y_1^L$ should be read as the probability of Alice choosing a pulse distribution $p_k$, the probability of a pulse from that distribution having a single photon $P_{1|k}$ and the lower bound on the single photon yield $Y_1^L$ summed over the different pulse distributions.

The explicit forms of $Y_1^L$ and $e_1^U$ can be found in [145] and are not reproduced here as they do not add any additional insight. One point that is worth covering is that for the security analysis to be valid the different pulse distributions must satisfy

$$\frac{P_{1|\nu}}{P_{1|\mu}} > \max_{i\geq 2} \frac{P_{i|\nu}}{P_{i|\mu}}, \quad (5.13)$$

where $P_{i|\mu(\nu)}$ is the photon number probability for the signal (decoy) distribution $\mu\left(\nu\right)$. Additionally, for the one decoy method the distributions must satisfy,

$$\frac{P_{0|\nu}}{P_{0|\mu}} > \frac{P_{1|\nu}}{P_{1|\mu}}. \quad (5.14)$$

A straightforward way to satisfy these constraints is to take the photon number distribution for the signal state and attenuate the signal to derive the weak decoy or vacuum pulse. This can be done on a shot-by-shot basis with an electro-optic intensity modulator and is a common technique with decoy-state implementations based on coherent states [146].

With an input state containing $i$ photons and an intensity modulator with transmission $T$ the probability of having $j$ photons at the output is

$$P_j = \sum_i \frac{i!}{j!\left(i-j\right)!} P_i T^j \left(1-T\right)^{i-j}. \quad (5.15)$$

The transmission is then a free parameter which can be optimised over to maximise the secret key rate.

At this point it should be noted that this is not the only method to vary the photon number distribution of a single emitter. Under resonant driving the effective two-level system undergoes Rabi oscillations, for different pulse energies $\{\pi, 2\pi, 3\pi\}$ the ratio of vacuum, single-photon and two-photon probabilities change. Previous characterisation of the quantum dot photon number distributions [147] under these excitation energies shows that the $2\pi$ and $3\pi$ pulses are compatible with the one-decoy protocol inequalities, see Eq. (5.13) and Eq. (5.14). Generating decoys by changing the excitation energy has the advantage that the single-photon signal does not have to travel through an intensity modulator which would typically have 3 dB loss. Part of future work will involve characterising the photon number distributions after the frequency conversion process and testing if Eq. (5.13) and Eq. (5.14) are still satisfied.

A noisy single-photon source has no closed form for the photon number distribution but the distribution can be reconstructed under some simplifying assumptions. First we assume a strict ordering in photon number probabilities $p_1 > p_2 > p_3 > ...$ which is valid for a large variety of experimental conditions where the probability of the emitter being re-excited is small compared to the single photon emission rate.

Given this, the second and third order correlations are equal to $g^{(2)} = 2P_2/P_1^2$ and the $g^{(3)} = 6p_3/p_1^3$ [129]. As the source is characterised by click detectors with no photon-number resolving capabilities we also have $p_{\text{click}} = 1 - p_0 = p_1 + p_2 + p_3$ if we truncate the photon-number space to no more than three photons.

The $g^{(3)}(\tau_1, \tau_2)$ was reconstructed using a polarising beam splitter splitting the counts in a 2:1 ratio with a 50/50 beam splitter placed in the brighter arm to create a 1:1:1 splitting ratio across three detectors. The reconstructed value is $g^{(3)}(0, 0) = 0.0018(9)$, the relatively large error is due to only four three-fold coincidences observed in the central peak at zero delay between all three detectors. As with the $g^{(2)}$ measurements the time window is set to include the full width between the pulses ±3 ns.

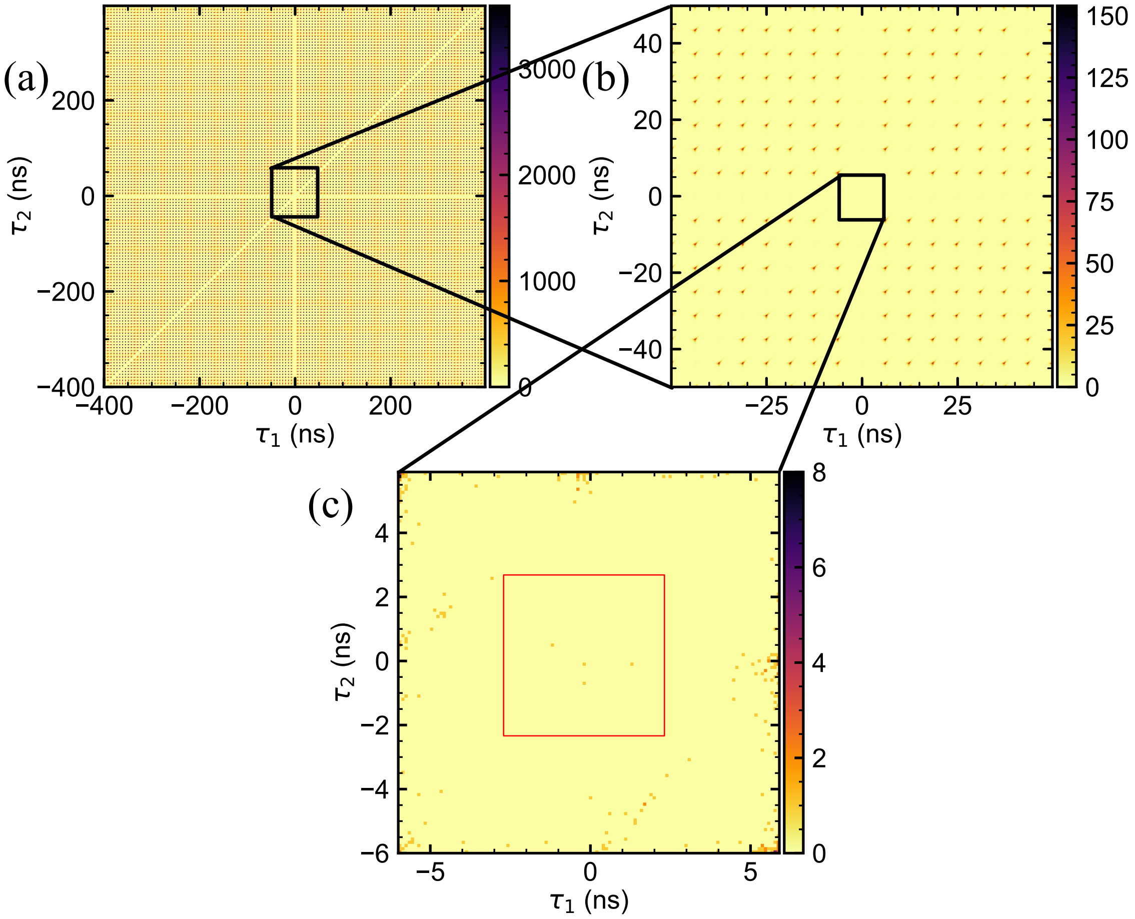

Figure 5.7: Two-dimensional plot of $g^{(3)}(\tau_1, \tau_2)$ at different coincidence windows. Black squares represent the region shown in subsequent plot. The red square in (c) contains the four three-fold coincidences which contribute to the $g^{(3)}(0, 0)$ peak. The peaks are normalised to peaks between 9 $\mu$s to 10 $\mu$s to avoid blinking of the emitter. The peaks used also avoid the diagonal zero line when the time between detectors two and three firing is zero.

The single-photon probability can be found by solving the cubic equation,

$$\frac{g^{(3)}}{6}p_1^3 + \frac{g^{(2)}}{2}p_1^2 + p_1 - p_{\text{click}} = 0. \tag{5.16}$$

Using the value for $p_1$ the photon number distribution up to three photons can be found. Using the values $p_{\text{click}} = 0.0142, g^{(2)} = 0.036, g^{(3)} = 0.0018$, the photon number probabilities are,

$$\begin{aligned} p_0 &= 0.986 \\ p_1 &= 1.42 \times 10^{-2} \\ p_2 &= 3.62 \times 10^{-6} \\ p_3 &= 8.58 \times 10^{-10}. \end{aligned} \tag{5.17}$$

It is worth comparing the performance of a single-photon source to the more common coherent-state decoy methods. The two-decoy method is known to be optimal in the asymptotic regime [144] so we will use this to compare the two cases. Alice sends signal states in the key-generation basis with almost unit probability in the asymptotic regime. The loss added to derive the decoy states are equal (90% transmission), the single-photon source having the $g^{(2)}$ and $g^{(3)}$ set to the experimentally measured values and all other experimental values are equal. For the case of relatively dim sources $\bar{n} = 0.01$ the single-photon source and coherent state perform almost identically in terms of key rate and maximum tolerable loss. Looking at Fig. 5.8(b) this is not surprising, the photon-number distributions are almost identical with 98.6% overlap in the dim case.

Motivated by the recent demonstration of a QD source with 50% extraction efficiency [13] it is also worth comparing a brighter single-photon source to a coherent state of equivalent brightness. In this scenario the long multiphoton tail of the coherent state shown in Fig. 5.8 limits the key rate due to the worse bound on the single-photon yield compared to the single-photon source. This illustrates that as the performance of single-photon sources improves it may become beneficial to transition to using single emitters instead of coherent sources in point-to-point QKD systems.

The performance of the frequency converted QD source is now estimated in a hypothetical decoy-state protocol using the experimental parameters measured. In order to give a realistic estimate the intensity modulator which would be used to generate the decoys states is assumed to have 3 dB insertion loss which is typical of integrated lithium niobate modulators. The mean photon number is therefore half the value

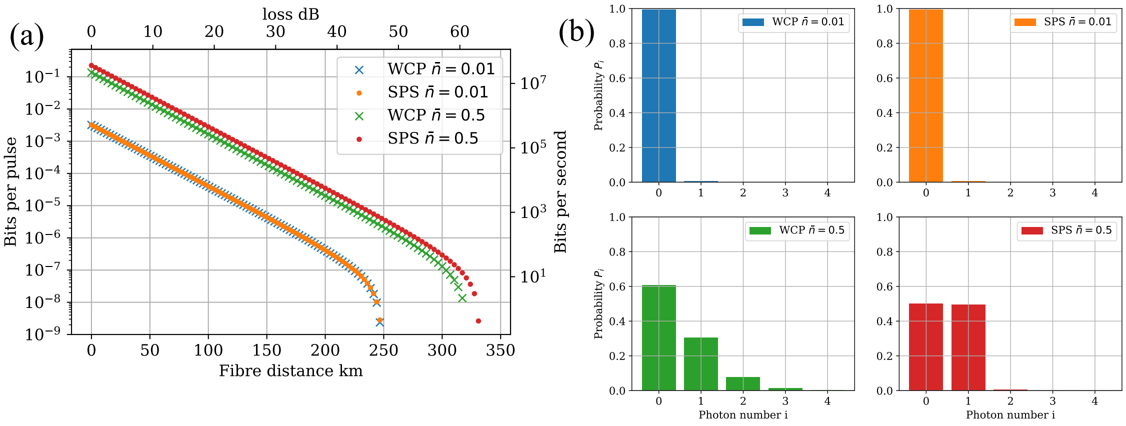

Figure 5.8: Asymptotic key rate for the two decoy protocol for weak coherent sources and a noisy single photon source for different mean photon numbers. (a) Comparison of the asymptotic key rate for the case of a single-photon source and weak coherent state with mean photon number 0.01 and 0.5. For the dim sources the key rate is almost identical which is expected from the similar photon number distributions shown in (b). As the brightness is increased the multiphoton component of the single-photon source increases less rapidly than the coherent state which gives an improvement in key rate and maximum tolerable loss.

used for the GLLP analysis in Section 5.3. The finite key rate formulas are found in [145] and are not reproduced here for brevity. We compare the one-decoy protocol and the two-decoy protocol for the same integration times used in Fig. 5.6. In the numerical simulation the key generation fraction from Alice, the signal-decoy ratio in the one-decoy protocol and the signal-decoy-vacuum ratio in the two-decoy protocol are optimised at each distance and integration time. Additionally, the intensity of the weak decoy for both protocols is numerically optimised.

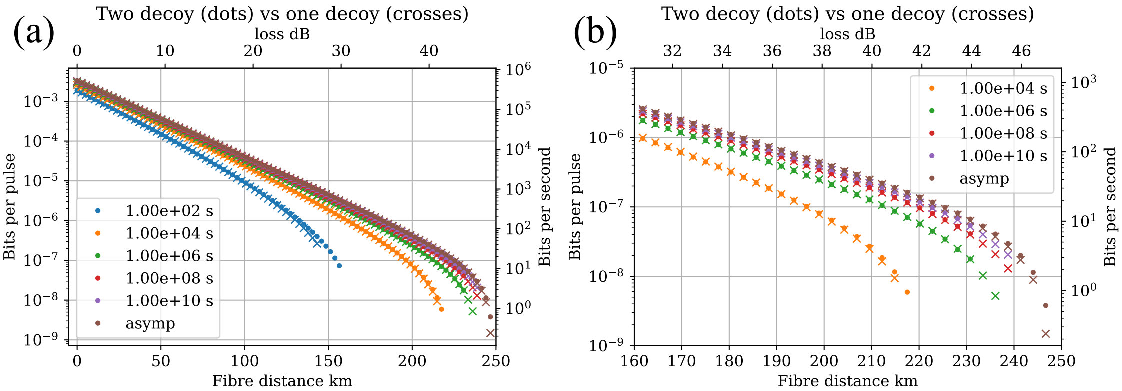

Figure 5.9: Comparison of the 1-decoy and 2-decoy states in the finite-key case for different integration times. There are relatively small differences between both protocols at all distances. Given the experimental simplicity of producing only one decoy it is expected that it may be the preferable protocol in practice. Figure (b) is a zoomed version of the data shown in figure (a).

The decoy-state method shows obvious improvements over the pessimistic GLLP security analysis. For 100 seconds a secure key can be generated at 150 km compared to around 30 km without decoy-states. It is worth noting that for some combinations of integration time and distance the decoy-state method has a lower secret key rate than the case without decoys. This is attributed to the extra 3 dB attenuation from the intensity modulator which would be required to generate the decoys.

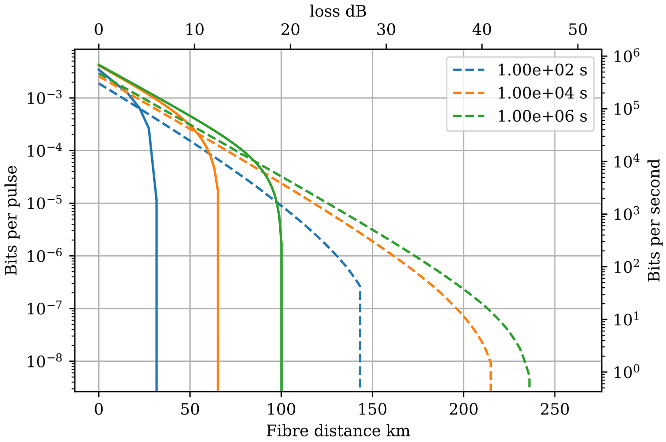

Figure 5.10: Comparison of finite-key rate for the one-decoy state method (dashed line) and the finite-key rate without decoy states (solid lines) for realistic integration times. The decoy state method greatly improves the maximum tolerable loss in all cases but for short distances and long integration times the additional loss due to the required intensity modulator reduces the key rate below the level without decoys.

With the analysis presented here the case for using the decoy-state method with a single-photon source purely for the purpose of QKD is perhaps hard to make. Using a laser diode is experimentally simpler, cheaper and does not require cryogenics, which are typically needed for the best single-photon sources available currently. What we can say is that the ultimate QKD performance is achieved for a true single-photon source with unit efficiency and zero multiphoton noise as imagined in the original BB84 protocol. As the performance of single-photon sources trends towards this ultimate goal, there may come a point in the future where decoy-state QKD with such a source might outperform an equivalent protocol with coherent states. At this point a true comparison can be made to see if the difference in performance is worth the additional experimental overhead in the implementation.

# Chapter 6

# Conclusion

With that we have come to the end of the thesis. To the reader hopefully this has been an interesting journey through time and frequency in quantum photonics. Maybe I have even convinced you that time and frequency are an interesting DoF to start using more seriously in quantum information protocols, then again maybe not...

In this thesis the problem of generating frequency-entangled states in a low-loss way has been discussed and demonstrated. The main hurdle for using frequency-bin entanglement in practical applications continues to be efficient manipulation of these states. The electro-optic modulators used to manipulate frequency-bin states typically come with 3 dB loss for each device due to spatial-mode matching. As with most problems in quantum photonics the perceived solution is integration.

Thin-film lithium niobate seems to be a promising platform, in which separable photon pairs have been generated with type-2 phasematching [148]. The group velocity matching conditions are compatible with generating frequency-bin entanglement using the domain-engineering techniques demonstrated in this thesis. Control of the time-frequency structure of non-classical light sources has also been demonstrated in thin-film LN including spectral shearing and bandwidth compression [149]. The bandwidth of these devices is larger than typical bulk electro-optics with $V_\pi$ on the order of 2.5 V compared to around 7 V for commercial devices. Integrating superconducting detectors onto the same chip along with appropriate filtering would be a promising platform for frequency-bin qudit generation, manipulation and detection in one system. In terms of communication applications these devices would need to have efficient coupling on and off chip and into single-mode fibre. This problem is on-going due to the dimensions of thin-film LN waveguides being a few hundred nm compared to 10 $\mu$m for standard single-mode fibre. Despite these technical hurdles, this direction of research may ultimately prove fruitful.

The second photon source developed in this thesis, the frequency-converted quantum dot, has some promise in terms of communication applications. Using this source in a decoy state protocol will dramatically extend the point-to-point distance over which QKD has been carried out using QDs. Using the brightest QDs available it may start to become competitive with weak coherent sources. Two-photon interference visibilities between distinct QDs has been a limiting factor in scaling up to networking protocols that might involve more than one source. There has been improvement in this direction [150] with visibilities above 90% between different emitters. If these sources can be integrated with photonic structures to enhance collection and count rate then perhaps QDs can be used in long-range multiphoton QKD protocols such as MDI-QKD which require more than one source.

Recently proposed QKD protocols have shown that there is a sliding scale between MDI-QKD which requires two sources and a two-photon interference event to twin-field QKD [151, 152] which only requires a single-photon detection at the central node at the cost of phase-locking both communication channels. The family of protocols between these two extremes are based on asynchronous two-photon interference [153, 154] and relax the phase locking requirements of twin-field QKD and can surpass the repeaterless key rate [155]. Frequency converted QD sources may well be an ideal candidate for these protocols, as they can theoretically achieve higher two-photon interference visibilities than two weak coherent sources which are limited to 50% and therefore have lower error rates and the issue of driving two single-emitters in a phase-locked way is side-stepped. Using reverse-wave frequency conversion would result in near unit spectral purity of the converted photons. The spectral reshaping and purification that naturally occurs in reverse-wave FC would allow for multiple different quantum emitters to be integrated into the same network. This may relax the source requirements required to realise a practical quantum internet for communication and entanglement distribution.

# Appendix A

# Derivation of PMF for a periodically-poled crystal

Here the steps for the derivation of the quasi-phasematched PMF Eq. (2.38) in Chapter 2 are laid out explicitly,

$$\begin{aligned}\phi_{pp}\left(\Delta k\right) &= \sum_{n=1}^{N}\int_{(n-1)l_c}^{nl_c} \mathrm{d}z\left(-1\right)^{n-1} e^{i\Delta kz}\\ &= i\sum_{n=1}^{N}\underbrace{\left(-1\right)^{n}}_{e^{in\pi}} e^{i\Delta knl_c}\frac{1-e^{-i\Delta kl_c}}{\Delta k}.\end{aligned} \tag{A.1}$$

Using the fact that $-1 = e^{i\pi}$ and evaluating the summation as $\sum_{n=1}^{N} e^{in\pi}e^{i\Delta knl_c} = \frac{e^{i\Delta kl_c}\left(e^{iN(\Delta kl_c+\pi)}-1\right)}{1+e^{i\Delta kl_c}}$ we can write,

$$\begin{aligned}\phi_{pp}\left(\Delta k\right) &= i\frac{e^{i\Delta kl_c}\left(e^{iN(\Delta kl_c+\pi)}-1\right)}{1+e^{i\Delta kl_c}}\frac{1-e^{-i\Delta kl_c}}{\Delta k}\\ &= i\left(e^{i\left(\Delta k-\frac{\pi}{l_c}\right)Nl_c}-1\right)\frac{1}{\Delta k}\frac{e^{i\Delta kl_c}-1}{e^{i\Delta kl_c}+1},\end{aligned} \tag{A.2}$$

in the second line the factors $\frac{e^{i\Delta kl_c}\left(1-e^{-i\Delta kl_c}\right)}{1+e^{i\Delta kl_c}}$ are gathered together.

Finally with some creative factors of $1 = \frac{Nl_c}{Nl_c} = \frac{\Delta k-\frac{\pi}{l_c}}{\Delta k-\frac{\pi}{l_c}}$ and using

$1 - e^{ix} = e^{ix/2}\left(e^{ix/2} - e^{-ix/2}\right)$ we can write,

$$\begin{aligned}\phi_{pp}\left(\Delta k\right) &= iNl_c e^{i\left(\Delta k - \frac{\pi}{l_c}\right)\frac{Nl_c}{2}} \\ &\times \frac{e^{i\left(\Delta k - \frac{\pi}{l_c}\right)\frac{Nl_c}{2}} - e^{-i\left(\Delta k - \frac{\pi}{l_c}\right)\frac{Nl_c}{2}}}{2\left(\Delta k - \frac{\pi}{l_c}\right)\frac{Nl_c}{2}} \\ &\times \frac{\Delta k - \frac{\pi}{l_c}}{\Delta k}\frac{e^{i\Delta k l_c} - 1}{e^{i\Delta k l_c} + 1} \\ &= Le^{i\left(\Delta k - \frac{\pi}{l_c}\right)\frac{L}{2}}\operatorname{sinc}\left(\left(\Delta k - \frac{\pi}{l_c}\right)\frac{L}{2}\right) \times \frac{\Delta k - \frac{\pi}{l_c}}{\Delta k}\frac{1 - e^{i\Delta k l_c}}{1 + e^{i\Delta k l_c}} \\ &= \phi_b\left(\Delta k - \frac{\pi}{l_c}\right) \times \phi_{\text{add}}\left(\Delta k\right).\end{aligned} \tag{A.3}$$

In the final passage we have used the fact that the product of the domain length times the number of domains gives the length of the crystal $Nl_c = L$ in the first line along with the identity $i\operatorname{sinc}\left(x\right) = \dfrac{\exp\left(ix\right) - \exp\left(-ix\right)}{2x}$ in the second line.

# Appendix B

# Electro-optic modulator characterisation

The high speed electro-optic modulator (EOM) consists of a lithium niobate waveguide which is end coupled with two polarisation maintaining fibres. The input fibre is glued such that the slow axis of the fibre is at 45° with respect to the crystal axis. When the input polarisation is correctly aligned to the slow-axis of the fibre, one component of the polarisation vector is aligned to the electro-optically active axis of the crystal and experiences a refractive index which depends on the voltage across the device. The orthogonal component of the polarisation vector accumulates a fixed phase. By sweeping the voltage sent to the device one can then dial up any polarisation vector on the $\{D, R, A, L\}$ great circle of the Bloch sphere. The device specifications state around 2 dB insertion loss and 20 dB polarisation extinction ratio.

The device was tested using frequency converted laser light which passed through the same optical setup used to convert the single photons from the QD source, see Fig. 4.7. The output polarisation output state was analysed using the BB84 receiver, see Fig. 5.2.

It was quickly noted that the polarisation state varied dramatically and erratically when using 1550 nm light from the frequency conversion setup. The EOM was held

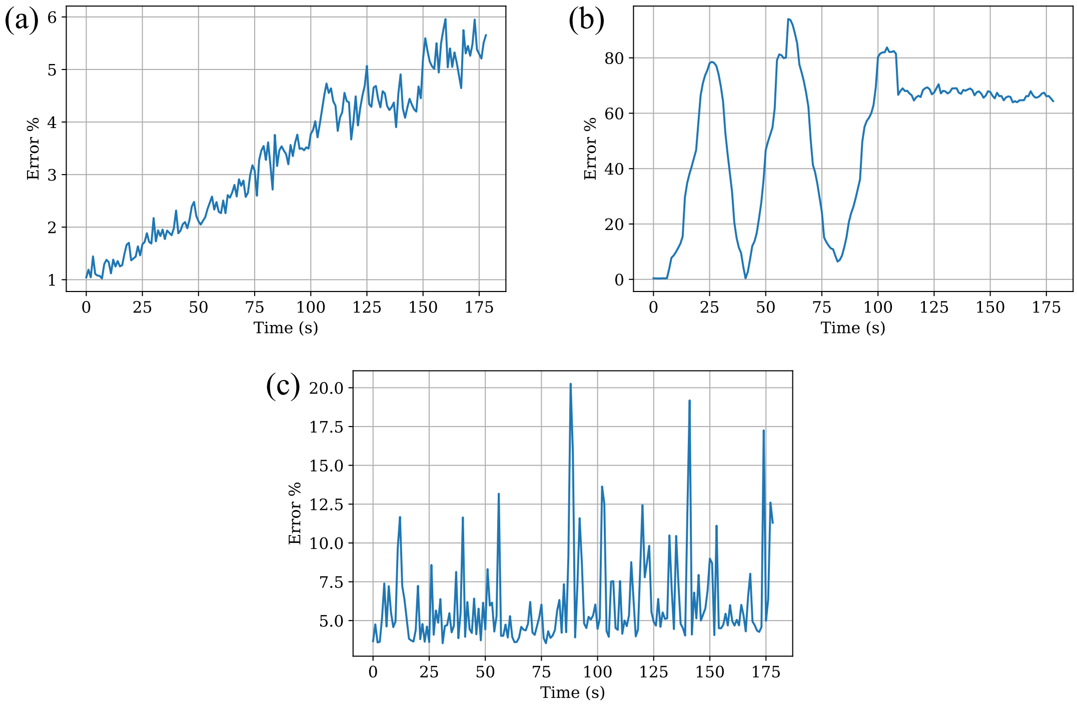

Figure B.1: Typical time traces for the polarisation encoding error for a distributed feedback laser diode at 1550 nm held at fixed temperature sent through the EOM in (a). The encoding error for the same diode with the temperature varied which sweeps the diode wavelength is shown in (b). The wavelength is swept through around 1.5 nm before the diode settles at a new temperature. A similar time trace for the frequency converted laser light from the experimental setup used to convert the QD single photons is shown in (c).

at a fixed DC voltage and the output state was aligned such that the majority of the detected counts were transmitted through one of the polarising beam splitters in the receiver. The polarisation encoding error can then be calculated as

$$e = \frac{N_R}{N_T + N_R}, \tag{B.1}$$

where $N_R$ and $N_T$ are the number of counts on the reflected and transmitted ports respectively. A typical time trace of the error for three minutes is shown in Fig. B.1 (c) for the frequency converted light. The encoding error was also tested sending a 1550 nm diode laser through the EOM to try and understand the reason for the erratic behaviour when using frequency converted light.

With the diode temperature fixed the error linearly increases with time which is attributed to temperature drifts in the fibres leading to and from the EOM itself.

The sinusoidal-like curves in Fig. B.1(b) are due to the projection onto the $\{H, V\}$ axis defined by the polarising beam splitter from the polarisation state processing around the Bloch sphere as the input wavelength varies. In Fig. B.1(c) the sharp jumps in the error are due to mode hopping seen in the spectrum of the seed laser used for conversion, Fig. 4.4. This spectral instability then gives large encoding errors on Alice's source end. A more faithful version of the BB84 protocol was attempted where a pre-programmed sequence of states was encoded on a shot-by-shot basis. Unfortunately, the measured error rate was above the threshold of $\approx 11\%$ required to generate a key in the asymptotic limit. Future work on this experiment should focus on locking the laser to an external cavity resonance or replacing the laser system with a commercial option. At this point a true shot-by-shot encoded implementation of BB84 should be possible.

# Bibliography

## Introduction

[1]W. H. Louisell, A. Yariv, and A. E. Siegman, “Quantum fluctuations and noise in parametric processes. i.”, Phys. Rev. **124**, 1646–1654 (1961).

[2]D. Magde and H. Mahr, “Study in ammonium dihydrogen phosphate of spontaneous parametric interaction tunable from 4400 to 16 000 å”, Phys. Rev. Lett. **18**, 905–907 (1967).

[3]R. L. Byer and S. E. Harris, “Power and bandwidth of spontaneous parametric emission”, Phys. Rev. **168**, 1064–1068 (1968).

[4]P. G. Kwiat, K. Mattle, H. Weinfurter, A. Zeilinger, A. V. Sergienko, and Y. Shih, “New high-intensity source of polarization-entangled photon pairs”, Phys. Rev. Lett. **75**, 4337–4341 (1995).

[5]J. G. Rarity and P. R. Tapster, “Experimental violation of Bell’s inequality based on phase and momentum”, Phys. Rev. Lett. **64**, 2495–2498 (1990).

[6]C. K. Law and J. H. Eberly, “Analysis and interpretation of high transverse entanglement in optical parametric down conversion”, Phys. Rev. Lett. **92**, 127903 (2004).

[7]A. Mair, A. Vaziri, G. Weihs, and A. Zeilinger, “Entanglement of the orbital angular momentum states of photons”, Nature **412**, 313–316 (2001).

[8]L. Olislager, J. Cussey, A. T. Nguyen, P. Emplit, S. Massar, J.-M. Merolla, and K. P. Huy, “Frequency-bin entangled photons”, Phys. Rev. A **82**, 013804 (2010).

[9] I. Marcikic, H. de Riedmatten, W. Tittel, V. Scarani, H. Zbinden, and N. Gisin, "Time-bin entangled qubits for quantum communication created by femtosecond pulses", Phys. Rev. A **66**, 062308 (2002).

[10] J. T. Barreiro, N. K. Langford, N. A. Peters, and P. G. Kwiat, "Generation of hyperentangled photon pairs", Phys. Rev. Lett. **95**, 260501 (2005).

[11] F. Graffitti, "Tailored quantum light for photonic quantum technologies", PhD thesis (Heriot-Watt University, 2021).

[12] P. Michler, A. Imamoğlu, M. Mason, P. Carson, G. Strouse, and S. Buratto, "Quantum correlation among photons from a single quantum dot at room temperature", Nature **406**, 968–970 (2000).

[13] N. Tomm, A. Javadi, N. O. Antoniadis, D. Najer, M. C. Löbl, A. R. Korsch, R. Schott, S. R. Valentin, A. D. Wieck, A. Ludwig, and R. J. Warburton, "A bright and fast source of coherent single photons", Nature Nanotechnology **16**, 399–403 (2021).

## Nonlinear Optics

[14] R. W. Boyd, *Nonlinear optics, third edition*, 3rd (Academic Press, Inc., Orlando, FL, USA, 2008).

[15] T. H. Maiman, "Stimulated optical radiation in ruby", Nature **187**, 493–494 (1960).

[16] Q. Lin, F. Yaman, and G. P. Agrawal, "Photon-pair generation by four-wave mixing in optical fibers", Opt. Lett. **31**, 1286–1288 (2006).

[17] Q. Li, M. Davanço, and K. Srinivasan, "Efficient and low-noise single-photon-level frequency conversion interfaces using silicon nanophotonics", Nature Photonics **10**, 406–414 (2016).

[18] A. Singh, Q. Li, S. Liu, Y. Yu, X. Lu, C. Schneider, S. Höfling, J. Lawall, V. Verma, R. Mirin, S. W. Nam, J. Liu, and K. Srinivasan, "Quantum frequency conversion of a quantum dot single-photon source on a nanophotonic chip", Optica **6**, 563–569 (2019).

[19]C. Parry, P. B. Main, T. A. Wright, and P. J. Mosley, “Group-velocity symmetry in photonic crystal fibre for ultra-tunable quantum frequency conversion”, Journal of Optics **23**, 075202 (2021).

[20]K. Bonsma-Fisher, P. Bustard, C. Parry, T. Wright, D. England, B. Sussman, and P. Mosley, “Ultratunable quantum frequency conversion in photonic crystal fiber”, arXiv:2207.14706 (2022).

[21]B. Brecht, “Engineering ultrafast quantum frequency conversion”, PhD thesis (Universität Paderborn, 2014).

[22]N. Quesada and J. E. Sipe, “Effects of time ordering in quantum nonlinear optics”, Phys. Rev. A **90**, 063840 (2014).

[23]A. B. U’Ren, C. Silberhorn, R. Erdmann, K. Banaszek, W. P. Grice, I. A. Walmsley, and M. G. Raymer, “Generation of pure-state single-photon wavepackets by conditional preparation based on spontaneous parametric downconversion”, arXiv preprint quant-ph/0611019 (2006).

[24]S. Emanueli and A. Arie, “Temperature-dependent dispersion equations for $KTiOPO_4$ and $KTiOAsO_4$”, Appl. Opt. **42**, 6661–6665 (2003).

[25]O. Gayer, Z. Sacks, E. Galun, and A. Arie, “Temperature and wavelength dependent refractive index equations for MgO-doped congruent and stoichiometric $LiNbO_3$”, Applied Physics B **91**, 343–348 (2008).

[26]C. K. Law, I. A. Walmsley, and J. H. Eberly, “Continuous frequency entanglement: effective finite Hilbert space and entropy control”, Phys. Rev. Lett. **84**, 5304–5307 (2000).

[27]A. M. Brańczyk, T. C. Ralph, W. Helwig, and C. Silberhorn, “Optimized generation of heralded fock states using parametric down-conversion”, New Journal of Physics **12**, 063001 (2010).

[28]M. Raymer, S. van Enk, C. McKinstrie, and H. McGuinness, “Interference of two photons of different color”, Optics Communications **283**, 747–752 (2010).

[29]K. De Greve, L. Yu, P. L. McMahon, J. S. Pelc, C. M. Natarajan, N. Y. Kim, E. Abe, S. Maier, C. Schneider, M. Kamp, S. Höfling, R. H. Hadfield, A. Forchel,

M. M. Fejer, and Y. Yamamoto, “Quantum-dot spin–photon entanglement via frequency downconversion to telecom wavelength”, Nature **491**, 421–425 (2012).

[30]L. Yu, C. M. Natarajan, T. Horikiri, C. Langrock, J. S. Pelc, M. G. Tanner, E. Abe, S. Maier, C. Schneider, S. Höfling, M. Kamp, R. H. Hadfield, M. M. Fejer, and Y. Yamamoto, “Two-photon interference at telecom wavelengths for time-bin-encoded single photons from quantum-dot spin qubits”, Nature Communications **6**, 8955 (2015).

[31]S. Ates, I. Agha, A. Gulinatti, I. Rech, M. T. Rakher, A. Badolato, and K. Srinivasan, “Two-photon interference using background-free quantum frequency conversion of single photons emitted by an InAs quantum dot”, Phys. Rev. Lett. **109**, 147405 (2012).

[32]S. Zaske, A. Lenhard, C. A. Keßler, J. Kettler, C. Hepp, C. Arend, R. Albrecht, W.-M. Schulz, M. Jetter, P. Michler, and C. Becher, “Visible-to-telecom quantum frequency conversion of light from a single quantum emitter”, Physical Review Letters **109**, 147404 (2012).

[33]J. H. Weber, B. Kambs, J. Kettler, S. Kern, J. Maisch, H. Vural, M. Jetter, S. L. Portalupi, C. Becher, and P. Michler, “Two-photon interference in the telecom C-band after frequency conversion of photons from remote quantum emitters”, Nature Nanotechnology **14**, 23–26 (2019).

[34]A. Dréau, A. Tcheborateva, A. E. Mahdaoui, C. Bonato, and R. Hanson, “Quantum Frequency Conversion of Single Photons from a Nitrogen-Vacancy Center in Diamond to Telecommunication Wavelengths”, Physical Review Applied **9**, 064031 (2018).

[35]V. Krutyanskiy, M. Meraner, J. Schupp, and B. P. Lanyon, “Polarisation-preserving photon frequency conversion from a trapped-ion-compatible wavelength to the telecom C-band”, Applied Physics B **123**, 228 (2017).

[36]V. Krutyanskiy, M. Meraner, J. Schupp, V. Krcmarsky, H. Hainzer, and B. P. Lanyon, “Light-matter entanglement over 50 km of optical fibre”, npj Quantum Information **5**, 72 (2019).

[37]M. Meraner, A. Mazloom, V. Krutyanskiy, V. Krcmarsky, J. Schupp, D. A. Fioretto, P. Sekatski, T. E. Northup, N. Sangouard, and B. P. Lanyon, "Indistinguishable photons from a trapped-ion quantum network node", Phys. Rev. A **102**, 052614 (2020).

[38]J.-P. W. MacLean, S. Schwarz, and K. J. Resch, "Reconstructing ultrafast energy-time-entangled two-photon pulses", Phys. Rev. A **100**, 033834 (2019).

[39]K. Zielnicki, K. Garay-Palmett, D. Cruz-Delgado, H. Cruz-Ramirez, M. F. O'Boyle, B. Fang, V. O. Lorenz, A. B. U'Ren, and P. G. Kwiat, "Joint spectral characterization of photon-pair sources", Journal of Modern Optics **65**, 1141–1160 (2018).

[40]J. A. Armstrong, N. Bloembergen, J. Ducuing, and P. S. Pershan, "Interactions between light waves in a nonlinear dielectric", Phys. Rev. **127**, 1918–1939 (1962).

[41]P. A. Franken and J. F. Ward, "Optical harmonics and nonlinear phenomena", Rev. Mod. Phys. **35**, 23–39 (1963).

[42]M. Houe and P. D. Townsend, "An introduction to methods of periodic poling for second-harmonic generation", Journal of Physics D: Applied Physics **28**, 1747–1763 (1995).

[43]M. F. Saleh, "Modelling spontaneous four-wave mixing in periodically tapered waveguides", Opt. Express **27**, 11979–11990 (2019).

# Time-Frequency entangled photon pairs

[9]I. Marcikic, H. de Riedmatten, W. Tittel, V. Scarani, H. Zbinden, and N. Gisin, "Time-bin entangled qubits for quantum communication created by femtosecond pulses", Phys. Rev. A **66**, 062308 (2002).

[26]C. K. Law, I. A. Walmsley, and J. H. Eberly, "Continuous frequency entanglement: effective finite Hilbert space and entropy control", Phys. Rev. Lett. **84**, 5304–5307 (2000).

[44]M. A. Arbore, A. Galvanauskas, D. Harter, M. H. Chou, and M. M. Fejer, "Engineerable compression of ultrashort pulses by use of second-harmonic generation in chirped-period-poled lithium niobate", Opt. Lett. **22**, 1341–1343 (1997).

[45]G. Imeshev, M. A. Arbore, M. M. Fejer, A. Galvanauskas, M. Fermann, and D. Harter, “Ultrashort-pulse second-harmonic generation with longitudinally nonuniform quasi-phase-matching gratings: pulse compression and shaping”, J. Opt. Soc. Am. B **17**, 304–318 (2000).

[46]V. Y. Shur, E. L. Rumyantsev, E. V. Ndcolaeva, E. I. Shishkin, R. G. Batchko, M. M. Fejer, and R. L. Byer, “Recent achievements in domain engineering in lithium niobate and lithium tantalate”, Ferroelectrics **257**, 191–202 (2001).

[47]A. M. Brańczyk, A. Fedrizzi, T. M. Stace, T. C. Ralph, and A. G. White, “Engineered optical nonlinearity for quantum light sources”, Opt. Express **19**, 55–65 (2011).

[48]N. Quesada and A. M. Brańczyk, “Gaussian functions are optimal for waveguided nonlinear-quantum-optical processes”, Phys. Rev. A **98**, 043813 (2018).

[49]P. B. Dixon, J. H. Shapiro, and F. N. C. Wong, “Spectral engineering by Gaussian phase-matching for quantum photonics”, Opt. Express **21**, 5879–5890 (2013).

[50]C. Chen, C. Bo, M. Y. Niu, F. Xu, Z. Zhang, J. H. Shapiro, and F. N. C. Wong, “Efficient generation and characterization of spectrally factorable biphotons”, Opt. Express **25**, 7300–7312 (2017).

[51]C. Cui, R. Arian, S. Guha, N. Peyghambarian, Q. Zhuang, and Z. Zhang, “Wavefunction engineering for spectrally uncorrelated biphotons in the telecommunication band based on a machine-learning framework”, Phys. Rev. Applied **12**, 034059 (2019).

[52]W.-H. Cai, Y. Tian, S. Wang, C. You, Q. Zhou, and R.-B. Jin, “Optimized design of the lithium niobate for spectrally-pure-state generation at MIR wavelengths using metaheuristic algorithm”, arXiv:2203.14783 (2022).

[53]J.-L. Tambasco, A. Boes, L. G. Helt, M. J. Steel, and A. Mitchell, “Domain engineering algorithm for practical and effective photon sources”, Opt. Express **24**, 19616–19626 (2016).

[54]F. Graffitti, D. Kundys, D. T. Reid, A. M. Brańczyk, and A. Fedrizzi, “Pure down-conversion photons through sub-coherence-length domain engineering”, Quantum Science and Technology **2**, 035001 (2017).

[55]Graffitti, P. Barrow, M. Proietti, D. Kundys, and A. Fedrizzi, "Independent high-purity photons created in domain-engineered crystals", Optica **5**, 514–517 (2018).

[56]A. Pickston, F. Graffitti, P. Barrow, C. L. Morrison, J. Ho, A. M. Brańczyk, and A. Fedrizzi, "Optimised domain-engineered crystals for pure telecom photon sources", Opt. Express **29**, 6991–7002 (2021).

[57]J. Ho, G. Moreno, S. Brito, F. Graffitti, C. L. Morrison, R. Nery, A. Pickston, M. Proietti, R. Rabelo, A. Fedrizzi, et al., "Entanglement-based quantum communication complexity beyond Bell nonlocality", npj Quantum Information **8**, 1–7 (2022).

[58]A. Pickston, J. Ho, A. Ulibarrena, F. Grasselli, M. Proietti, C. L. Morrison, P. Barrow, F. Graffitti, and A. Fedrizzi, "Experimental network advantage for quantum conference key agreement", arXiv:2207.01643 (2022).

[59]H.-S. Zhong, H. Wang, Y.-H. Deng, M.-C. Chen, L.-C. Peng, Y.-H. Luo, J. Qin, D. Wu, X. Ding, Y. Hu, P. Hu, X.-Y. Yang, W.-J. Zhang, H. Li, Y. Li, X. Jiang, L. Gan, G. Yang, L. You, Z. Wang, L. Li, N.-L. Liu, C.-Y. Lu, and J.-W. Pan, "Quantum computational advantage using photons", Science **370**, 1460–1463 (2020).

[60]C. Reimer, S. Sciara, P. Roztocki, M. Islam, L. Romero Cortés, Y. Zhang, B. Fischer, S. Loranger, R. Kashyap, A. Cino, S. T. Chu, B. E. Little, D. J. Moss, L. Caspani, W. J. Munro, J. Azaña, M. Kues, and R. Morandotti, "High-dimensional one-way quantum processing implemented on d-level cluster states", Nature Physics **15**, 148–153 (2019).

[61]A. Boaron, B. Korzh, R. Houlmann, G. Boso, D. Rusca, S. Gray, M.-J. Li, D. Nolan, A. Martin, and H. Zbinden, "Simple 2.5 GHz time-bin quantum key distribution", Applied Physics Letters **112**, 171108 (2018).

[62]L. Olislager, E. Woodhead, K. Phan Huy, J.-M. Merolla, P. Emplit, and S. Massar, "Creating and manipulating entangled optical qubits in the frequency domain", Phys. Rev. A **89**, 052323 (2014).

[63]H.-H. Lu, E. M. Simmerman, P. Lougovski, A. M. Weiner, and J. M. Lukens, "Fully arbitrary control of frequency-bin qubits", Phys. Rev. Lett. **125**, 120503 (2020).

[64]M. Kues, C. Reimer, P. Roztocki, L. R. Cortés, S. Sciara, B. Wetzel, Y. Zhang, A. Cino, S. T. Chu, B. E. Little, D. J. Moss, L. Caspani, J. Azaña, and R. Morandotti, "On-chip generation of high-dimensional entangled quantum states and their coherent control", Nature **546**, 622–626 (2017).

[65]H.-H. Lu, K. V. Myilswamy, R. S. Bennink, S. Seshadri, M. S. Alshaykh, J. Liu, T. J. Kippenberg, D. E. Leaird, A. M. Weiner, and J. M. Lukens, "Full quantum state tomography of high-dimensional on-chip biphoton frequency combs with randomized measurements", arXiv:2108.04124 (2021).

[66]A. Eckstein, B. Brecht, and C. Silberhorn, "A quantum pulse gate based on spectrally engineered sum frequency generation", Opt. Express **19**, 13770–13778 (2011).

[67]V. Ansari, J. M. Donohue, B. Brecht, and C. Silberhorn, "Remotely projecting states of photonic temporal modes", Opt. Express **28**, 28295–28305 (2020).

[68]F. Graffitti, A. Barrow Peter and, A. M. Brańczyk, and A. Fedrizzi, "Direct generation of tailored pulse-mode entanglement", Phys. Rev. Lett. **124**, 053603 (2020).

[69]V. Ansari, J. M. Donohue, B. Brecht, and C. Silberhorn, "Tailoring nonlinear processes for quantum optics with pulsed temporal-mode encodings", Optica **5**, 534–550 (2018).

[70]K.-C. Chang, X. Cheng, M. C. Sarihan, A. K. Vinod, Y. S. Lee, T. Zhong, Y.-X. Gong, Z. Xie, J. H. Shapiro, F. N. C. Wong, and C. W. Wong, "648 Hilbert-space dimensionality in a biphoton frequency comb: entanglement of formation and Schmidt mode decomposition", npj Quantum Information **7**, 48 (2021).

[71]S. K. Joshi, D. Aktas, S. Wengerowsky, M. Lončarić, S. P. Neumann, B. Liu, T. Scheidl, G. C. Lorenzo, Ž. Samec, L. Kling, A. Qiu, M. Razavi, M. Stipčević, J. G. Rarity, and R. Ursin, "A trusted-node-free eight-user metropolitan quantum communication network", Science Advances **6**, eaba0959 (2020).

[72]A. O. C. Davis, V. Thiel, M. Karpiński, and B. J. Smith, "Measuring the single-photon temporal-spectral wave function", Phys. Rev. Lett. **121**, 083602 (2018).

[73] A. O. C. Davis, V. Thiel, and B. J. Smith, “Measuring the quantum state of a photon pair entangled in frequency and time”, Optica **7**, 1317–1322 (2020).

[74] C. Iaconis and I. Walmsley, “Self-referencing spectral interferometry for measuring ultrashort optical pulses”, IEEE Journal of Quantum Electronics **35**, 501–509 (1999).

[75] V. Ansari, G. Harder, M. Allgaier, B. Brecht, and C. Silberhorn, “Temporal-mode measurement tomography of a quantum pulse gate”, Phys. Rev. A **96**, 063817 (2017).

[76] A. Fedrizzi, T. Herbst, A. Poppe, T. Jennewein, and A. Zeilinger, “A wavelength-tunable fiber-coupled source of narrowband entangled photons”, Opt. Express **15**, 15377–15386 (2007).

[77] M. Avenhaus, A. Eckstein, P. J. Mosley, and C. Silberhorn, “Fiber-assisted single-photon spectrograph”, Opt. Lett. **34**, 2873–2875 (2009).

[78] S. Ramelow, L. Ratschbacher, A. Fedrizzi, N. K. Langford, and A. Zeilinger, “Discrete tunable color entanglement”, Phys. Rev. Lett. **103**, 253601 (2009).

[79] A. Fedrizzi, T. Herbst, M. Aspelmeyer, M. Barbieri, T. Jennewein, and A. Zeilinger, “Anti-symmetrization reveals hidden entanglement”, New Journal of Physics **11**, 103052 (2009).

[80] N. B. Lingaraju, H.-H. Lu, S. Seshadri, P. Imany, D. E. Leaird, J. M. Lukens, and A. M. Weiner, “Quantum frequency combs and Hong-Ou-Mandel interferometry: the role of spectral phase coherence”, Opt. Express **27**, 38683–38697 (2019).

[81] M. A. Broome, M. P. Almeida, A. Fedrizzi, and A. G. White, “Reducing multi-photon rates in pulsed down-conversion by temporal multiplexing”, Opt. Express **19**, 22698–22708 (2011).

[82] F. Graffitti, V. D’Ambrosio, M. Proietti, J. Ho, B. Piccirillo, C. de Lisio, L. Marrucci, and A. Fedrizzi, “Hyperentanglement in structured quantum light”, Phys. Rev. Research **2**, 043350 (2020).

[83] S. Wengerowsky, S. K. Joshi, F. Steinlechner, H. Hübel, and R. Ursin, “An entanglement-based wavelength-multiplexed quantum communication network”, Nature **564**, 225–228 (2018).

[84]J. Řeháček, B.-G. Englert, and D. Kaszlikowski, “Minimal qubit tomography”, Phys. Rev. A **70**, 052321 (2004).

[85]R.-B. Jin, R. Shimizu, K. Wakui, M. Fujiwara, T. Yamashita, S. Miki, H. Terai, Z. Wang, and M. Sasaki, “Pulsed Sagnac polarization-entangled photon source with a PPKTP crystal at telecom wavelength”, Opt. Express **22**, 11498–11507 (2014).

[86]S. P. Neumann, M. Selimovic, M. Bohmann, and R. Ursin, “Experimental entanglement generation for quantum key distribution beyond 1 Gbit/s”, arXiv:2107.07756 (2021).

[87]D. M. Greenberger, M. A. Horne, and A. Zeilinger, “Going beyond bell’s theorem”, in *Bell’s theorem, quantum theory and conceptions of the universe* (Springer, 1989), pp. 69–72.

[88]D. Bouwmeester, J.-W. Pan, M. Daniell, H. Weinfurter, and A. Zeilinger, “Observation of three-photon greenberger-horne-zeilinger entanglement”, Phys. Rev. Lett. **82**, 1345–1349 (1999).

[89]J. M. Donohue, M. Agnew, J. Lavoie, and K. J. Resch, “Coherent ultrafast measurement of time-bin encoded photons”, Phys. Rev. Lett. **111**, 153602 (2013).

# Quantum dot frequency conversion

[33]J. H. Weber, B. Kambs, J. Kettler, S. Kern, J. Maisch, H. Vural, M. Jetter, S. L. Portalupi, C. Becher, and P. Michler, “Two-photon interference in the telecom C-band after frequency conversion of photons from remote quantum emitters”, Nature Nanotechnology **14**, 23–26 (2019).

[35]V. Krutyanskiy, M. Meraner, J. Schupp, and B. P. Lanyon, “Polarisation-preserving photon frequency conversion from a trapped-ion-compatible wavelength to the telecom C-band”, Applied Physics B **123**, 228 (2017).

[66]A. Eckstein, B. Brecht, and C. Silberhorn, “A quantum pulse gate based on spectrally engineered sum frequency generation”, Opt. Express **19**, 13770–13778 (2011).

[90]P. Chaiwongkhot, S. Hosseini, A. Ahmadi, B. L. Higgins, D. Dalacu, P. J. Poole, R. L. Williams, M. E. Reimer, and T. Jennewein, "Enhancing secure key rates of satellite QKD using a quantum dot single-photon source", arXiv:2009.11818 (2020).

[91]K. Takemoto, Y. Nambu, T. Miyazawa, Y. Sakuma, T. Yamamoto, S. Yorozu, and Y. Arakawa, "Quantum key distribution over 120 km using ultrahigh purity single-photon source and superconducting single-photon detectors", Scientific Reports **5**, 14383 (2015).

[92]C. L. Morrison, M. Rambach, Z. X. Koong, F. Graffitti, F. Thorburn, A. K. Kar, Y. Ma, S.-I. Park, J. D. Song, N. G. Stoltz, D. Bouwmeester, A. Fedrizzi, and B. D. Gerardot, "A bright source of telecom single photons based on quantum frequency conversion", Applied Physics Letters **118**, 174003 (2021).

[93]B. Da Lio, C. Faurby, X. Zhou, M. L. Chan, R. Uppu, H. Thyrrestrup, S. Scholz, A. D. Wieck, A. Ludwig, P. Lodahl, and L. Midolo, "A pure and indistinguishable single-photon source at telecommunication wavelength", Advanced Quantum Technologies **5**, 2200006 (2022).

[94]X. You, M.-Y. Zheng, S. Chen, R.-Z. Liu, J. Qin, M.-C. Xu, Z.-X. Ge, T.-H. Chung, Y.-K. Qiao, Y.-F. Jiang, et al., "Quantum interference between independent solid-state single-photon sources separated by 300 km fiber", arXiv:2106.15545 (2021).

[95]M. T. Rakher, "Quantum optics with quantum dots in microcavities", PhD thesis (University of California, Santa Barbara, Jan. 2008).

[96]M. T. Rakher, N. G. Stoltz, L. A. Coldren, P. M. Petroff, and D. Bouwmeester, "Externally mode-matched cavity quantum electrodynamics with charge-tunable quantum dots", Phys. Rev. Lett. **102**, 097403 (2009).

[97]S. Strauf, N. G. Stoltz, M. T. Rakher, L. A. Coldren, P. M. Petroff, and D. Bouwmeester, "High-frequency single-photon source with polarization control", Nature Photonics **1**, 704–708 (2007).

[98] J. R. Macdonald, S. J. Beecher, P. A. Berry, G. Brown, K. L. Schepler, and A. K. Kar, "Efficient mid-infrared Cr: ZnSe channel waveguide laser operating at 2486 nm", Optics Letters **38**, 2194–2196 (2013).

[99] R. V. Roussev, C. Langrock, J. R. Kurz, and M. M. Fejer, "Periodically poled lithium niobate waveguide sum-frequency generator for efficient single-photon detection at communication wavelengths", Optics Letters **29**, 1518–1520 (2004).

[100] T. S. Santana, Y. Ma, R. N. E. Malein, F. Bastiman, E. Clarke, and B. D. Gerardot, "Generating indistinguishable photons from a quantum dot in a noisy environment", Phys. Rev. B **95**, 201410 (2017).

[101] T. Flissikowski, A. Hundt, M. Lowisch, M. Rabe, and F. Henneberger, "Photon beats from a single semiconductor quantum dot", Phys. Rev. Lett. **86**, 3172–3175 (2001).

[102] M. Davanço, C. S. Hellberg, S. Ates, A. Badolato, and K. Srinivasan, "Multiple time scale blinking in InAs quantum dot single-photon sources", Phys. Rev. B **89**, 161303 (2014).

[103] M. Kaniber, A. Laucht, A. Neumann, J. M. Villas-Bôas, M. Bichler, M.-C. Amann, and J. J. Finley, "Investigation of the nonresonant dot-cavity coupling in two-dimensional photonic crystal nanocavities", Phys. Rev. B **77**, 161303 (2008).

[104] M. Winger, T. Volz, G. Tarel, S. Portolan, A. Badolato, K. J. Hennessy, E. L. Hu, A. Beveratos, J. Finley, V. Savona, and A. İmamoğlu, "Explanation of photon correlations in the far-off-resonance optical emission from a quantum-dot–cavity system", Phys. Rev. Lett. **103**, 207403 (2009).

[105] J. Suffczyński, A. Dousse, K. Gauthron, A. Lemaître, I. Sagnes, L. Lanco, J. Bloch, P. Voisin, and P. Senellart, "Origin of the optical emission within the cavity mode of coupled quantum dot-cavity systems", Phys. Rev. Lett. **103**, 027401 (2009).

[106] E. Peter, S. Laurent, J. Bloch, J. Hours, S. Varoutsis, I. Robert-Philip, A. Beveratos, A. Lemaître, A. Cavanna, G. Patriarche, P. Senellart, and D. Martrou, "Fast radiative quantum dots: from single to multiple photon emission", Applied Physics Letters **90**, 223118 (2007).

[107]L. Lanco and P. Senellart, “A highly efficient single photon-single quantum dot interface”, in *Engineering the Atom-Photon Interaction: Controlling Fundamental Processes with Photons, Atoms and Solids*, edited by A. Predojević and M. W. Mitchell (Springer International Publishing, New York, NY, 2015) Chap. 2, pp. 39–71.

[108]H. Ollivier, S. E. Thomas, S. C. Wein, I. M. de Buy Wenniger, N. Coste, J. C. Loredo, N. Somaschi, A. Harouri, A. Lemaitre, I. Sagnes, L. Lanco, C. Simon, C. Anton, O. Krebs, and P. Senellart, “Hong-Ou-Mandel interference with imperfect single photon sources”, Phys. Rev. Lett. **126**, 063602 (2021).

[109]A. Thoma, P. Schnauber, M. Gschrey, M. Seifried, J. Wolters, J.-H. Schulze, A. Strittmatter, S. Rodt, A. Carmele, A. Knorr, T. Heindel, and S. Reitzenstein, “Exploring dephasing of a solid-state quantum emitter via time- and temperature-dependent Hong-Ou-Mandel experiments”, Phys. Rev. Lett. **116**, 033601 (2016).

[110]A. Carmele and S. Reitzenstein, “Non-Markovian features in semiconductor quantum optics: quantifying the role of phonons in experiment and theory”, Nanophotonics **8**, 655–683 (2019).

[111]T. Miyazawa, K. Takemoto, Y. Nambu, S. Miki, T. Yamashita, H. Terai, M. Fujiwara, M. Sasaki, Y. Sakuma, M. Takatsu, T. Yamamoto, and Y. Arakawa, “Single-photon emission at 1.5 $\mu$m from an InAs/InP quantum dot with highly suppressed multi-photon emission probabilities”, Applied Physics Letters **109**, 132106 (2016).

[112]B. Brecht, A. Eckstein, A. Christ, H. Suche, and C. Silberhorn, “From quantum pulse gate to quantum pulse shaper—engineered frequency conversion in nonlinear optical waveguides”, New Journal of Physics **13**, 065029 (2011).

[113]S. Gao, O. Lazo-Arjona, B. Brecht, K. T. Kaczmarek, S. E. Thomas, J. Nunn, P. M. Ledingham, D. J. Saunders, and I. A. Walmsley, “Optimal coherent filtering for single noisy photons”, Phys. Rev. Lett. **123**, 213604 (2019).

[114]A. Christ, A. Eckstein, P. J. Mosley, and C. Silberhorn, “Pure single photon generation by type-I PDC with backward-wave amplification”, Opt. Express **17**, 3441–3446 (2009).

[115] A. Gatti, T. Corti, and E. Brambilla, "Temporal coherence and correlation of counterpropagating twin photons", Phys. Rev. A **92**, 053809 (2015).

[116] A. Gatti and E. Brambilla, "Heralding pure single photons: a comparison between counterpropagating and copropagating twin photons", Phys. Rev. A **97**, 013838 (2018).

[117] K.-H. Luo, V. Ansari, M. Massaro, M. Santandrea, C. Eigner, R. Ricken, H. Herrmann, and C. Silberhorn, "Counter-propagating photon pair generation in a nonlinear waveguide", Opt. Express **28**, 3215–3225 (2020).

[118] Y.-C. Liu, D.-J. Guo, K.-Q. Ren, R. Yang, M. Shang, W. Zhou, X. Li, C.-W. Sun, P. Xu, Z. Xie, Y.-X. Gong, and S.-N. Zhu, "Observation of frequency-uncorrelated photon pairs generated by counter-propagating spontaneous parametric down-conversion", Scientific Reports **11**, 12628 (2021).

[119] D.-J. Guo, R. Yang, Y.-C. Liu, J.-C. Duan, Z. Xie, Y.-X. Gong, and S.-N. Zhu, "Optical frequency down-conversion with bandwidth compression based on counter-propagating phase matching", Frontiers in Physics **9** (2021).

[120] M. Allgaier, V. Ansari, L. Sansoni, C. Eigner, V. Quiring, R. Ricken, G. Harder, B. Brecht, and C. Silberhorn, "Highly efficient frequency conversion with bandwidth compression of quantum light", Nature Communications **8**, 1–6 (2017).

[121] J. Lavoie, J. M. Donohue, L. G. Wright, A. Fedrizzi, and K. J. Resch, "Spectral compression of single photons", Nature Photonics **7**, 363–366 (2013).

[122] D. Nadlinger, P. Drmota, B. Nichol, G. Araneda, D. Main, R. Srinivas, D. Lucas, C. Ballance, K. Ivanov, E. Tan, et al., "Device-independent quantum key distribution", arXiv:2109.14600 (2021).

## Quantum key distribution with a frequency converted quantum dot

[13] N. Tomm, A. Javadi, N. O. Antoniadis, D. Najer, M. C. Löbl, A. R. Korsch, R. Schott, S. R. Valentin, A. D. Wieck, A. Ludwig, and R. J. Warburton, "A bright

and fast source of coherent single photons", Nature Nanotechnology **16**, 399–403 (2021).

[90]P. Chaiwongkhot, S. Hosseini, A. Ahmadi, B. L. Higgins, D. Dalacu, P. J. Poole, R. L. Williams, M. E. Reimer, and T. Jennewein, "Enhancing secure key rates of satellite QKD using a quantum dot single-photon source", arXiv:2009.11818 (2020).

[91]K. Takemoto, Y. Nambu, T. Miyazawa, Y. Sakuma, T. Yamamoto, S. Yorozu, and Y. Arakawa, "Quantum key distribution over 120 km using ultrahigh purity single-photon source and superconducting single-photon detectors", Scientific Reports **5**, 14383 (2015).

[93]B. Da Lio, C. Faurby, X. Zhou, M. L. Chan, R. Uppu, H. Thyrrestrup, S. Scholz, A. D. Wieck, A. Ludwig, P. Lodahl, and L. Midolo, "A pure and indistinguishable single-photon source at telecommunication wavelength", Advanced Quantum Technologies **5**, 2200006 (2022).

[94]X. You, M.-Y. Zheng, S. Chen, R.-Z. Liu, J. Qin, M.-C. Xu, Z.-X. Ge, T.-H. Chung, Y.-K. Qiao, Y.-F. Jiang, et al., "Quantum interference between independent solid-state single-photon sources separated by 300 km fiber", arXiv:2106.15545 (2021).

[123]P. W. Shor, "Polynomial-time algorithms for prime factorization and discrete logarithms on a quantum computer", SIAM Journal on Computing **26**, 1484–1509 (1997).

[124]H.-K. Lo, M. Curty, and B. Qi, "Measurement-device-independent quantum key distribution", Phys. Rev. Lett. **108**, 130503 (2012).

[125]U. Vazirani and T. Vidick, "Fully device independent quantum key distribution", Commun. ACM **62**, 133 (2019).

[126]C. H. Bennett and G. Brassard, "Quantum cryptography: public key distribution and coin tossing", Theoretical Computer Science **560**, 7–11 (2014).

[127]D. Gottesman, H.-K. Lo, N. Lutkenhaus, and J. Preskill, "Security of quantum key distribution with imperfect devices", Quant. Inf. Comput. **5**, 325–360 (2004).

[128]N. Lütkenhaus, "Security against individual attacks for realistic quantum key distribution", Phys. Rev. A **61**, 052304 (2000).

[129]A. Migdall, S. V. Polyakov, J. Fan, and J. C. Bienfang, *Single-photon generation and detection: physics and applications* (Academic Press, 2013).

[130]E. Waks, C. Santori, and Y. Yamamoto, "Security aspects of quantum key distribution with sub-Poisson light", Phys. Rev. A **66**, 042315 (2002).

[131]A. Boaron, G. Boso, D. Rusca, C. Vulliez, C. Autebert, M. Caloz, M. Perrenoud, G. Gras, F. Bussières, M.-J. Li, D. Nolan, A. Martin, and H. Zbinden, "Secure quantum key distribution over 421 km of optical fiber", Phys. Rev. Lett. **121**, 190502 (2018).

[132]T. Gao, L. Rickert, F. Urban, J. Große, N. Srocka, S. Rodt, A. Musiał, K. Żołnacz, P. Mergo, K. Dybka, W. Urbańczyk, G. Sęk, S. Burger, S. Reitzenstein, and T. Heindel, "A quantum key distribution testbed using a plug&play telecom-wavelength single-photon source", Applied Physics Reviews **9**, 011412 (2022).

[133]H. Z. J. Zeng, M. A. P. Ngyuen, X. Ai, A. Bennet, A. S. Solntsev, A. Laucht, A. Al-Juboori, M. Toth, R. P. Mildren, R. Malaney, and I. Aharonovich, "Integrated room temperature single-photon source for quantum key distribution", Opt. Lett. **47**, 1673–1676 (2022).

[134]E. Waks, K. Inoue, C. Santori, D. Fattal, J. Vuckovic, G. S. Solomon, and Y. Yamamoto, "Quantum cryptography with a photon turnstile", Nature **420**, 762–762 (2002).

[135]G. Murtaza, M. Colautti, M. Hilke, P. Lombardi, F. S. Cataliotti, A. Zavatta, D. Bacco, and C. Toninelli, "Efficient room-temperature molecular single-photon sources for quantum key distribution", arXiv:2202.12635 (2022).

[136]D. A. Vajner, L. Rickert, T. Gao, K. Kaymazlar, and T. Heindel, "Quantum communication using semiconductor quantum dots", arXiv:2108.13877 (2021).

[137]Ç. Samaner, S. Paçal, G. Mutlu, K. Uyanık, and S. Ateş, "Free-Space Quantum Key Distribution with Single Photons from Defects in Hexagonal Boron Nitride", arXiv e-prints (2022).

[138]T. Gao, M. v. Helversen, C. Anton-Solanas, C. Schneider, and T. Heindel, “Atomically-thin single-photon sources for quantum communication”, (2022).

[139]R. Y. Q. Cai and V. Scarani, “Finite-key analysis for practical implementations of quantum key distribution”, New Journal of Physics **11**, 045024 (2009).

[140]M. Bozzio, M. Vyvlecka, M. Cosacchi, C. Nawrath, T. Seidelmann, J. C. Loredo, S. L. Portalupi, V. M. Axt, P. Michler, and P. Walther, “Enhancing quantum cryptography with quantum dot single-photon sources”, arXiv:2204.11734 (2022).

[141]W.-Y. Hwang, “Quantum key distribution with high loss: toward global secure communication”, Phys. Rev. Lett. **91**, 057901 (2003).

[142]H.-K. Lo, X. Ma, and K. Chen, “Decoy state quantum key distribution”, Phys. Rev. Lett. **94**, 230504 (2005).

[143]S.-K. Liao, W.-Q. Cai, W.-Y. Liu, L. Zhang, Y. Li, J.-G. Ren, J. Yin, Q. Shen, Y. Cao, Z.-P. Li, et al., “Satellite-to-ground quantum key distribution”, Nature **549**, 43–47 (2017).

[144]X. Ma, B. Qi, Y. Zhao, and H.-K. Lo, “Practical decoy state for quantum key distribution”, Phys. Rev. A **72**, 012326 (2005).

[145]G. Foletto, F. Picciariello, C. Agnesi, P. Villoresi, and G. Vallone, “Security bounds for decoy-state quantum key distribution with arbitrary photon-number statistics”, Phys. Rev. A **105**, 012603 (2022).

[146]F.-Y. Lu, X. Lin, S. Wang, G.-J. Fan-Yuan, P. Ye, R. Wang, Z.-Q. Yin, D.-Y. He, W. Chen, G.-C. Guo, and Z.-F. Han, “Intensity modulator for secure, stable, and high-performance decoy-state quantum key distribution”, npj Quantum Information **7**, 75 (2021).

[147]Z. X. Koong, “Coherent light-matter interaction in semiconductor quantum dots”, PhD thesis (Heriot-Watt University, 2021).

## Conclusion

[148]C. J. Xin, J. Mishra, C. Chen, D. Zhu, A. Shams-Ansari, C. Langrock, N. Sinclair, F. N. C. Wong, M. M. Fejer, and M. Lončar, “Spectrally separable photon-pair

generation in dispersion engineered thin-film lithium niobate", Opt. Lett. **47**, 2830–2833 (2022).

[149]D. Zhu, C. Chen, M. Yu, L. Shao, Y. Hu, C. Xin, M. Yeh, S. Ghosh, L. He, C. Reimer, et al., "Spectral control of nonclassical light using an integrated thin-film lithium niobate modulator", arXiv:2112.09961 (2021).

[150]L. Zhai, G. N. Nguyen, C. Spinnler, J. Ritzmann, M. C. Löbl, A. D. Wieck, A. Ludwig, A. Javadi, and R. J. Warburton, "Quantum interference of identical photons from remote GaAs quantum dots", Nature Nanotechnology, 1–5 (2022).

[151]M. Lucamarini, Z. L. Yuan, J. F. Dynes, and A. J. Shields, "Overcoming the rate–distance limit of quantum key distribution without quantum repeaters", Nature **557**, 400–403 (2018).

[152]S. Wang, Z.-Q. Yin, D.-Y. He, W. Chen, R.-Q. Wang, P. Ye, Y. Zhou, G.-J. Fan-Yuan, F.-X. Wang, Y.-G. Zhu, et al., "Twin-field quantum key distribution over 830-km fibre", Nature Photonics **16**, 154–161 (2022).

[153]Y.-M. Xie, Y.-S. Lu, C.-X. Weng, X.-Y. Cao, Z.-Y. Jia, Y. Bao, Y. Wang, Y. Fu, H.-L. Yin, and Z.-B. Chen, "Breaking the rate-loss bound of quantum key distribution with asynchronous two-photon interference", PRX Quantum **3**, 020315 (2022).

[154]P. Zeng, H. Zhou, W. Wu, and X. Ma, "Quantum key distribution surpassing the repeaterless rate-transmittance bound without global phase locking", arXiv:2201.04300 (2022).

[155]S. Pirandola, R. Laurenza, C. Ottaviani, and L. Banchi, "Fundamental limits of repeaterless quantum communications", Nature Communications **8**, 1–15 (2017).